



UPPSALA
UNIVERSITET

*Digital Comprehensive Summaries of Uppsala Dissertations
from the Faculty of Science and Technology 1564*

Sputtering-based processes for thin film chalcogenide solar cells on steel substrates

PATRICE BRAS



ACTA
UNIVERSITATIS
UPSALIENSIS
UPPSALA
2017

ISSN 1651-6214
ISBN 978-91-513-0078-8
urn:nbn:se:uu:diva-329778

Dissertation presented at Uppsala University to be publicly examined in Polhemssalen, Ångström laboratory, Lägerhyddsvägen 1, Uppsala, Thursday, 9 November 2017 at 09:15 for the degree of Doctor of Philosophy. The examination will be conducted in English. Faculty examiner: PhD Veronica Bernudez (Solar Frontier K.K.).

Abstract

Bras, P. 2017. Sputtering-based processes for thin film chalcogenide solar cells on steel substrates. *Digital Comprehensive Summaries of Uppsala Dissertations from the Faculty of Science and Technology* 1564. 107 pp. Uppsala: Acta Universitatis Upsaliensis. ISBN 978-91-513-0078-8.

Thin film chalcogenide solar cells are promising photovoltaic technologies. Cu(In,Ga)Se₂ (CIGS)-based devices are already produced at industrial scale and record laboratory efficiency surpasses 22 %. Cu₂ZnSn(S,Se)₄ (CZTS) is an alternative material that is based on earth-abundant elements. CZTS device efficiency above 12 % has been obtained, indicating a high potential for improvement.

In this thesis, in-line vacuum, sputtering-based processes for the fabrication of complete thin film chalcogenide solar cells on stainless steel substrates are studied. CIGS absorbers are deposited in a one-step high-temperature process using compound targets. CZTS precursors are first deposited by room temperature sputtering and absorbers are then formed by high temperature crystallization in a controlled atmosphere. In both cases, strategies for absorber layer improvement are identified and implemented.

The impact of CZTS annealing temperature is studied and it is observed that the absorber grain size increases with annealing temperature up to 550 °C. While performance also improves from 420 to 510 °C, a drop in all solar cell parameters is observed for higher temperature. This loss is caused by blisters forming in the absorber during annealing. Blister formation is found to originate from gas entrapment during precursor sputtering. Increase in substrate temperature or sputtering pressure leads to drastic reduction of gas entrapment and hence alleviate blister formation resulting in improved solar cell parameters, including efficiency.

An investigation of bandgap grading in industrial CIGS devices is conducted through one-dimensional simulations and experimental verification. It is found that a single gradient in the conduction band edge extending throughout the absorber combined with a steeper back-grading leads to improved solar cell performance, mainly due to charge carrier collection enhancement.

The uniformity of both CIGS and CZTS 6-inch solar cells is assessed. For CZTS, the device uniformity is mainly limited by the in-line annealing process. Uneven heat and gas distribution resulting from natural convection phenomenon leads to significant lateral variation in material properties and device performance. CIGS solar cell uniformity is studied through laterally-resolved material and device characterization combined with SPICE network modeling. The absorber material is found to be laterally homogeneous. Moderate variations observed at the device level are discussed in the context of large area sample characterization.

Power conversion efficiency values above 15 % for 225 cm² CIGS cells and up to 5.1 % for 1 cm² CZTS solar cells are obtained.

Keywords: CIGS, CZTS, solar cell, photovoltaics, thin film, sputtering, annealing, gallium grading, blister, uniformity, stainless steel

Patrice Bras, Department of Engineering Sciences, Solid State Electronics, Box 534, Uppsala University, SE-75121 Uppsala, Sweden.

© Patrice Bras 2017

ISSN 1651-6214

ISBN 978-91-513-0078-8

urn:nbn:se:uu:diva-329778 (<http://urn.kb.se/resolve?urn=urn:nbn:se:uu:diva-329778>)

Dedicated to my family

List of papers

This thesis is based on the following papers, which are referred to in the text by their Roman numerals.

- I P. Bras, J. Sterner, C. Platzer-Björkman, "Influence of hydrogen sulfide annealing on copper–zinc–tin–sulfide solar cells sputtered from a quaternary compound target", *Thin Solid Films*, 582, 2015, pp. 233-238. DOI: <http://dx.doi.org/10.1016/j.tsf.2014.11.004>
- II P. Bras, J. Sterner, C. Platzer-Björkman, "Investigation of blister formation in sputtered $\text{Cu}_2\text{ZnSnS}_4$ absorbers for thin film solar cells", *Journal of Vacuum Science & Technology A*, 33, 2015, 061201. DOI: <http://dx.doi.org/10.1116/1.4926754>
- III P. Bras, C. Frisk, A. Tempez, E. Niemi, C. Platzer-Björkman, "Ga-grading and Solar Cell Capacitance Simulation of an industrial $\text{Cu}(\text{In,Ga})\text{Se}_2$ solar cell produced by an in-line vacuum, all-sputtering process", *Thin Solid Films*, 582, 2017, pp. 367-374. DOI: <http://dx.doi.org/10.1016/j.tsf.2017.06.031>
- IV P. Bras, L. Mauvy, J. Sterner, C. Platzer-Björkman, "Uniformity assessment of a 6-inch copper-zinc-tin-sulfide solar cell sputtered from a quaternary compound target", *Proceedings of the 42nd Photovoltaic Specialist Conference (PVSC)*, New Orleans, LA, USA, 2015, pp. 1-4. DOI: <http://dx.doi.org/10.1109/PVSC.2015.7356103>
- V P. Bras, A. Davydova, C. Platzer-Björkman, "SPICE network modeling of a 6-inch $\text{Cu}(\text{In,Ga})\text{Se}_2$ solar cell", in manuscript.

Reprints were made with permission from the publishers.

Personal contribution to the papers

- I Contribution to the definition of the research project, sample fabrication, sample characterization, data analysis and paper writing with input from co-authors.
- II Contribution to the definition of the research project, design of experiments, sample processing, major part of the characterization, data analysis and paper writing with input from co-authors.
- III Definition of the research project and scope of the investigation, sample fabrication, major part of the characterization, data analysis, SCAPS model build-up, simulations and paper writing with input from co-authors.
- IV Definition of the research project and scope of the investigation, part of the sample fabrication, part of the characterization, data analysis, simulations and paper writing with input from co-authors.
- V Definition of the research project and scope of the investigation, sample fabrication, major part of the characterization, data analysis, SPICE simulations and paper writing with input from co-authors.

Abbreviations and acronyms

CIGS	Cu(In,Ga)Se_2
CZTS	$\text{Cu}_2\text{ZnSn(S,Se)}_4$
PV	Photovoltaics
BIPV	Building-integrated photovoltaics
PIPV	Product-integrated photovoltaics
SCAPS	Solar cell capacitance simulator
SPICE	Simulation program with integrated circuit emphasis
SRH	Shockley-Read-Hall
CBD	Chemical bath deposition
TCO	Transparent conductive oxide
ITO	$\text{In}_2\text{O}_3\text{:SnO}_2$
CIS	CuInSe_2
CGS	CuGaSe_2
NREL	National renewable energy laboratory
PVD	Physical vapor deposition
GGI	Ga/(Ga+In)
DC	Direct current
RF	Radio-frequency
QR	Quick response
OBO	One-by-one
SEM	Scanning electron microscope
EDX or EDS	Energy-dispersive x-ray spectroscopy
XRF	X-ray fluorescence
XRD	X-ray diffraction
GIXRD	Grazing incidence x-ray diffraction
CTS	Cu_2SnS_3
PP-TOFMS TM	Plasma profiling time of flight mass spectrometry
IV	Current-voltage
JV	Current density-voltage
QE	Quantum efficiency
EQE	External quantum efficiency
IQE	Internal quantum efficiency
AC	Alternating current
MoNa	$\text{Mo:Na}_2\text{MoO}_4$
CV	Capacitance-voltage

Contents

Part I: Introduction	11
1 Renewables in a shifting global energy system	13
2 Solar energy and photovoltaics	14
3 Thin film photovoltaics	15
Motivation and aim	16
Part II: Theory	19
4 Thin film chalcogenide solar cells	21
4.1 Solar cell operating principle	21
4.1.1 Semiconductor properties	21
4.1.2 Requirements for a solar cell device	26
4.1.3 PN junction	28
4.1.4 Real solar cells	31
4.2 Thin-film heterojunction solar cells	33
4.3 Cu(In,Ga)Se ₂ solar cells	34
4.3.1 Material properties	34
4.3.2 Bandgap grading	36
4.4 Cu ₂ ZnSn(S,Se) ₄ solar cells	38
4.4.1 Material properties	38
4.4.2 Thermodynamic stability and consequences	39
5 Thin film deposition by sputtering	41
5.1 Principles and parameters	41
5.1.1 Principles of sputtering	41
5.1.2 Pulsed DC magnetron sputtering	43
5.2 Sputtering from a compound target	44
5.2.1 Compound target and implications during sputtering process	45
5.2.2 CIGS and CZTS sputtered from a compound target	45
5.3 Gas entrapment	47
Part III: Process and characterization	49
6 Process description	51

6.1	General process flow: From stainless steel substrates to finalized devices	51
6.2	CIGS: the DUO process	52
6.3	CZTS sputtering and annealing	55
7	Characterization methods and simulations	56
7.1	Material and device characterization	56
7.1.1	Scanning electron microscopy (SEM) and energy dispersive x-ray spectroscopy (EDX)	56
7.1.2	X-ray fluorescence (XRF)	57
7.1.3	X-ray diffraction (XRD)	58
7.1.4	Raman spectroscopy	59
7.1.5	Plasma profiling time of flight mass spectrometry (PP-TOFMS TM)	59
7.1.6	Current-voltage measurements	60
7.1.7	Quantum efficiency	60
7.2	Simulations	62
7.2.1	SCAPS	63
7.2.2	SPICE	63
	Part IV: Results and discussion	67
8	Improvement of thin film solar cell absorber layers and uniformity of 6-inch devices	69
8.1	Annealing CZTS absorbers (Paper I and II)	69
8.2	Bandgap grading for industrial CIGS solar cells (Paper III)	74
8.3	Uniformity of 6-inch chalcogenide solar cells (Paper IV and V)	77
8.3.1	Laterally-resolved characterization and simulation of CIGS absorbers and full solar cells	77
8.3.2	Sputtering and annealing process uniformity for 6-inch CZTS device fabrication	79
9	Concluding remarks	81
10	Future work	83
	Sammanfattning på svenska	85
	Résumé en français	88
	Acknowledgements	92
	References	94

Part I: Introduction

Global energy landscape and solar energy

1. Renewables in a shifting global energy system

The industrial revolution and all the related technological progress brought tremendous improvement in quality of life to humankind. One significant and adverse consequence, however, is the ever increasing energy consumption that characterizes modern world. Up to the end of the 20th century, mostly fossil resources such as coal, oil or gas have been used to satisfy the needs. Fossil fuels are finite by definition and their utilization ineluctably leads to greenhouse gas emissions which have terrible consequences on the environment and public health [1].

The need for a paradigm shift in our energy supply has been frequently pointed out (see for instance [2]) and evidence of a growing awareness from people, the private and the public sector, is observed everyday despite the magnitude of the challenge ahead. Politically, the Paris climate agreement of 2015 [3] sets the basis for a global transition towards a more environmentally-friendly energy model. On the industrial side, multiple large scale power plants (with capacities of several hundred MWp and up to the GWp level), based on renewable sources and exhibiting competitive energy prices, have recently been inaugurated and numerous other projects are soon to be realized [4]. Technologically speaking, scientists and engineers have found effective ways to harness energy from a variety of renewable sources available in Nature. The gravitational potential energy of water is exploited in various types of hydropower plants. The kinetic energy carried by winds is transformed into electricity by wind turbines. The electromagnetic energy radiated by the sun can be harnessed to produce heat, electricity or even synthetic fuels. Numerous exploitation strategies of other renewable energy sources are also being developed. Combining them all, a share of 18% of the total primary energy supply has been reached in 2014 [5]. Focusing on electricity, this proportion increases above 23% [5]. Although these numbers may appear low, the fact that the share of renewable power generation has grown at an average annual rate of 6% since 2009 combined with a recent drop in the cost of wind turbines and solar panels (30% and 80% respectively compared to 2009) is source of optimism for the coming decades [5]. Nevertheless, a lot remains to be done if we are to achieve the ambitious but necessary goals of the Paris agreement.

2. Solar energy and photovoltaics

The average incident solar irradiance on the surface of the earth is close to 160 W.m^{-2} [6]. The world total primary energy supply in 2014 was estimated to be around 160 000 TWh (13699 Mtoe) [7]. Considering the surface area of our planet, it is relatively easy to conclude that it receives from the sun, in just a couple of hours, the equivalent of the energy consumed by all human activity during a year. Of course, it is not practically possible to harness all this energy but it gives a representative idea of the potential of solar power. Solar energy can be converted into heat using solar thermal technologies or directly into electricity via the photovoltaic (PV) effect.

The photovoltaic effect was discovered by the French physicist Edmond Becquerel in 1839 [8]. After more than a century spent on improving the understanding of the underlying physics and developing experimental proofs, the first silicon solar cell appeared in Bell Labs in 1954 with a power conversion efficiency of 6% [9]. During the second half of the 20th century, intense research activities on PV cells have led to technology upscaling accompanied by constant improvement of solar cell performance. Mainly used in spatial applications at first, solar cells and solar panels gradually expanded towards other types of applications. Different solar programs funded by public subsidies in Europe, Japan and the USA during the 1990s and 2000s associated with industrial development have led to the generalization of PV adoption and the creation of numerous power plants based on solar panels all over the world. The achievement of levelized cost of electricity equivalent to or lower than conventional power plants in several recent PV projects constitutes an important milestone towards a much wider penetration of solar energy in today's energy landscape [10].

3. Thin film photovoltaics

The dominant PV technologies on the market nowadays are based on silicon. Building on decades of research in microelectronics which have led to the synthesis of extremely pure and high quality material at a relatively low cost, silicon is a natural candidate for efficient solar cell manufacturing. Power conversion efficiency for record Si solar cells is above 26 % [11] while it ranges from 15 to more than 20 % for commercial modules, depending on the technology. However, silicon is not the perfect candidate for all PV applications. First of all, standard crystalline Si cells need to be rather thick (several tens of microns at least) in order to absorb a significant part of sunlight and the corresponding cells are fragile leading to bulky and heavy, glass-encapsulated solar panels. Thin-film technologies are based on different types of semiconductor material used as light absorbers. They typically exhibit a higher absorption coefficient than crystalline silicon which means that a few micron-thick layer is sufficient to absorb sunlight effectively. Historically, amorphous silicon has played an important role in the field of thin film solar cells although it is heavily declining nowadays due to relatively low efficiency and light-induced degradation. Copper indium gallium selenide (Cu(In,Ga)Se_2 , CIGS) and cadmium telluride (CdTe)-based solar cells are the most promising thin film technologies that have already reached the commercial stage. At the research and development scale, solar submodules above 18% for these two technologies have been reported [12] while commercially available modules exhibit total area efficiencies in the range 14-16% depending on the manufacturer and the technology [13, 14].

Concerns about the toxicity of Cd as well as the potential scarcity of Te and In have triggered intense research effort to find more earth-abundant and non-toxic thin film absorber materials for solar cells. $\text{Cu}_2\text{ZnSn(S,Se)}_4$ (CZTS) has been identified as a potential alternative that matches well the previously mentioned criteria. Record solar cell efficiency for this material is 12.6% at the research scale denoting a high improvement potential [15].

Motivation and aim

Our current electricity supply is mainly based on centralized generation in large power plants and wide-scale distribution through the power grid. As previously mentioned, photovoltaics is compatible with this approach and large scale PV plants allow to reach the lowest electricity price due to scale effects. However, one important characteristic of sunlight is its distributed nature meaning that it is available almost anywhere on Earth as long as sun is shining. As a consequence, electricity generation can also take place much closer to where it is consumed, limiting transportation-related losses, additional costs, guaranteeing partial or complete energy autonomy to buildings and devices, and increasing resilience in case of power grid failure. In this context, the concept of building integrated photovoltaics (BIPV) is now considered as an important component of the photovoltaic energy production of the future.

BIPV is the combination of a photovoltaic cell or module and a construction material to obtain a product that exhibits electricity generation capability together with some building-related function. One of the most common examples are photovoltaic panels integrated in rooftops or facades. In this case, the electricity generation function is coupled to the protection and waterproofness expected from the building component.

Product integrated photovoltaics or PIPV is the extension of this concept to any kind of products with an emphasis on new digital technologies ranging from portable consumer electronics (tablets, portable chargers) to network of autonomous sensors (internet of things).

Thin film PV technologies are particularly adapted to applications in the fields of BIPV and PIPV. CIGS, for instance, can be deposited on flexible and light-weight substrates using mature thin-film deposition techniques such as sputtering or evaporation. The integration of such cell into, for instance, building material, is facilitated compared to crystalline silicon due to enhanced modularity in terms of shape, size, mechanical properties and device parameters.

Midsummer AB has developed a process exclusively based on sputtering for the fabrication of CIGS solar cells on thin stainless steel substrates. Optimization of the process for CIGS solar cell fabrication to reach higher performance level is critical in an industrial context to guarantee further penetration of the technology into the market. On the other hand, exploring related promising alternative technologies based on more earth-abundant materials appears to be also necessary for wider spread of thin film PV technologies in a longer term future.

This thesis, conducted in collaboration between Midsummer AB and Uppsala University, focuses on the optimization of absorber layer synthesis for application in thin film solar cells. The main efficiency bottlenecks related to CIGS and CZTS absorber formation within the framework of an industrial process are identified and studied.

For CIGS solar cells, the one step sputtering of the absorber layer leads to lower minority carrier lifetime compared to samples typically obtained in research context. Additionally, the accessible thickness range is limited to about one micrometer to guarantee low cycle time and high throughput in production. The implications of these constraints on optimal bandgap grading are investigated both experimentally, through the use of CIGS compound targets with different In/Ga content, and by device simulations using SCAPS.

Due to thermodynamic instability of CZTS above 500 °C in vacuum, one step deposition of absorbers at high temperature is particularly challenging. A process for CZTS solar cells on steel substrates based on room temperature sputtering followed by annealing in a controlled atmosphere and compatible with Midsummer's technology is also proposed and studied. Fine tuning of temperature and sulfur partial pressure during the annealing sequence are preponderant parameters for obtaining CZTS absorbers with appropriate optoelectronic properties. A particular attention is given to the effect of temperature during 15 minute-long, in-line vacuum annealing process. While performance increases for intermediate temperatures, a drop in all solar cell parameters is observed for higher temperature. The reason for this performance loss is studied in detail and routes for avoiding the problem are suggested.

Uniformity of all layers in thin film solar cells is one of the most important characteristics sought after when working on large area industrial devices. The geometry of solar cells produced at Midsummer resembles silicon cells but potentially exhibit non-homogeneity inherent to large area thin film deposition. For CIGS, experimental assessment of lateral non-uniformity is compared to a 2D network model based on SPICE, developed to relate local device properties to the performance of the full size solar cell. 6-inch CZTS device uniformity is found to be mainly dictated by the annealing process, performed vertically due to equipment design. The effect of the annealing chamber configuration on lateral non-uniformity of CZTS is studied.

Part II: Theory

Thin film solar cells based on Cu(In,Ga)Se_2 and $\text{Cu}_2\text{ZnSn(S,Se)}_4$

4. Thin film chalcogenide solar cells

CuInSe₂ (CIS) and later Cu(In,Ga)Se₂ (CIGS) solar cells have been investigated for more than 40 years [16]. Both incremental and more disruptive research at the material, process and device structure levels have allowed efficiency improvements over the years to reach a laboratory scale record value of 22.6% in 2016 [17]. CZTS development is more recent [18] and greatly benefited from research findings related to CIGS technology. However, intrinsic thermodynamic instability of CZTS at high temperature and more complex defect chemistry compared to CIGS are two important differences that contribute to the performance gap between these two technologies. The purpose of this chapter is, first, to describe the general operating principle of a solar cell and to briefly introduce its main parameters. The material properties of both CIGS and CZTS are then explored. In each case, a specific topic related to solar cell absorber optoelectronic properties optimization is examined, namely bandgap grading for CIGS and high temperature annealing for CZTS.

4.1 Solar cell operating principle

This section starts with a short review of important semiconductor properties. Then, the requirements for designing an efficient solar cell are discussed. Subsequently, a summary of the physics of the main component of solid state solar cells, the PN junction, is given. Finally, the solar cell performance parameters are described.

4.1.1 Semiconductor properties

Charge carrier concentration in a semiconductor

Semiconductors and insulators are materials exhibiting a special energy band structure where a valence and a conduction band are separated by a so-called energy gap, E_g , where no allowed energy states are present. They differ by the magnitude of the bandgap where the distinction is mainly a matter of convention. E_g values for semiconductors are generally below 5 eV. Larger bandgap materials are most of the time considered as insulators.

Due to thermal or external excitation such as light shining on the material, some electrons from the valence band can be transferred to the conduction band leaving behind a positive quasi-particle called hole. The carrier concentration

in the valence and the conduction band of a semiconductor can be obtained by first multiplying the density of available states in each of the bands by the corresponding occupation function given by the Fermi-Dirac distribution and by integrating the result over all accessible energy levels. The so-called Fermi level of the semiconductor is then defined as the energy level that has a 50% probability of being occupied. Using the Boltzmann approximation, the density of electrons in the conduction band n and holes in the valence band p can be calculated with equations (4.1) and (4.2).

$$n = N_C \exp\left(\frac{E_F - E_C}{k_B T}\right) \quad (4.1)$$

$$p = N_V \exp\left(\frac{E_V - E_F}{k_B T}\right) \quad (4.2)$$

N_V and N_C are the effective density of states in the valence and conduction band which depend on the effective mass of holes and electrons respectively. Further discussion on these parameters is available in, for instance, [19]. E_V is the energy level corresponding to the top of the valence band and E_C corresponds to the bottom of the conduction band. E_F represents the Fermi level, k_B is Boltzmann constant and T is the temperature.

In thermal equilibrium condition, and for a non-doped or intrinsic semiconductor, some free electrons and holes are thermally generated. Their concentration corresponds to the intrinsic concentration n_i which depends on temperature. Generalizing to all semiconductors (undoped and doped) at thermal equilibrium, the square of the intrinsic carrier concentration is equal to the concentration of electrons in the conduction band multiplied by the concentration of holes in the valence band as shown in eq. (4.3).

$$np = n_i^2 = N_C N_V \exp\left(\frac{E_V - E_C}{k_B T}\right) = N_C N_V \exp\left(-\frac{E_g}{k_B T}\right) \quad (4.3)$$

Doping in a semiconductor

One important characteristic of a semiconductor is that its free charge carrier density can be modified by doping. Doping can be intentional, as for instance in silicon solar cells. In this case, so-called donor or acceptor atoms are deliberately introduced into the Si lattice. Donor atoms such as phosphorus exhibit an additional valence electron compared to silicon. This electron will not take part in the formation of a covalent bond and it will act as a free electron when the dopant atom is ionized. In terms of energy band diagram, the inclusion of such impurities in the lattice creates additional energy levels, called donor levels, in the bandgap of Si which can emit an electron to the conduction band upon ionization. This process is called n-type doping.

Silicon can also be doped with acceptors, for instance boron atoms which have only three valence electrons. This leads to the formation of a free hole.

Acceptor levels are created in the bandgap and the material is said to be doped p-type.

Acceptor and/or donor levels can also form spontaneously, without intentional doping, as a result of defects in the crystal structure of a material. This phenomenon is exploited in CIGS and CZTS where acceptor levels naturally form, resulting in p-type doping.

In a doped semiconductor in equilibrium, one type of free charge carrier will dominate. In a p-type material, holes are orders of magnitude more abundant than electrons. In this case, holes are called majority carriers and electrons are minority carriers. The situation is reversed in an n-type semiconductor. Assuming complete ionization of donors (acceptors), which is generally valid at room temperature, the free charge carrier density in a doped semiconductor can be approximated by the donor (acceptor) density N_D (N_A). The resulting electron and hole concentrations in n and p-type semiconductors, calculated with eq. (4.3), are given in Table 4.1.

	n	p
n-type	N_D	$\frac{n_i^2}{N_D}$
p-type	$\frac{n_i^2}{N_A}$	N_A

Table 4.1. Carrier concentrations in doped semiconductors.

From eqs. (4.1) and (4.2) it follows that the Fermi level of a p-type semiconductor is closer to the valence band edge compared to the same intrinsic material. For an n-type material, the Fermi level is brought closer to the conduction band minimum. The position of the Fermi level is given by eqs. (4.4) and (4.5).

$$E_C - E_F = kT \ln \left(\frac{N_C}{N_D} \right) \quad (4.4)$$

$$E_F - E_V = kT \ln \left(\frac{N_V}{N_A} \right) \quad (4.5)$$

Conduction in a semiconductor

Delocalized or free carriers are responsible for electrical conduction in semiconductors. Due to their charge, they can be drifted by electrostatic forces resulting from an electric field. They will also tend to diffuse to guarantee an even concentration throughout the material. The resulting current density, defined as current per unit area, that can flow in a semiconductor is then com-

posed of a drift and a diffusion component. For each of them, the contribution of holes and electrons must be considered.

$$\mathbf{J}_{\text{drift}} = q\varepsilon(\mu_n n + \mu_p p) \quad (4.6)$$

$$\mathbf{J}_{\text{diff}} = q \left(D_n \frac{dn}{dx} - D_p \frac{dp}{dx} \right) \quad (4.7)$$

$$\mathbf{J}_{\text{tot}} = \mathbf{J}_{\text{drift}} + \mathbf{J}_{\text{diff}} \quad (4.8)$$

The drift current $\mathbf{J}_{\text{drift}}$ is proportional to the elementary charge q , the charge carrier concentrations n and p , the respective mobilities μ_n and μ_p and the electric field ε . Simply speaking, the mobility is a measure of the impact of an electric field on the movement of carriers.

The diffusion current \mathbf{J}_{diff} depends on the elementary charge q , the gradient of charge carrier concentrations $\frac{dn}{dx}$, $\frac{dp}{dx}$, in one dimension, and the diffusion coefficients for electrons and holes D_n and D_p . The minus sign in eq. (4.7) arises from the different polarity of charge carriers.

Equation (4.9), called Nernst-Einstein equation, relates mobility μ and diffusion coefficient D .

$$D = \frac{\mu k_B T}{q} \quad (4.9)$$

Generation, recombination and ambipolar transport equation

In a semiconductor, free charge carriers are generated thermally or as a result of external excitation. Conversely, an electron and a hole can annihilate each other in a process called recombination. In the following, the behavior of minority carriers in a p-type semiconductor (electrons) is studied to illustrate recombination. This example is representative of what happens in CIGS and CZTS solar cells where the absorber is p-type.

When additional energy is supplied to a p-type semiconductor, for instance when light is shone on it, the concentration of both types of free charge carriers is increased by the same amount until a new equilibrium is reached. Low level injection is assumed which means that the increase in charge carrier concentration is smaller than the majority carrier (holes) concentration at thermal equilibrium.

When the external energy source shuts down, the minority charge carrier concentration will decay exponentially until it reaches its initial equilibrium value. The characteristic decay time in this process is called minority carrier lifetime τ and it is representative of the recombination processes occurring in the material. The recombination rate R is equal to the excess carrier concentration divided by the corresponding lifetime as shown in eq. (4.10). A convenient and related parameter to characterize material quality in solar cells is the minority carrier diffusion length L . The relationship between L and τ is shown in eq. (4.11).

$$R_n = \frac{\Delta n}{\tau_n} \quad (4.10)$$

$$L_n = \sqrt{D_n \tau_n} \quad (4.11)$$

R_n is the recombination rate for electrons. Δn is the excess electron concentration. τ_n is the electron lifetime. L_n is the electron diffusion length and D_n is the diffusion coefficient for electrons. These relationships are also valid for n-type semiconductors except that holes are considered instead of electrons.

Minority carrier lifetime is a very important material property in solar cells because it determines the amount of time available for minority carrier collection before recombination occurs. As a result, large values of τ are desirable in order to minimize losses due to recombination.

Recombination in semiconductor materials follows three different mechanisms. The most fundamental process is band-to-band radiative recombination. Radiative recombination cannot be avoided and originates from the fundamental energy transfer balance that must exist between a material and its surroundings. This process is characterized by the emission of a photon with an energy close to the semiconductor bandgap upon recombination.

Auger recombination is a three particle mechanism where the energy released by an electron-hole recombination is transferred to a third particle which then loses the surplus of energy via thermalization.

The third process, called Shockley-Read-Hall (SRH) recombination, originates from trap states in the semiconductor bandgap due to defects in its lattice. Formalized by Shockley, Read and Hall, SRH recombination is a complex multistep process that is of particular interest in thin film solar cells where it is one of the dominant recombination processes. In this case, the recombination rate is given by eq. (4.12).

$$R_{SRH} = \nu_{th}^2 \sigma_p \sigma_n N_T \frac{np - n_i^2}{\nu_{th} \sigma_n n + \nu_{th} \sigma_p p + e_n + e_p} \quad (4.12)$$

ν_{th} is the thermal velocity, σ_n and σ_p are the trap capture cross-sections for electrons and holes respectively and N_T is the trap density. e_n and e_p characterize electron and hole emission from the trap. Simply speaking, ν_{th} and σ represent the reach of the trap.

The three recombination mechanisms are depicted schematically in Figure (4.1). Finally, surface defects caused by, for instance, dangling bonds, play an important role in solar cells, especially in modern silicon photovoltaics.

If we consider a particular volume element in a slab of semiconductor material, generation and recombination take place simultaneously. Charge carriers can also flow in and out. To express the variation of carrier concentration

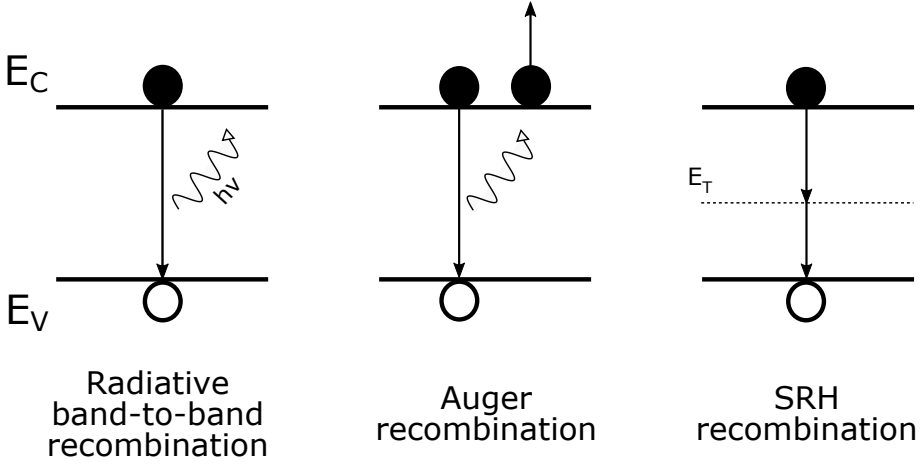


Figure 4.1. Three types of recombination. E_T is the energy level of a trap state. $h\nu$ is the energy of a photon emitted during radiative recombination process.

with time in this volume element, the continuity equation (4.13), or ambipolar transport equation, obtained by combining eqs. (4.6) and (4.7) with generation/recombination processes is used [20]. The 1D form of the equation for electrons is shown in eq. (4.13) for simplicity. A similar expression exists for holes.

$$\frac{\partial n}{\partial t} = D_n \frac{\partial^2 n}{\partial x^2} + \mu_n \frac{\partial(\varepsilon_x n)}{\partial x} + G_n - R_n \quad (4.13)$$

n is the electron concentration which depends on position x and time t , D_n is the electron diffusion coefficient, μ_n is the electron mobility and ε_x is the electric field in the direction x . R_n is the net thermal electron generation-recombination rate. G_n is the generation rate of electrons due to other processes, for instance photo-generation.

4.1.2 Requirements for a solar cell device

In order to generate electrical power from the electromagnetic energy flux radiated by the sun, an efficient solar cell combines several features. First of all, sunlight is absorbed in the device. Light absorption leads to the generation of charge carriers. The corresponding electrons and holes are then separated before they recombine. The last step is charge carrier collection by electrical contacts.

Most of today's solar cells are based on a semiconductor light absorber. Semiconductors can have a direct or an indirect bandgap. In the former case, the minimum of the conduction band coincides with the maximum of the valence band in momentum-energy space. Such semiconductors are potentially

interesting light absorbers since the energy supplied by incoming light is enough to excite an electron to the conduction band. For an indirect semiconductor, such process also requires simultaneous momentum transfer. An indirect semiconductor can also be used in solar cells, silicon being the most obvious example, but its absorption coefficient is typically lower leading to an increased thickness of the absorber layer.

In an ideal semiconductor absorber, if the energy of an incoming photon is larger than its bandgap, an electron-hole pair is created, provided the photon is absorbed. Higher energy photons will also be absorbed and will excite charge carriers to a deeper level in the valence and conduction band. However, these carriers will rapidly relax to the band edges in a process called thermalization before being collected. Photons with energies smaller than the bandgap will simply not contribute to free charge carriers generation. As a result, in so-called single junction solar cells, a trade-off exists between maximizing absorption and minimizing thermalization losses. As shown in Figure 4.2, the largest part of the energy radiated by the sun is in the spectral range between 300 and 1200 nm. As a result, semiconductor materials with bandgaps ranging from 1 to 1.5 eV are suitable for single junction solar cell applications [19]. For an ideal single junction solar cell exhibiting radiative recombination only, a maximum power conversion efficiency a little above 30% for an absorber bandgap of 1.1 eV has been predicted by Shockley and Queisser [21].

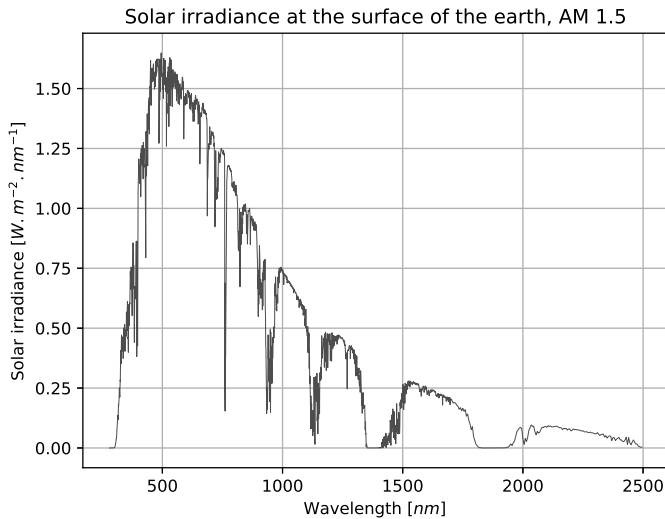


Figure 4.2. Reference solar irradiance spectrum for air mass 1.5. Data taken from [22].

Charge carrier separation and selective extraction in solid state solar cells is performed by a PN junction and metallic contacts, respectively.

4.1.3 PN junction

PN junction in thermal equilibrium

In a PN junction, also called PN diode, a p-type semiconductor is brought in contact with an n-type semiconductor. In the following, the PN junction under study is a so-called homojunction where the p-type and the n-type semiconductors are from the same material but doped differently. The most important consequence is that the bandgap is the same on both sides of the junction. Heterojunctions or junctions between two different semiconductor materials follow the same principle although the formula derivation is somewhat more difficult because of the presence of two different bandgaps.

At the metallurgical junction, excess electrons from the n-side diffuse to the p-side leaving positive fixed charges behind. The reciprocal process also takes place for holes moving from the p-side to the n-side. Positive fixed charge in the n-type material and negative fixed charge in the p-type material result in an electric field that tends to drift electrons to the n-region and holes in the opposite direction, counteracting diffusion. When equilibrium is reached, a so called space charge region depleted of free charge carriers forms at the junction. The space charge region is hence also called depletion region. In equilibrium, the Fermi level is constant throughout the PN junction leading to band bending at the junction. The electrostatic potential difference between the p and the n-side is represented as qV_{bi} in the energy band diagram of Figure 4.3. From the charge density in the space charge region, and integrating the Poisson equation assuming an abrupt PN junction, one can calculate the electric field distribution in the depletion region. By a second integration, the electrostatic potential is obtained and the built-in potential can be evaluated as shown in eq. (4.14). The energy band diagram for the junction can then be drawn. A graphical representation of this procedure as well as the corresponding energy band diagram are shown in Figure 4.3.

$$V_{bi} = \frac{q}{2\epsilon_r\epsilon_0}(N_Dx_n^2 + N_Ax_p^2) \quad (4.14)$$

ϵ_0 is the vacuum permittivity and ϵ_r is the considered material relative permittivity. x_n and x_p represent the extent of the space charge region in the n and p-side of the junction respectively. They are defined in Figure 4.3.

Using eqs. (4.3), (4.4) and (4.5), and based on the band diagram of Figure 4.3, a second expression of the junction built-in potential is obtained (eq. 4.15).

$$qV_{bi} = E_G - E_{Fn} - E_{Fp} = k_B T \ln \left(\frac{N_A N_D}{n_i^2} \right) \quad (4.15)$$

E_{Fn} corresponds to the energy difference between the conduction band minimum and the Fermi level on the n-type side of the PN junction. E_{Fp} is the energy difference between the Fermi level and the top of the valence band in the p-type side of the junction.

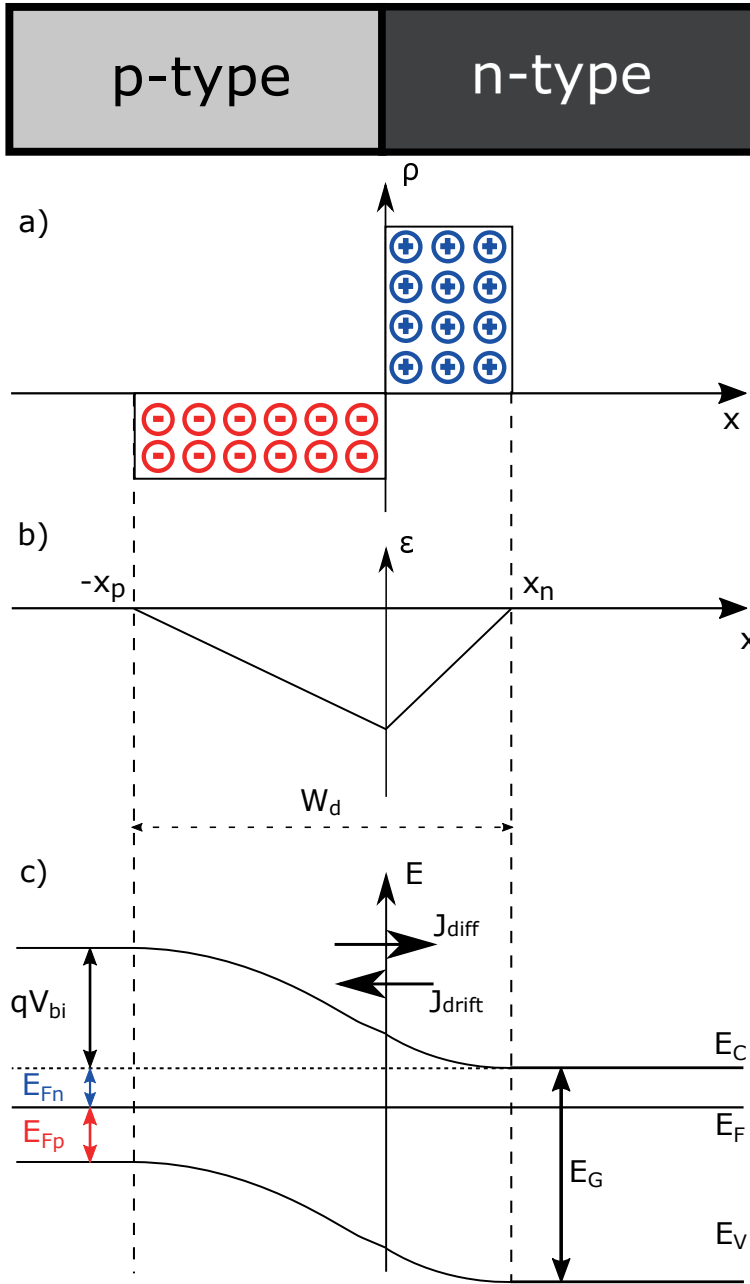


Figure 4.3. A schematic representation of electrical parameters in an abrupt PN junction including the charge density ρ (a), the internal electric field ϵ (b) and the corresponding band diagram (c). W_d is the width of the space charge region, J_{diff} and J_{drift} represent the diffusion and drift current density, respectively.

Combining eq. (4.14) and (4.15), the width of the space charge region W_D can be calculated. The expression is given in eq. (4.16).

$$W_D = x_n + x_p = \sqrt{\frac{2\epsilon_0\epsilon_r V_{bi}}{q} \left(\frac{1}{N_A} + \frac{1}{N_D} \right)} \quad (4.16)$$

It is obvious from 4.16 that the doping level of the semiconductors will have a strong impact on the width of the depletion region.

Voltage biasing and illumination of an ideal PN junction

Forward biasing a PN diode is achieved by applying a positive potential difference between the p-type and the n-type side of the junction. The applied voltage has an opposite polarity compared to the junction built-in voltage. The electrostatic potential barrier between the two sides of the junction is then lowered meaning that some electrons start diffusing from the n-side to the p-side where they recombine with majority holes. Holes undergo the opposite process. This diffusion process is enhanced with increasing voltage bias. The majority carrier concentration reduces as a result of recombination with diffusing carriers. This is compensated by electron injection from the voltage source and a net current flows from the p-side to the n-side and in the external circuit.

In reverse bias conditions, the potential barrier at the junction is increased. The electric field in the space charge area is enhanced and some minority carriers are drifted across the junction. A very small current flows from the n-side to the p-side. Contrary to the diffusion current in forward bias, this small drift current involves minority carriers resulting in a low intensity, so-called, dark saturation current density, J'_0 .

For an ideal diode, deriving a relationship between current density J and applied voltage V involves several steps. At each step, the contribution from holes in the n-side and electrons in the p-side must be considered. By applying the ambipolar transport equation (4.13) in the quasi neutral regions of the PN junction, the minority carrier distribution is obtained. Using Fick's diffusion law, the corresponding current at the edge of the space charge region is calculated. Finally, assuming that the diffusion current is constant throughout the space charge region, the famous current-voltage relationship of an ideal PN junction, or Shockley equation, is derived.

$$J = J'_0 \left(\exp \left(\frac{qV}{k_B T} \right) - 1 \right) \quad (4.17)$$

$$J'_0 = qn_i^2 \left(\frac{D_n}{L_n N_A} + \frac{D_p}{L_p N_D} \right) \quad (4.18)$$

The dark saturation current density is greatly influenced by recombination in the device. An expression for J'_0 is presented in eq. (4.18). A value as low

as possible for this parameter is desirable as it would imply that recombination losses are limited.

Under illumination, free charge carriers are generated. The derivation of the current-voltage equation is similar to the previous procedure. One important difference is that the contribution from light-induced generation must be considered in eq. (4.13). The resulting equation (4.19) exhibits an additional term J_{ph} corresponding to the photogenerated current density.

$$J = J_0' \left(\exp \left(\frac{qV}{k_B T} \right) - 1 \right) - J_{ph} \quad (4.19)$$

The negative sign in the equation arises from the fact that, under forward bias, current is extracted from the device. The diode or solar cell under illumination can then be used as a power source.

4.1.4 Real solar cells

Current density/voltage relationship of a real solar cell

The derivation of the Shockley equation assumes an ideal solar cell. In practice, and especially in thin film solar cells where the absorber material is polycrystalline and far from ideal, additional contributions to the current density-voltage relationship must be considered. Taking into account generation and recombination through trap states in the space charge region, a so called ideality factor A is introduced in eq. (4.19) and the saturation current density J_0 is modified to include trap-related leakage current in reverse bias.

Additionally, real solar cell devices have an intrinsic series resistance R_S that limits the current flow at high voltages. It originates from the device structure itself as well as resistive losses in the contacts. If the series resistance is non-negligible, it has a strong negative impact on the fill factor of the device and hence reduces solar cell performance.

Finally, due to, for instance, imperfections of the different layers in a solar cell, an alternative current path through the device can form locally resulting in electrical losses. These losses are taken into account through the inclusion of a so-called shunt resistance R_{SH} term. For optimal performance, the shunt resistance of solar cells needs to be as large as possible. The resulting JV relationship shown in eq. (4.20) accurately describes the behavior of the solar cells studied in the present work.

$$J = J_0 \left[\exp \left(\frac{q(V - R_S J)}{A k_B T} \right) - 1 \right] + \frac{V - R_S J}{R_{SH}} - J_{ph} \quad (4.20)$$

Solar cell parameters

A typical current density-voltage or JV curve for a solar cell is represented in Figure 4.4. Some of the most important corresponding parameters are also shown.

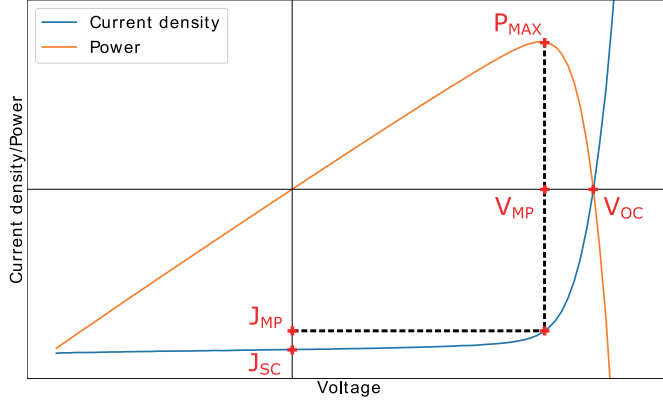


Figure 4.4. An example of current density-voltage or JV curve of a solar cell including important parameters. The power-voltage curve is also shown.

The open circuit voltage or V_{OC} is defined as the voltage where no current flows through the device. The short circuit current density, J_{SC} represents the current flowing through the circuit when the bias voltage is zero, in other words when the solar cell is short-circuited. The maximum power point, denoted by $_{MP}$ indices, corresponds to the situation where maximum power P_{MAX} is extracted from the solar cells. The corresponding voltage and current density are V_{MP} and J_{MP} respectively. From these parameters, the fill factor FF can be defined. Finally, the power conversion efficiency η is calculated as the ratio between incoming irradiance P_{IN} and the extracted electrical power following eq. (4.23).

$$FF = \frac{V_{MP}J_{MP}}{V_{OC}J_{SC}} \quad (4.21)$$

$$P_{MAX} = V_{OC}J_{SC}FF \quad (4.22)$$

$$\eta = \frac{P_{MAX}}{P_{IN}} \quad (4.23)$$

4.2 Thin-film heterojunction solar cells

At the core of a heterojunction solar cell lies a PN junction involving two different semiconductors. The general operating principle is similar to what was presented for homojunctions. There are, however, a few important differences which impact the solar cell performance. The dark saturation current density $J'_{0,H}$ of an ideal heterojunction is given by eq. (4.24).

$$J'_{0,H} = q \left(\frac{D_n n_{i,p}^2}{L_n N_A} + \frac{D_p n_{i,n}^2}{L_p N_D} \right) \quad (4.24)$$

The difference compared to the saturation current density of a homojunction shown in eq. (4.18) lies in the consideration of the intrinsic carrier concentration of both the n-type ($n_{i,n}$) and p-type ($n_{i,p}$) materials. As shown in eq. (4.3), the intrinsic carrier concentration decays exponentially with increasing bandgap energy meaning that the saturation current density can theoretically be reduced if one of the materials in the heterojunction exhibits a larger bandgap. The reverse saturation has a direct impact on the open circuit voltage of the solar cell as can be seen in eq. (4.25). This equation is obtained by rewriting eq. (4.19) at open-circuit conditions.

$$V_{OC} \approx \frac{k_B T}{q} \ln \frac{J_{ph}}{J'_0} \quad (4.25)$$

The reduction of the saturation current allowed by heterojunctions hence offers the perspective to reach higher open-circuit voltage compared to homojunctions.

Using a larger bandgap heterojunction partner also allows to decouple electrical and optical properties of the materials involved in the junction by using an optically transparent semiconductor together with an optoelectrically optimized absorber.

In practice, several other effects linked to heterojunction formation have to be considered. Interface defects can be created as a result of, for instance, lattice mismatch or deposition process chosen to form the junction, leading to enhanced recombination. Additionally, band alignment between the two semiconductors must be engineered carefully to avoid interface recombination [23, 24].

Thin film heterojunctions solar cells are usually produced using mature deposition techniques such as sputtering or coevaporation. They can be fabricated on a variety of substrates including glass, polymers and metal foils.

The commonly used substrate structure involves a metallic back-contact, an absorber layer based on a direct bandgap semiconductor, an optically transparent buffer/window layer to complete the PN junction and a front electrode based on transparent conducting oxide (TCO) materials.

The band diagram of thin film solar cells is more complex than for homo-junction cells as it involves several materials. The back contact material used in chalcogenide solar cells is molybdenum as it is reported to form an ohmic contact with CIGS. Mo is also used in CZTS devices despite not being an ideal candidate as further explained in section 4.4.2. The absorber material is then deposited. Properties of CIGS and CZTS are further discussed in the following sections.

As previously discussed, the interface between the p and n-type layer is critical for solar cell performance as recombination easily occurs at the metal-lurgical junction and high quality junction formation is a crucial step for well behaved devices [23, 25]. A cadmium sulfide thin film obtained by chemical bath deposition (CBD) is used in most cases as a heterojunction partner due to high quality of the resulting junction [26, 27]. However, concerns about the toxicity of Cd have driven research efforts towards identifying an efficient alternative n-type layer. Several candidates including Zn(O,S), ZnMgO, Zn-SnO or In_2S_3 show encouraging results [28, 29]. The process studied here is focused on sputtered In_2S_3 buffer layer. Sputtering is generally avoided for buffer deposition as it can lead to interface damage (see, for instance, [30]), however, process parameter tuning allows to obtain high quality cells [31, 32]. Sputtering has the additional advantage of being more easily incorporated in physical vapor deposition (PVD)-based solar cell production line which is especially relevant in the process under study.

The n-type buffer layer is generally covered with a highly resistive ZnO-based window layer. Although this layer is not needed in theory, its presence has been shown to dramatically reduce the negative impact of local defects in the devices such as pinholes and local shunts [33]. The device is finalized by the deposition of a TCO layer such as ZnO:Al or ITO. A simplified and generic schematic of a thin film solar cell band diagram is shown in Figure 4.5.

4.3 $\text{Cu}(\text{In,Ga})\text{Se}_2$ solar cells

After going through the main material properties of CIGS, this section focuses on a specific aspect that has contributed to high efficiency levels reached by CIGS solar cells: bandgap grading.

4.3.1 Material properties

CuInSe_2 (CIS) and CuGaSe_2 (CGS) are ternary $I-III-VI_2$ semiconductors that crystallize in the chalcopyrite structure. More than 40 years ago, CIS was used to produce the first chalcopyrite based solar cells [16]. Apart from bandgap related effects that will be discussed later, replacing part of the In by Ga in CIS to form $\text{Cu}(\text{In}_{1-x}\text{Ga}_x)\text{Se}_2$ was found to have beneficial impact on the defect density of the material [34] which allowed superior solar cell

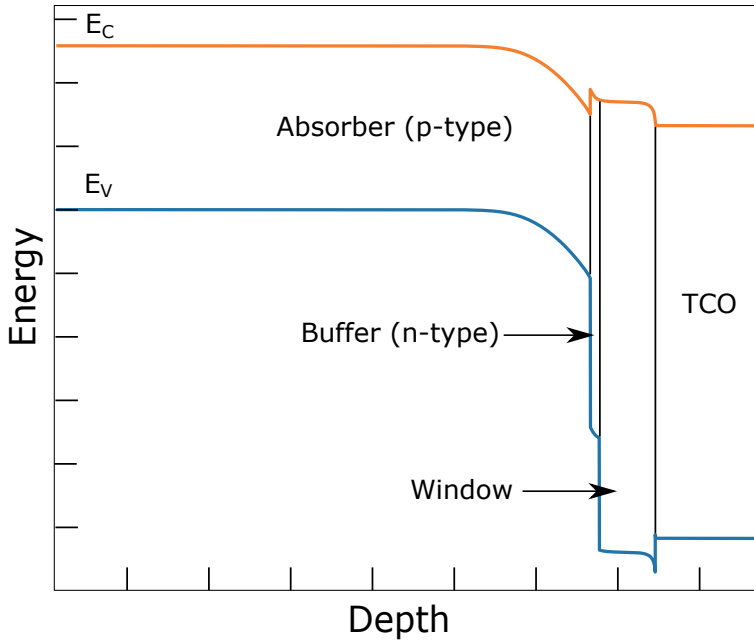


Figure 4.5. Schematic representation of the band diagram of a thin film chalcogenide solar cell.

performance compared to CIS. CIGS exhibits a high absorption coefficient which makes it a very attractive material for absorber layers in thin film solar cells [35]. Ga-containing chalcopyrite formation was revealed to be relatively tolerant to compositional variation as single phase material is obtained in a relatively large compositional window around stoichiometry [36].

CIGS is naturally doped p-type owing to the large number of Cu vacancies forming which create a shallow acceptor level in the bandgap [37, 38]. Deeper defects, potentially harmful for solar cell performance have been heavily investigated [39, 40, 41]. So called N1 and N2 defect states are frequently reported although their contribution to performance loss in recent high quality devices seems relatively minor [42].

Historically, two main processes have been developed for the fabrication of high efficiency CIGS solar cells [16]. The three-stage coevaporation process first demonstrated by the US National Renewable Energy Laboratory (NREL) [43] and later widely adopted by the CIGS community constitutes the basis for modern high efficiency devices including the present world record of 22.6 % [17]. In this process, Cu, In, Ga are thermally evaporated in a Se-saturated atmosphere and condense as chalcopyrite on a heated substrate.

A two step process involving metal stack sputtering followed by high temperature annealing in chalcogen-containing atmosphere is another successful route for high quality chalcopyrite solar cells. Efficiency values above 22% have also been reached following this approach [44].

Besides, intense research efforts have been dedicated to the development of non-PVD based approaches for CIGS deposition [45, 46]. Coating of nano particle-containing or molecular precursor solutions [47, 48, 49] as well as electrodeposition [50] followed by selenization or sulfurization has been explored. Impressive efficiency values up to 17 % have been obtained by a hydrazine-based process [51, 52].

Although CIGS has already reached the commercial stage, research on the material is still ongoing to understand the present device limitations and find ways to push solar cell efficiency closer to the theoretical maximum [42]. In parallel, additional efforts in industrial research focus towards successful up-scaling of technologies to reduce the efficiency gap between laboratory cells and commercial-size devices [53]. An overview of currently most researched topics including alkali post deposition treatments (PDT), alternative buffer layers, optimized grading, among other advanced concepts, is given in [54].

4.3.2 Bandgap grading

As described in section 4.1.3, currents in solar cells are mainly driven by the built-in electric field in the space charge region (drift) and by the gradient of charge carriers in the quasi-neutral regions (diffusion). However, additional contributions to the current also exist. Gradients in energy band edges for instance, have a strong impact on the motion of charge carriers [55]. Such grading can arise as a result of a spatial variation of the electron affinity and bandgap of the material which vary with its composition. This phenomenon is utilized in CIGS solar cells where the concept of bandgap grading is one of the main technological breakthrough of the last decades [56, 57, 58, 59]. Ga incorporation in chalcopyrite mainly raises the conduction band minimum of the material [60], increasing the bandgap from 1 eV for CIS to 1.7 eV for CGS, as shown in Figure 4.6, giving the possibility to improve solar cell performance through bandgap engineering. Equation (4.26) relates the Ga/(In + Ga) ratio or GGI to the material bandgap E_g [61].

$$E_g = 1.02 + 0.67x + bx(x - 1) \quad (4.26)$$

x is the GGI ratio and b is a bowing coefficient where $0.11 < b < 0.24$ [60].

Generally speaking, an increase in bandgap curtails the recombination probability and potentially leads to increased V_{OC} . At the same time, it also reduces light absorption. An optimized bandgap profile is then a carefully engineered

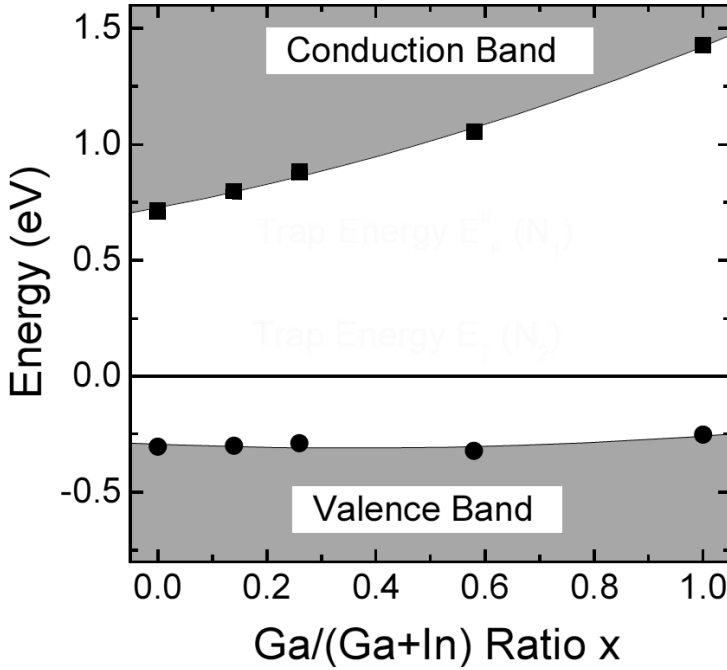


Figure 4.6. Dependence of the valence and conduction band edge position on the Ga/(Ga+In) ratio. Reprinted from [60], with the permission of AIP Publishing.

balance between these two parameters to give the highest performance.

The simplest type of bandgap grading is back grading where the absorber Ga content is increased towards the back contact. In this case, a slope in the conduction band minimum prevents electrons from reaching the back electrode where they would easily recombine and drives them towards the space charge region, increasing the collection probability. Such a grading is believed to be beneficial for solar cell performance in general and particularly effective in devices with thin absorbers where recombination at the back interface is more prominent [58, 62].

Combining back and front grading in a so called "notch" profile by increasing Ga content towards the front of the absorber as well is also possible and can have beneficial effects on the device performance [57, 63, 64]. The main argument in favor of this approach is that an increased surface bandgap can lead to higher V_{OC} values while a high photocurrent can be maintained due to enhanced absorption in the low bandgap region. However, front grading must be designed with great care as it can also lead to a barrier formation for electrons and negatively affect device performance [65].

Bandgap grading can also be realized through the addition of S to partly replace Se in the chalcopyrite lattice. Sulfur incorporation mainly influences the material bandgap by lowering the valence band maximum [60]. Shallow front sulfurization is hence a potential way to reduce recombination at the buffer interface through bandgap widening [66] and hole repulsion [67]. Such grading has also been successfully implemented [68, 53].

On the process side, bandgap grading is accomplished following different strategies. In three-stage coevaporation processes, varying power to the different crucibles in the evaporation chamber leads to in-depth compositional variation of the absorber thin film and hence bandgap grading can be achieved [43]. In two-step processes based on metal sputtering, bandgap grading is achieved through precise thickness control of the layers in the metal stack as well as optimized temperature profiles and chalcogen incorporation from the gas phase during annealing [69]. In both cases, understanding and controlling diffusion mechanisms [70] is of utmost importance.

4.4 $\text{Cu}_2\text{ZnSn}(\text{S},\text{Se})_4$ solar cells

In this section, CZTS material properties are highlighted with a particular emphasis on the thermodynamic stability of the material which sets specific requirements for the solar cell fabrication process.

4.4.1 Material properties

Interest in CZTS arises from concern about the potential future scarcity of elements present in already commercial technologies (In in CIGS and Te in CdTe). It is based on earth-abundant and non-toxic materials and shares favorable optical properties for solar cell applications with the related CIGS material, mainly an absorption coefficient above 10^4 cm^{-1} in a wide wavelength range [71]. However, $\text{Cu}_2\text{ZnSn}(\text{S},\text{Se})_4$ is in fact a quaternary $I_2 - II - IV - VI_4$ semiconductor which complexifies the corresponding phase diagram and multiplies the number of possible secondary phases compared to CIGS [72, 73]. Moreover, the composition stability window of single phase $\text{Cu}_2\text{ZnSn}(\text{S},\text{Se})_4$ is reported to be relatively narrow [74]. Synthesizing an effective absorber layer while avoiding the formation of detrimental secondary phases, such as Cu_2S is hence one of the challenges of CZTS solar cell fabrication. As a result, CZTS absorbers are generally synthesized under Cu-poor and Zn-rich condition for higher performance [75, 76].

CZTS mainly crystallizes in kesterite phase with some degree of Cu-Zn disorder in the lattice [72, 77, 78, 79].

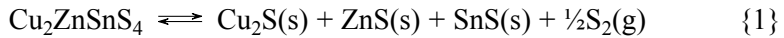
Defect chemistry is very complex in kesterite and the material appears to be strongly compensated [80]. Inherent p-type conductivity follows from high density of Cu vacancies and Cu_{Zn} defects that lead to shallow acceptor levels.

The bandgap of $\text{Cu}_2\text{ZnSn}(\text{S,Se})_4$ can be varied from 1 eV to 1.5 eV depending on the S/Se ratio in the material [81].

CZTS devices have reached efficiency levels close to 13%, however most devices suffer from a relatively large V_{OC} deficit defined as the difference between the voltage corresponding to the material bandgap and the open-circuit voltage. V_{OC} deficit is believed to be caused by recombination in the bulk of the material due to high defect density, losses at the buffer interface, as well as potential fluctuations resulting from lateral bandgap variation and/or electrostatic potential fluctuation [82, 83]. Understanding and overcoming the underlying mechanisms is the main objective of current research on kesterite to enable performance level comparable to CIGS.

4.4.2 Thermodynamic stability and consequences

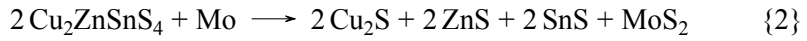
One of the major challenges when trying to fabricate high quality CZTS absorbers is the poor thermal stability of the material when exposed to high temperature. Weber et al. showed that annealing CZTS absorbers in vacuum at 500°C leads to decomposition of the material [84]. The corresponding reaction {1} was further investigated by Redinger et al. [85] and Scragg et al. [86].



SnS has a high vapor pressure so solid SnS created from reaction {1} tends to evaporate hence being lost from the absorber. It was discovered that the reaction is reversible and that providing a sufficient S_2 and SnS pressure during annealing can prevent decomposition. At a normal annealing temperature of 550°C, 2.3×10^{-4} mbar of sulfur partial pressure and a very low SnS partial pressure are needed to ensure the stability of the absorber surface [86]. As a consequence of this instability, a two-step process involving room temperature deposition of precursors followed by crystallization at high temperature in a controlled atmosphere is usually implemented although one step methods also exist [87, 88].

In two step processes, CZTS precursors can be deposited by physical methods such as sputtering [89, 75] and pulse laser deposition [90, 91] or wet processes such as, among others, electrodeposition [92, 93], spray pyrolysis [94, 95], or hydrazine based approach [96], the latter having led to the record device so far [15].

In addition, a detrimental reaction occurs at the back-contact of the solar cell device where molybdenum is directly in contact with CZTS [97].



Reaction {2} was found to be thermodynamically favorable while the corresponding one for CIGS is not. These results suggest that even though molybdenum is an adapted back contact for CIGS solar cells, it is not optimized for CZTS devices. Some more work has to be done in order to identify a more suitable back contact candidate.

5. Thin film deposition by sputtering

Sputtering was first observed by Grove in 1852. In a discharge tube, atoms from the cathode were ejected from the material surface by energetic gas ions and deposited on the tube walls. What was originally considered as an undesirable side effect in experimental set-ups turned out to be one of the most convenient and controllable ways to deposit high quality thin films. In this section, the sputtering phenomenon is introduced followed by its application to the deposition of thin film solar chalcogenide absorbers. Among problems arising from sputtering thin films, working gas entrapment was revealed to be critical in the context of CZTS solar cell fabrication. A detailed description of the underlying phenomenon is proposed at the end of this section.

5.1 Principles and parameters

Sputtering belongs to the so-called physical vapor deposition (PVD) processes. From an industrial process point of view, sputtering exhibits several interesting features such as high deposition rate and tunability that arise from the physical process itself but also from technological development.

5.1.1 Principles of sputtering

When a material is bombarded by energetic entities such as accelerated ions, atoms are ejected from its surface. This phenomenon, depicted in Figure 5.1 is called back sputtering or sputtering.

The simplest kind of a practical sputtering reactor is the so-called diode sputtering system. It is composed of an anode and a cathode facing each other in a vacuum chamber. The sputtering chamber is filled with a gas, most commonly argon. The target material is usually part of the cathode while a substrate is placed at the anode. Applying a potential difference higher than the threshold breakdown voltage between the cathode and the anode results in partial ionization of the gas molecules and the formation of a plasma discharge. The breakdown voltage depends on the gas used, the pressure and the cathode material. The potential of the cathode is kept more negative than the anode, consequently, positively charged gas ions are accelerated towards the target (cathode). If their kinetic energy is higher than the surface binding energy of

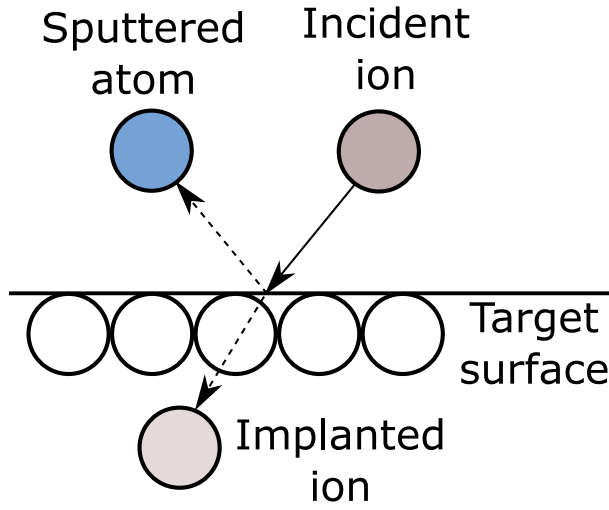


Figure 5.1. The sputtering phenomenon.

the target material, usually assumed to be close to the sublimation energy U , atoms will be sputtered away. A large part of them travel towards the substrate facing the target. The accumulation of these particles on the substrate progressively builds up the thin film. The impact of highly energetic ions on the target surface also induces ejection of secondary electrons. They are accelerated towards the anode, ionizing more gas atoms on their path, sustaining the plasma and hence ensuring a continuous sputtering process [98].

Non-inert gases can also be used during sputtering. This deposition process is called reactive sputtering. Atoms sputtered from the target are combined with gas molecules to form a compound thin film. Sputtering a metallic target in nitrogen or oxygen containing atmosphere is commonly used in industrial or research context to form nitride or oxide thin films [99, 100].

The number of atoms back-scattered after collision of one incident ion with the surface defines the sputtering yield S .

$$S = \frac{\text{atoms removed}}{\text{incident ions}} \quad (5.1)$$

The energy of incident ions has a strong influence on sputtering yield. If incoming ions have less energy than the target surface threshold energy (several tens of eV), the sputtering yield is obviously very low, in the order of 10^{-5} . In the energy regime where ions have a kinetic energy between 10 eV and 1 keV, it is energetically possible to displace atoms at the target surface. Sputtering through collision-cascade phenomenon can take place. This energy range is particularly useful for thin film deposition as the sputtering yield is in the order of unity. In practical applications, the regime above 1 keV is rarely used due to low energy efficiency, and potential damages caused by ion implantation in

the target material. The sputtering yield tends to saturate and even decrease as ions penetrate deeper into the material and more energy is dissipated as heat in the core of the target [98].

5.1.2 Pulsed DC magnetron sputtering

Understanding DC diode sputtering is of primary interest to realize the tremendous potential of sputtering processes for thin film deposition. However, in practice, several issues limit the potential of simple diode sputtering. One of the main difficulties is that the ionization cross section resulting from collision between secondary electrons and gas molecules reaches a maximum for electron energy in the order of 100 eV [101]. In that case, increasing power will not allow process scale up and other strategies must be implemented.

The development of magnetron source in the 1970s was a major improvement for sputtering systems. In a magnetron sputtering configuration, strong magnetic fields are generated close to the cathode. The system architecture is engineered to create magnetic field lines mostly parallel to the target. The magnetic field superimposed to the electric field between anode and cathode constrains the electron motion close to the cathode, enhancing the number of collisions and hence increasing the ionization probability.

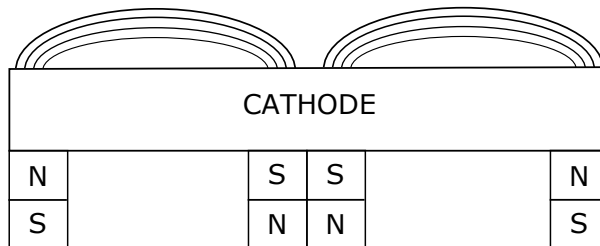


Figure 5.2. Schematic representation of a magnetron sputtering cathode. Magnets with north 'N' and south 'S' poles create a magnetic field close to the cathode surface. Electrons are confined and spiral along the magnetic field lines in the vicinity of the target.

DC magnetron sputtering is a successful and a high deposition rate process for metal thin film deposition. However, in the case of semiconductor targets and furthermore when working with dielectric materials, several problems severely affect the sputtering phenomenon. Indeed, adding a non-metal material at the cathode will induce local surface charges due to the positive ion bombardment. The risk of breakdown is then increased and arcing phenomenon can disrupt the sputtering process significantly. Arcs at the surface can result in ejection of material droplets from the target leading to poor film quality and target surface deterioration. The damaged areas further enhance arcing which eventually destroys the target [102]. Arcing phenomenon is es-

pecially critical in an industrial process where the sputtering power is high and particular care must be taken to prevent crack formation and local target melting.

Avoiding arcing is also critical in reactive sputtering processes. In the case of a metal sputtered in an oxygen containing atmosphere for instance, areas of the target are likely to be covered by a thin dielectric oxide layer resulting from surface reaction between the metal and oxygen. This process, known as target poisoning, promotes surface charge build-up and arcing phenomenon.

Several technical improvements allow a drastic reduction of arcing. One commonly used strategy involves applying an oscillating radiofrequency (RF) potential difference between anode and cathode. The alternating polarity in the sputtering system prevents charge accumulation at the target surface and hence formation of electric arcs. RF sputtering is useful for sputtering of dielectric material or to avoid target charging however the practical implementation is cumbersome due to the need for impedance matching and the deposition rate is typically half of the DC sputtering rate. Moreover upscaling of RF sputtering processes is difficult and costly [103]. To circumvent this problem, a hybrid solution was suggested in the 1990s and successfully applied to the deposition of a variety of thin films. The pulsed DC magnetron sputtering principle is similar to the regular DC process. The main difference is that the sputtering voltage is maintained at its regular level (in the order of 500V) for a fixed “pulse-on” time and then briefly reversed to dissipate potential surface charges. By using such a technique, the deposition rate can be kept relatively high (around 10 $\mu\text{m}/\text{h}$) and the arcing phenomenon is drastically reduced ensuring a stable and industrially-viable process.

Technology development in the last 30 years has enabled dramatic improvement of sputtering processes. Combination of magnetron sputtering configuration and pulsed DC power allows a high deposition rate while limiting the arcing phenomenon. Modern sputtering equipment also exhibits easy scale up, excellent uniformity and a high degree of tunability [104].

5.2 Sputtering from a compound target

Sputtering from binary or even ternary targets is commonly used in industrial and research-related processes (See for instance [105, 106]). It is a fast, relatively easy to implement and scalable process. This sections briefly describes the process of sputtering from a compound target and its consequence on the resulting thin film properties. A short literature survey of CIGS and CZTS absorbers deposited by this method as well as main related results are then given.

5.2.1 Compound target and implications during sputtering process

One of the great advantages of sputtering is that it allows the deposition of alloy thin films that maintain the composition of the target due to the fact that the material is ejected layer by layer [107], provided optimized deposition conditions and system design. However, process parameters such as pressure, atomic weight and angular distribution of ejected species, temperature as well as target surface morphology and target-substrate distance can lead to discrepancies between the target and the film composition and different film properties [108, 109, 110, 111]. Monte Carlo-based simulation is a powerful tool to study the distribution of sputtered particle in the chamber and at the substrate surface [112, 113, 114].

The relationship between sputtering parameters, target composition and film composition was investigated for binary targets [115]. A similar, analytical study in the context of quaternary alloys sputtering is however challenging although the theory has been explored in details [116, 117]. In a simplified picture, compound sputtering can be explained as follows. Elements composing the target material typically have different sputtering yields called partial sputtering yields. The surface composition then differs from the bulk as atoms with higher yield are ejected at an increased rate. This is called preferential sputtering. When steady state sputtering conditions are reached and if diffusion within the target is neglected, the partial sputtering yields evolve towards an equilibrium where constituents are ejected with proportions corresponding to the target bulk composition [118].

It is also important to point out that the ejected flux angular distribution will depend on the nature of sputtered species which can lead to lateral non-homogeneity. Such an effect is minimized if the target has dimensions similar to the substrate and if the substrate-target distance is kept small.

When it comes to complex compounds, co-sputtering of elemental and/or binary targets is usually preferred because it allows to control the composition of the sputtered film by varying the power supplied to the different targets. Sputtering from a quaternary target has other advantages such as rapidity, simplicity (one cathode needed) and repeatability.

5.2.2 CIGS and CZTS sputtered from a compound target

This sections summarizes recently reported results corresponding to the processes studied in the present thesis, namely one-step sputtering of CIGS from a compound target at high temperature and two-step process for CZTS absorbers including room temperature sputtering from a compound target and high temperature annealing in a controlled atmosphere. For other similar CIGS processes, the reader is referred to the very detailed review by the US Naval Research Laboratory published in 2016 [118]. For pure sulfide CZTS, a recent

comprehensive review of sputtering-based processes including single quaternary target is available [89].

One-step CIGS deposition by sputtering from a single target

During one-step, high temperature sputtering of CIGS, the control of the resulting thin film composition is further complexified by selenium loss [119, 120]. When the substrate temperature is increased, sticking coefficients are typically reduced and re-evaporation of Se can take place. The resulting Se-poor films exhibit a high density of Se vacancies, and metal antisite defects, detrimental for device performance [121]. It is worth noting, however, that device efficiencies up to 11% have been reached without additional Se in the gas phase during sputtering [122, 123, 124, 125]. A cell exhibiting over 14% efficiency has recently been achieved by combining a similar process with alkali-post deposition treatments (PDT) [126]. Potassium PDT was found to reduce Se vacancies concentration. Combination with sodium PDT to curtail In_{Cu} formation led to performance increase.

On a side note, two step processes involving post selenization of precursors sputtered from a compound target has led to an aperture area device efficiency of 16.7% [127].

The CIGS process studied in this thesis is considered as one-step since deposition and crystallization at high temperature are simultaneous. Se losses are compensated by the presence of H_2Se in the gas phase during deposition. Power conversion efficiency values in the order of 15 % are reported.

In an industrial context, one step, high temperature processes including simultaneous deposition and crystallization guarantees rapidity and potentially high throughput. Technologically speaking, one advantage is that such process does not rely on diffusion to form bandgap grading as bandgap profiling can be achieved by successively using a set of targets with varying compositions. Some interdiffusion occurs but it is limited due to the short processing time.

CZTS absorber by one and two-step processes based on sputtering from a quaternary target

Thermodynamic instability of CZTS makes one step absorber deposition challenging. However, such process has been implemented and efficiency values between 3 and 6 % have been achieved with this approach [128, 129]. We note that the 6 % cell is obtained through co-sputtering of a CZTS and a ZnS target and exhibits an antireflective coating.

Generally, sputtering from a CZTS target is performed without intentional heating and followed by annealing in a controlled atmosphere. Early work on optical properties of kesterite absorber sputtered from a CZTS target was done by Seol et al. in the beginning of the 2000s [130]. At the time, no devices were made, but it was found that sputtering combined with high temperature annealing leads to kesterite formation. An absorption coefficient of 1.10^4 cm^{-1} and a bandgap of 1.51 eV was measured, which were interesting values for

potential application in solar cells. Over the last ten years, CZTS gained in popularity and more results from quaternary target sputtering were reported. Xie et al. [131] noticed that Zn is usually lost during sputtering leading to a zinc poor film even though the target has a zinc rich composition.

He et al [132] investigated the influence of post annealing on CZTS precursors sputtered from a compound target. A one-hour annealing in Ar/5%H₂S led to drastic crystallinity improvement in the film and release of compressive stress induced by the deposition. The effect of annealing was further studied by Inamdar et al. [133]. A post annealing in N₂ atmosphere at temperatures above 450°C induced compositional shift that was compensated by adding a Cu capping layer prior to thermal treatment. In 2014, He et al. [134] gave more insight into the effect of annealing temperature on the micro structure and the corresponding performance of complete devices. XRD analysis showed that a sulfurization temperature higher than 500°C promotes interdiffusion of elements and reduces the preferential orientation observed at lower temperature while inducing large kesterite grains. The absorber annealed at 550°C was used in a solar cell device exhibiting an efficiency of 2.85%.

Recent efficiency results on two step processes for sulfide CZTS based on sputtering from a quaternary target are around 4 to 5% [135, 136, 137]. The CZTS process developed in this thesis led to similar performance with a maximum efficiency of 5.1%.

5.3 Gas entrapment

As discussed before, in the sputtering process, accelerated gas ions hit the target surface ejecting atoms towards the substrate to grow the thin film. In the vicinity of the target a part of the incident ions tend to be neutralized [138]. Being neutral, they are not affected by the potential difference between anode and cathode and some of them can then be reflected towards the growing film. If these gas atoms have sufficient energy, recoil implantation can occur leading to working gas entrapment in the film as shown in Figure 5.3.

Working gas entrapment can have several detrimental effects on the thin film such as stress and/or modification of the film surface properties [139]. When the processes involved associate sputtering or ion bombardment and thermal treatment, further damages to the film can appear. Blister formation after high temperature annealing has been reported for a variety of thin film materials [140, 141, 142] and was primarily attributed to working gas entrapment and diffusion. During high temperature treatment, diffusion occurs and recrystallization can take place (depending on temperature). Gas atoms trapped in the film travel along the forming grain boundaries and are stopped at local defects in the material, namely dislocations or stacking faults. The local accumulation of gas in the film creates bubble nuclei that grow either by coalescence or Ostwald ripening depending on experimental conditions [142]. The amount of

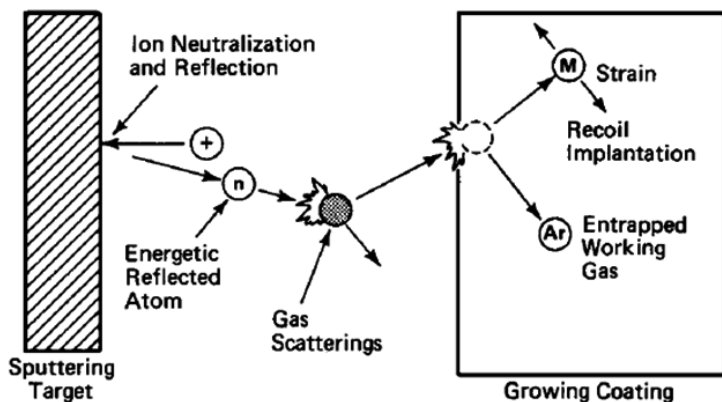


Figure 5.3. A working gas ion is neutralized and reflected at the cathode to yield an energetic atom which passes to the substrate, subject to gas scattering. Impact at the substrate can cause recoil implantation of a surface atom of the metal coating "M" and implantation of the working gas atom, typically Ar. Reprinted with permission from [139]. Copyright 1985, American Vacuum Society.

working gas trapped in the film depending on sputtering parameters was investigated in TaSi₂ by Levy and Gallagher [143] using a model developed in [144] which gives the fraction of trapped gas in the sputtered film. This fraction f is given in eq. (5.2).

$$f = \frac{\alpha N}{\alpha N + R} \quad (5.2)$$

N is the number of Ar atoms bombarding a unit area of the film per unit of time, α is the sticking coefficient of Ar during deposition and R is the deposition rate. This model is used further in the present work to explain blistering effect in CZTS thin films sputtered from a quaternary compound target and subsequently annealed at high temperature.

Part III:

Process and characterization

In-line vacuum, sputtering-based processes for thin film solar cells, characterization equipment and modeling.

6. Process description

This section presents one step sputtering of CIGS from compound targets at high temperature as well as a two-step approach for CZTS absorber based on compound sputtering followed by high temperature annealing.

6.1 General process flow: From stainless steel substrates to finalized devices

The process flow at Midsummer starts with 16 cm wide ASTM 430 stainless steel coils. The standard steel thickness is 0.15 mm. An in-house designed stamping line is used to punch 6-inch semi-square substrates that are automatically stacked in polypropylene cassettes. Each substrate is laser marked with a QR (Quick Response) code to track its path through the factory.

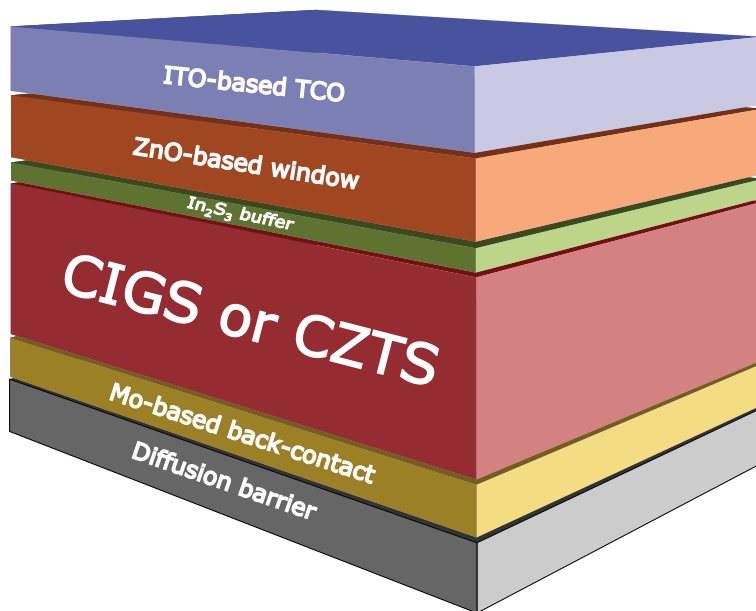


Figure 6.1. Different layers in thin film solar cells produced at Midsummer.

Thorough cleaning is performed through a series of detergent-based washing and rinsing steps. The substrates are then dried and stored at 70°C in a controlled atmosphere.

For solar cell processing, a robotic arm is used to bring substrates to the sputtering equipment and to unload finished devices once their path through the tool is completed. Only one or two sputtering systems are needed, depending on the process considered. Details of the CIGS and CZTS processes are discussed in the following sections. The generic structure of a thin film solar cell produced at Midsummer is shown in Figure 6.1.

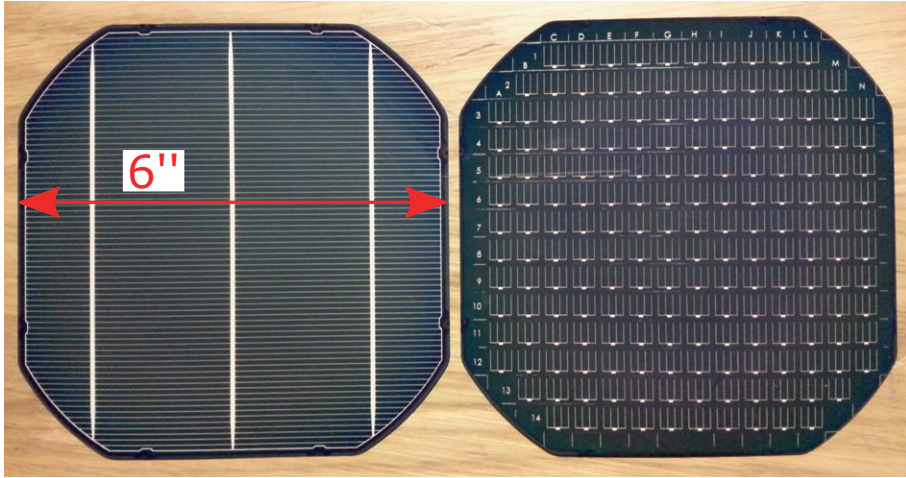


Figure 6.2. Two types of front grid. Left: Standard used in production. Right: Grid pattern used in research which defines 184, 1 cm² solar cells.

The last step consists of a low temperature silver grid screen printing and curing using standard equipment from the silicon industry. Depending on the final application, different silver grid patterns are deposited as shown in Figure 6.2. If the cell is to be further used in solar module production or to assess the performance of the complete device, a silver grid pattern exhibiting current carrying busbars and collecting fingers is used. If the purpose is to study solar cell parameters locally, a special pattern for 1 cm² cells is screen printed and small cells are subsequently manually scribed.

CIGS cells produced for commercialization are interconnected through ribbon soldering and encapsulated between polymer-based back and front sheets to form flexible solar modules as shown in Figure 6.3.

6.2 CIGS: the DUO process

CIGS solar cell processing is exclusively performed in the DUO tool designed by Midsummer. The DUO is a sputtering system based on two main vacuum chambers surrounded by 25 sputtering stations as depicted in Figure 6.4. Stainless steel plates are loaded into the machine via a load-lock mechanism

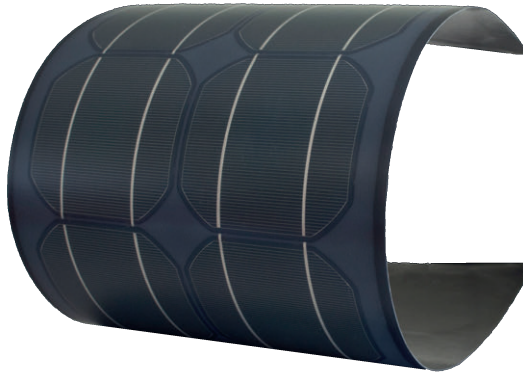


Figure 6.3. An example of a flexible solar module.

and transported by $28 + 4$ mechanical arms. The substrates are successively brought to every deposition chamber by incremental rotations of the arm shaft. Depending on the conductivity of the target material, either DC or pulsed-DC magnetron sputtering is used. Important features of the tool for CIGS solar cell production are resistive heating in close proximity to the substrates, rapid He-based cooling in the intermediate chamber and a variety of process gases available. In full production mode, one CIGS solar cell is unloaded from the DUO every 20 second.



Figure 6.4. The DUO sputtering system.

The process sequence, depicted in Figure 6.5 starts with the deposition of a conductive diffusion barrier to prevent atoms in the steel (mainly Fe) from

reaching the absorber layer where they would have a strong detrimental impact [145, 146]. Alkali doped molybdenum layers covered by a thin undoped Mo layer are then sputtered and form the device back contact. Alkali doping of CIGS through Na and K incorporation has been shown to dramatically enhance CIGS growth and optoelectronic properties resulting in device performance improvement [147, 148, 149, 150]. In the present process such a doping is realized by diffusion of the alkali elements from the back contact into the absorber during high temperature processing.

The substrate temperature is then increased and the sample is brought to chamber B where the absorber is sputtered. CIGS absorbers are synthesized using compound targets. The deposition sequence starts with CGS sputtering. The bulk of the absorber is sputtered from CIGS targets with varying GGI ratio, depending on the desired bandgap profile. The absorber deposition ends with sputtering of a Cu and Ga-poor compound.

After a fast cool-down process, the sample is transferred to the second half of chamber A where an In_2S_3 buffer layer is deposited. To complete the solar cell, a resistive window layer is sputtered followed by an ITO-based transparent conductive oxide layer.

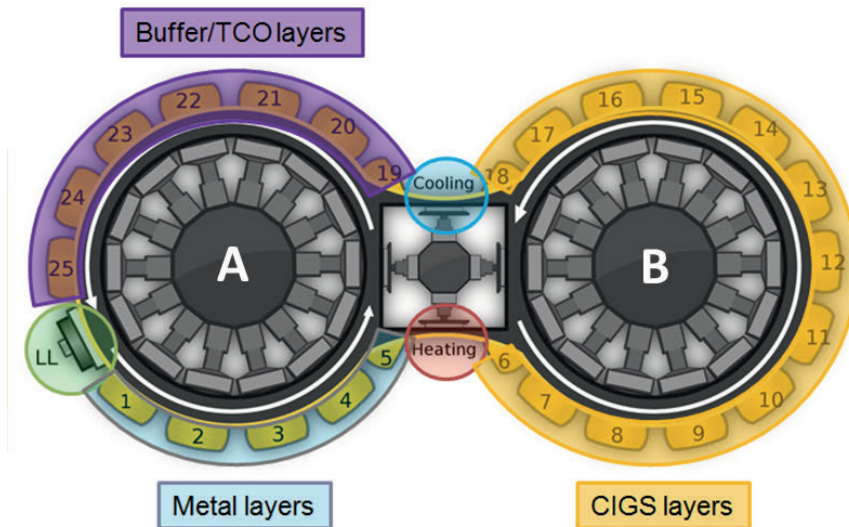


Figure 6.5. The DUO process for CIGS cells.

The DUO is normally run in production mode where 30 substrates are present simultaneously in the system, maximizing throughput. A so-called one-by-one (OBO) mode where only one solar cell is processed at a time is also used for research and development purposes where a greater versatility is a strong advantage and a high throughput is not required.

6.3 CZTS sputtering and annealing

The CZTS process starts with diffusion barrier and back contact pre-sputtering of stainless steel substrates in the DUO following a process similar to the one used for CIGS. The substrates are then transferred to a second sputtering tool, a re-built SMO unit from Ulvac, for the rest of the process sequence. A schematic top view of the tool is shown in Figure 6.6. The SMO unit was initially designed for the optical disc industry and its architecture is based on a main vacuum chamber and 7 sputtering stations. To meet the requirements of solar cell processing, the tool was modified to include a variety of process gases, fast heating capability, and a sputtering station was converted into an annealing chamber.

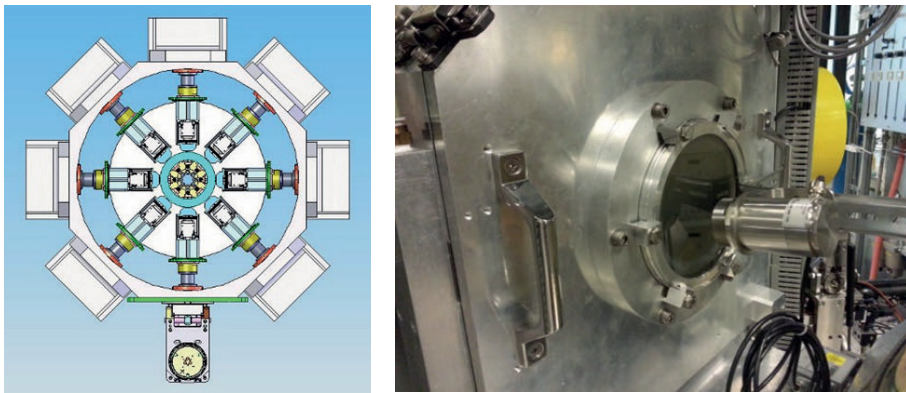


Figure 6.6. Left: A schematic top view of the SMO unit with a main vacuum chamber, 8 mechanical arms and 7 sputtering chambers. Right: Pyrometer reading the sample temperature through the annealing chamber quartz window.

CZTS absorber deposition is performed using a compound target. The freshly sputtered CZTS precursors are then brought into the annealing station, without vacuum breaking. A mix of Ar-10% H_2S is let into the chamber through a needle valve until the pressure reaches 500 mbar. A controlled current is supplied to resistive elements located at the back of the substrate raising its temperature up to 550 °C. A pyrometer pointing towards the absorber material through a quartz window monitors temperature as also depicted in Figure 6.6. After 15 minutes, the heaters are switched off and the temperature of the sample gradually decreases. When it reaches 200°C, the chamber is pumped down again to high vacuum and the sample is brought to the following sputtering chamber for In_2S_3 buffer layer deposition. Similar to the CIGS process, the cell is finalized by the addition of a ZnO resistive window layer and an ITO front electrode.

7. Characterization methods and simulations

This chapter presents the different characterization methods that were utilized during this thesis as well as programs and software used for simulation.

7.1 Material and device characterization

Characterization is an important part of the present work. While CZTS-related studies are more focused on the analysis of the absorber material properties, mainly crystal structure and composition, the CIGS investigations also involve several device characterization techniques.

7.1.1 Scanning electron microscopy (SEM) and energy dispersive x-ray spectroscopy (EDX)

Scanning electron microscopy is based on the detection of electrons escaping from a material as a result of an incident electron beam excitation. The incident electrons can be back-scattered and collected to produce an image of the sample. Energetic incident electrons can also excite core electrons from the studied material and transfer enough energy for them to be ejected from the surface. These secondary electrons can then also be collected and detected. By combining local excitation and two dimensional scan of the sample, a rectangular image of the material surface can be obtained.

Penetration of high energy electrons in a material also induces excitation of some core electrons without enough energy to eject them. When those electrons relax to lower energy states, x-ray radiation is emitted. The radiation energy is normally characteristic of the atom that emitted it. An appropriate x-ray detector coupled to data treatment can theoretically allow to evaluate the composition of the sample probed. This is the measurement principle of Energy-Dispersive X-ray Spectroscopy (EDX or EDS). However, in practice, electron slowing effects as well as other penetration depth-related effects limit the ability of EDX systems to give accurate absolute compositional data. Relative results can still be obtained and give interesting information about the sample composition.

In this project, two SEMs are used. A Hitachi S4800 SEM equipped with a Bruker AXS X flash 4030 EDX detector is available at Midsummer. A Merlin SEM from Zeiss and a 80X Max silicon drift detector from Oxford instruments

from Uppsala university are also used for sample characterization. SEM images of sample cross sections are of first interest to assess the crystallinity of CZTS and CIGS absorbers and possibly identify secondary phase segregation. Absorber thickness can also be extracted from those images. Example of CIGS absorber SEM images are given in Figure 7.1.

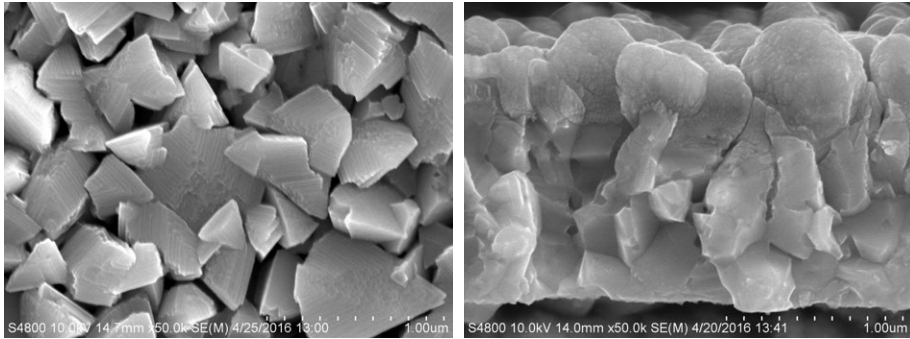


Figure 7.1. Left: SEM top view of a CIGS absorber. Right: SEM cross-section image of a CIGS solar cell. The back contact is not present in the picture.

EDX is a quick and convenient way of measuring an approximate absorber composition. However, one has to keep in mind a few important considerations about EDX measurement for CZTS and CIGS. The principal drawback of that characterization technique is that the characteristic EDX pattern for molybdenum and sulfur overlap. A quantification of sulfur on a molybdenum containing sample can then turn out to be inaccurate. One possibility is to deposit the same material on a test molybdenum-free substrate.

7.1.2 X-ray fluorescence (XRF)

Another convenient composition analysis method used to study the composition of chalcogenide absorbers is X-Ray Fluorescence (XRF). The measurement relies on the excitation of the sample by an x-ray beam. Similarly to EDX, electrons from the sample that were excited by the incoming radiation eventually relax. Part of this relaxation is a radiative process. The resulting characteristic x-rays are detected and composition information of the sample can be extracted. The x-ray radiation emitted by the sample is maximized when the excitation wavelength is close to the characteristic absorption of the analyzed material. As a result, XRF tools usually combine an x-ray source and a secondary target to create the appropriate radiation, depending on the element of interest. XRF measurement requires calibration for absolute composition assessment.

In the present thesis, XRF is mainly used for CZTS analysis. The composition in Cu, Zn and Sn is determined using a calibration sample for which an

absolute composition was measured with Rutherford Back-Scattering (RBS) technique [151]. The tool used is a PANalytical Epsilon 5 x-ray fluorescence system. Cu and Zn analyses are run using a Ge secondary target and Sn analysis using a BaF₂ secondary target.

7.1.3 X-ray diffraction (XRD)

X-ray diffraction is probably one of the most commonly used characterization techniques for thin film analysis. The material of interest often exhibits a certain degree of crystallinity. For thin film solar cells, the absorber is usually polycrystalline i.e. it is composed of crystallites separated by grain boundaries. Inside one grain, the atoms are ordered in a lattice. Interaction of x-rays and a material lattice alter the incoming radiation through diffraction. By analyzing the dependence of the diffracted x-ray intensity and the relative angle between x-ray source, sample and detector, information about the crystallinity of a sample can be derived. Additionally, XRD allows to discriminate other phases in the material studied.

A typical configuration for an XRD system is the Bragg-Brentano setup where the angle between the incident beam and the surface normal is the same as the angle between this normal and the detector line of sight. This configuration leads to θ - 2θ scan. A potential issue when thin films are studied in θ - 2θ XRD is the relative weakness of the signal coming from the film itself compared to the large contribution from the substrate. An effective work-around is to use the so-called grazing incidence XRD or GIXRD configuration where the angle between the surface and the incoming x-ray beam is kept at a fixed, low value, maximizing the interaction volume in the thin film and the corresponding signal.

As discussed before, in the Cu-Zn-Sn-S system, several secondary phases can form and some of them are particularly detrimental for the final solar cell. Detecting them and understanding their formation is one of the keys towards high quality material formation. XRD analysis is then a helpful tool, both to identify potential secondary phases and evaluate the degree of crystallinity of the sample (grain size, preferential orientation). XRD also has limitations when it comes to CZTS material analysis. Secondary phases such as ZnS and Cu₂SnS₃ (CTS) exhibit crystal structures similar to kesterite making them indistinguishable from XRD results. However, kesterite has a more complex pattern showing more peaks than the other compounds mentioned. It is then possible to verify the presence of kesterite phase in a sample but it is difficult to rule out ZnS or CTS formation by simply looking at the results of XRD analysis.

CZTS XRD patterns are acquired with a Siemens D500 diffractometer in Bragg-Brentano focusing geometry.

For GGI investigations in CIGS absorbers, GIXRD configuration with an incidence angle of 0.5° in a Siemens D5000 diffractometer was used. The inclusion of Ga in CIS leads to a reduction in lattice parameter inducing peak shift in XRD pattern. A comparison of the chalcopyrite-related reflexes and reference CIS and CGS patterns can then be used to approximate the material composition.

7.1.4 Raman spectroscopy

In Raman spectroscopy, a monochromatic light source (a laser) is aimed at the material. The beam is scattered by the sample and most of the scattered light conserves its original frequency. This phenomenon is called Rayleigh or elastic scattering. The remaining very small part of it experiences a shift in energy (called Raman shift) due to the interaction of the electromagnetic radiation with the vibrational states of the chemical bonds present in the sample. Plotting the intensity of the scattered light versus Raman shift gives a characteristic spectrum for a specific material.

For CZTS analysis, regular green light Raman is used to assess the crystallinity of a sample and allows to detect secondary phases. Distinction between kesterite and ZnS is, however, still difficult. Using a UV laser excitation allows to overcome this difficulty. XRD and Raman analysis is a powerful combination to characterize the microstructure and detect secondary phases.

7.1.5 Plasma profiling time of flight mass spectrometry (PP-TOFMSTM)

Composition depth-profile measurement is of paramount importance when studying bandgap gradients in CIGS solar cells. As discussed in section 4.3.2, an in-depth variation of the relative In/Ga content of the absorber is used as a technological tool to induce in-depth bandgap variation in CIGS absorbers, potentially leading to charge carrier collection improvement.

Plasma profiling time of flight mass spectrometry (PP-TOFMSTM, Horiba Scientific) is an emerging depth profiling technique [152, 153, 154, 155]. During a PP-TOFMSTM measurement, an argon plasma is created in the vicinity of the sample and ions are accelerated towards the film by a potential difference. Sputtering phenomenon occurs and the ejected particles are in turn ionized. A time of flight mass spectrometer is then used to identify the ejected species and build a composition depth-profile. The high plasma density created in a PP-TOFMSTM system allows to maximize the sputtering rate leading to measurement times of a few minutes for a film thickness in the order of a micrometer.

7.1.6 Current-voltage measurements

Current-voltage (IV or JV as commonly used in photovoltaics) measurement is probably the most common solar cell analysis method. It is generally performed using a solar simulator, providing an irradiance close to the AM1.5 spectrum presented in Figure 4.2. By sweeping the voltage applied to the device and measuring the current supplied to or generated by the solar cell, a current-voltage curve can be obtained. Performance parameters including open-circuit voltage, short-circuit current, fill factor and power conversion efficiency are obtained from such a measurement. From a fitting procedure to the diode equation (4.20), more advanced parameters such as the ideality factor and the reverse saturation current density, introduced in section 4.1.4, can be extracted as well. Fitting procedures of the illuminated diode equation can be rather complex and other approaches based on graphical methods and linear fits have also been developed to determine the main parameters of interest [156].

In solar cell production lines, IV measurements are typically used to sort devices depending on their performance. In this thesis, IV curves are measured on 6-inch full size devices and on 1 cm² cells. In both cases, a calibrated, ABB class, Newport 91193-1000 solar simulator is used. For full size devices, a set of current and voltage probes uniformly arranged along n probe holders, n being the number of busbars on the cell, contact the front of the device. The corresponding set-up is shown in Figure 7.2. The cell substrate being conductive, the back electrode is directly contacted through the stainless steel by a water-cooled brass plate. In accordance with standards for IV measurements, the brass plate is normally maintained at a temperature of 25°C. For 1 cm² device measurements, Kelvin probes are used to contact the front of the device. The voltage sweep and current measurement/supply are carried out either by an Agilent 2722A or an Advantest R6244 source-meter depending on the size of the device and the resulting current level.

7.1.7 Quantum efficiency

Quantum efficiency is a powerful technique to characterize both electrical and optical current losses in a solar cell. During quantum efficiency measurements, a monochromatic light beam is shone onto the sample and the generated photocurrent is measured. The quantum efficiency is then defined as the ratio between the number of incident photons of a particular energy or wavelength and the number of generated electron-hole pairs collected at the contacts as expressed in Eq. (7.1).

$$QE(\lambda) = \frac{N_e}{N_p} = \frac{J(\lambda)}{q\phi_i(\lambda)} \quad (7.1)$$

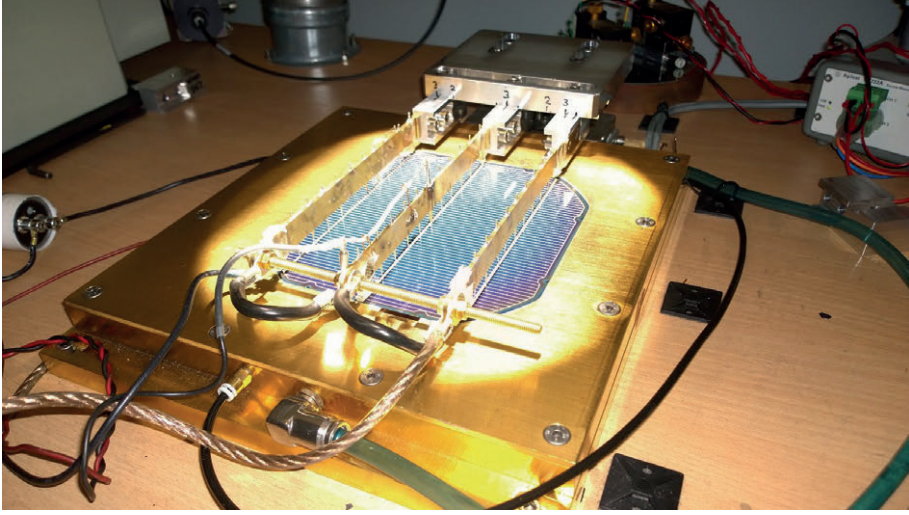


Figure 7.2. JV curve measurement set-up for 6-inch solar cells.

N_e is the number of collected electrons in a given time t which is equal to the output current $J(\lambda)$ multiplied by t and divided by the elementary charge q . N_p is the number of incident photons during the same time t which corresponds to the photon flux $\phi_i(\lambda)$ multiplied by t . By varying the incoming light beam wavelength in the spectral range where the device is active (typically 300 - 1200 nm for CIGS devices), one can determine the wavelength dependence of the photo-generation and collection processes.

Integrating the product of quantum efficiency and light source spectral irradiance over all relevant wavelengths gives the short-circuit current of the device which can then be used to calibrate a solar simulator for JV measurements.

$$J_{SC} = q \int QE(\lambda) \phi_{AM1.5}(\lambda) d\lambda \quad (7.2)$$

Two types of quantum efficiency measurements can be distinguished. If the incident photon flux on the sample surface is considered in the calculations, the measured value corresponds to the device external quantum efficiency (EQE). Some photons are typically lost by reflection at the sample surface or transmitted through the solar cell. If these losses are taken into account by subtracting the reflectance and transmittance spectra to the quantum efficiency spectrum, the internal quantum efficiency (IQE) of the device is obtained. The IQE is then defined as the ratio between the number of photo-generated charge carriers collected at the device contacts and the number of photons *absorbed* by the device.

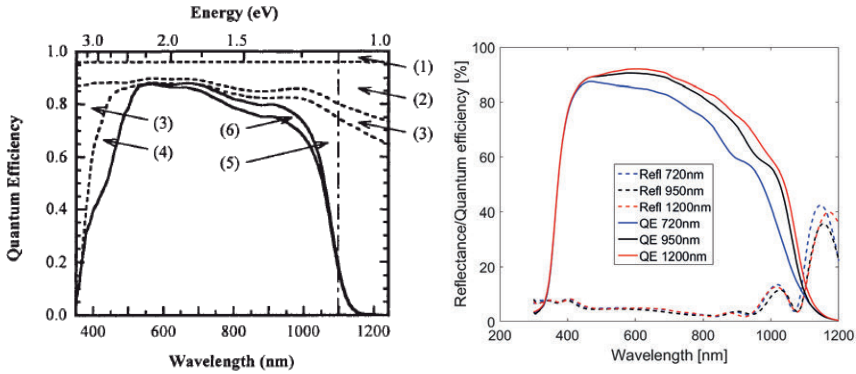


Figure 7.3. Left: Different current losses identified in EQE. The explanation is given in the text. Reprinted from [156], with the permission of John Wiley and Sons. Right: Impact of absorber thickness on the EQE of a CIGS solar cell. Reflectance spectra are also shown.

Different types of current loss can be identified in a QE measurement as schematically depicted in Figure 7.3. However, the origin for such losses is sometimes difficult to determine. One way to distinguish between optical losses, for instance in solar cell top layers, and electrical losses related to poor collection of charge carriers, is to apply a reverse bias to the device. The resulting increase in space charge region width enhances the junction collection properties. Major losses observed in QE measurements are listed below [156]. The numbers correspond to Figure 7.3:

- (1) Shading from the grid.
- (2) Front surface reflection (in the case of an EQE spectrum).
- (3) Absorption in the window/TCO layer
- (4) Absorption in the buffer layer which is less critical when larger bandgap materials such as In_2S_3 or $\text{Zn}(\text{O},\text{S})$ are used compared to CdS .
- (5) Incomplete absorption in the absorber layer. Such effect is particularly critical for thin absorbers as illustrated on the right-hand side of Figure 7.3.
- (6) Non-optimized collection of charge carriers that can originate from recombination in the bulk or at the back contact interface.

7.2 Simulations

Two types of simulations have been conducted in this thesis. 1D solar cell device simulation starting from physical properties of the different layers is conducted using SCAPS. To relate local solar cell parameters to the performance of a full size 6-inch device, a 2D network model based on the solar cell equivalent circuit is built in a SPICE environment.

7.2.1 SCAPS

Solar Cell Capacitance Simulation or SCAPS is a free software dedicated to 1D simulation of thin film solar cells developed at the Department of Electronics and Information System of the University of Gent in Belgium [157, 158, 159]. SCAPS operating principle is based on solving the fundamental semiconductor equations discussed in section 4.1 namely the Poisson equation, shown in one dimension in eq. (7.3), to relate the charge ρ and the electrostatic potential V , and the continuity or ambipolar transport equation discussed in section 4.1.1.

$$\frac{\partial}{\partial x} \left(\epsilon_r \frac{\partial V}{\partial x} \right) = -\frac{\rho}{\epsilon_0} \quad (7.3)$$

Where ϵ_0 is the vacuum permittivity and ϵ_r is the considered material relative permittivity.

A SCAPS model includes up to seven layers for which the main physical parameters are user-defined with a possibility of grading in most cases. This feature is particularly adapted to the study of bandgap grading in CIGS solar cells. Recombination through trap states in a semiconductor layer bulk is taken into consideration and described by the SRH formalism. Interface recombination due to discontinuities in band edges is also taken into account in SCAPS.

Different types of simulations can be conducted including JV curves, capacitance-voltage and capacitance-frequency responses as well as quantum efficiency spectra.

Finally, the optical behavior of a device, is accounted for by the inclusion of an optical filter at the front surface of the simulated stack. One example is the reflectance spectrum of a complete CIGS solar cell presented in Figure (7.4)

In this thesis, a SCAPS model for CIGS solar cells produced at Midsummer is set-up. The main differences in this model compared to most devices simulated in research context is a relatively low minority carrier lifetime in the absorber and a thin CIGS layer resulting from process requirements. A simulation study on different bandgap grading accompanied by experimental verification is conducted.

7.2.2 SPICE

SPICE (for Simulation Program with Integrated Circuit Emphasis) is a circuit simulation program used for a large variety of circuit analysis including DC, AC, steady state and transient behaviors. SPICE allows to simulate the response of circuits involving all basic passive components such as resistors, capacitors, inductors as well as different types of power sources among many other devices. Simply speaking, SPICE treats each component with its characteristic equation and applies a modified nodal analysis based on Kirchhoff's

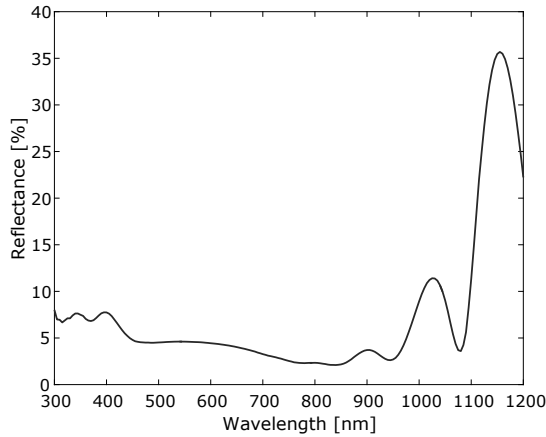


Figure 7.4. Reflectance spectrum measured at the surface of a CIGS solar cell and used as an optical filter in SCAPS simulations.

circuit law to formulate global circuit equations and calculate local potentials at nodes and currents in branches. It was originally developed at the Electrical Engineering and Computer Sciences department of the University of California at Berkeley [160]. SPICE is a public-domain software for which numerous free and commercial distributions are available.

Graphical user interfaces typically used for simple SPICE circuits are convenient but they are limited to a small amount of components. For more complex circuits, a netlist is written which contains a list of all components in the circuit, their characteristics as well as the nodes between which they are connected. Such approach makes the visualization of the circuit more challenging. It is, however, more powerful in the sense that a circuit netlist can be written automatically via another program.

A typical equivalent circuit representing the electrical behavior of a solar cell according to the one-diode model is shown on the left-hand side of Figure 7.5. It is composed of a diode representing the PN junction in the dark, a current source to simulate the photocurrent and a series and shunt resistances which origins are described in section 4.1.4. A large solar cell can then be treated as a parallel connection of numerous small devices, each of them exhibiting its proper solar cell parameters. In the framework of a uniformity study conducted on 6-inch solar cells, the performance of 184, 1 cm² solar cells uniformly distributed over the sample surface as depicted in Figure 6.2 is assessed and the corresponding solar cell and diode parameters are determined. The sheet resistance of the TCO layer is also measured. These parameters are then used as input in a SPICE network model shown in Figure 7.5 to relate local solar cell properties to the performance of the full size device.

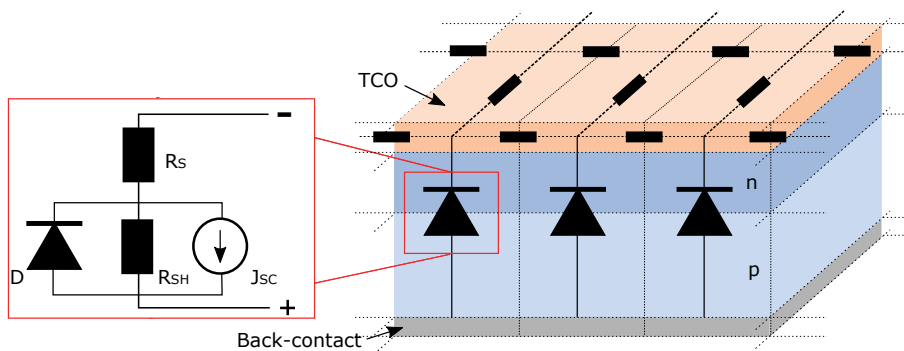


Figure 7.5. A large solar cell simulated as a combination of small devices connected in parallel. The sheet resistance of the TCO layer is taken into account while the back contact is considered as a perfect conductor.

Interfacing SPICE and Python allows to combine simulation and post treatment of the results such as advanced parameters extraction and data visualization.

Part IV:

Results and discussion

8. Improvement of thin film solar cell absorber layers and uniformity of 6-inch devices

This chapter summarizes the main results included in the scientific publications attached to this thesis. CZTS absorbers are first explored and the impact of high temperature annealing in sulfur-containing atmosphere on the material crystal structure, morphology and device performance is investigated. Blister formation during annealing is identified as the main limitation for reaching higher performance. This phenomenon is studied in details and solutions are provided.

Improvement of absorber layer in industrial CIGS solar cells is the focus of the second part of this chapter. Based on SCAPS simulations, an optimized GGI profile for the absorber is determined and experimentally implemented. Performance improvement and successful transfer to production process are shown.

Finally, the uniformity of both CIGS and CZTS 6-inch devices is examined.

8.1 Annealing CZTS absorbers (Paper I and II)

The annealing step is crucial for the formation of large kesterite grains and well-behaved solar cells. Another parameter that influences the growth of the material as well as its optoelectronic properties is sodium incorporation [161]. The influence of sodium from the MoNa layer on the performance of the corresponding CZTS solar cell is briefly investigated in Paper I entitled "Influence of hydrogen sulfide annealing on copper-zinc-tin-sulfide solar cells sputtered from a quaternary compound target". It is shown that the presence of sodium drastically improves the device photocurrent but no clear correlation between the thickness of the MoNa layer and the performance of the solar cell could be established.

The core investigation of Paper I is to assess the influence of annealing temperature on the crystallinity and the composition of CZTS absorber layers and on the performance of the corresponding complete devices. It is shown that increasing the annealing temperature from 420°C to 550°C enhances the grain size from a hundred nanometers up to more than a micrometer as shown in Figure 8.1.

The composition also comes closer to stoichiometry with increasing temperature. However, performance of the complete device reaches a maximum

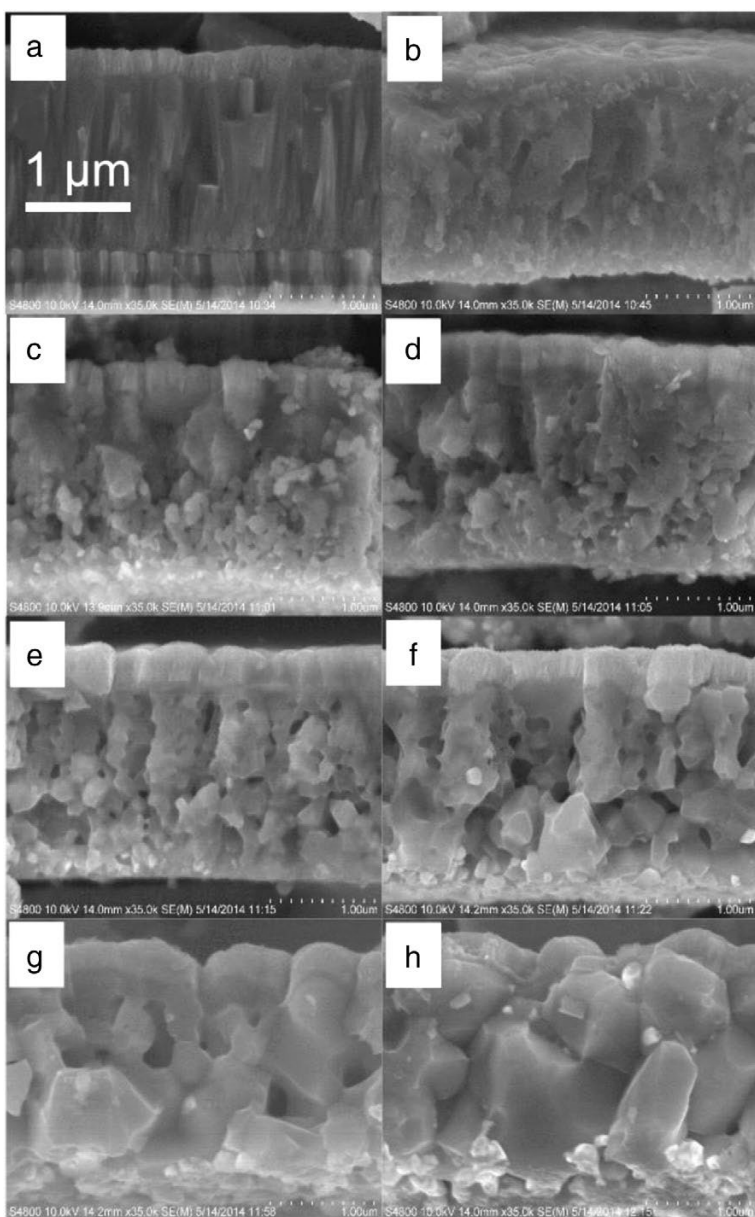


Figure 8.1. SEM cross-section images of CZTS thin films after room temperature deposition (a), and annealed at 420°C (b), 450°C (c), 475°C (d), 490°C (e), 510°C (f), 525°C (g), 550°C (h).

for an annealing temperature of 510°C. The solar cell parameters as a function of annealing temperature are displayed in Figure 8.2.

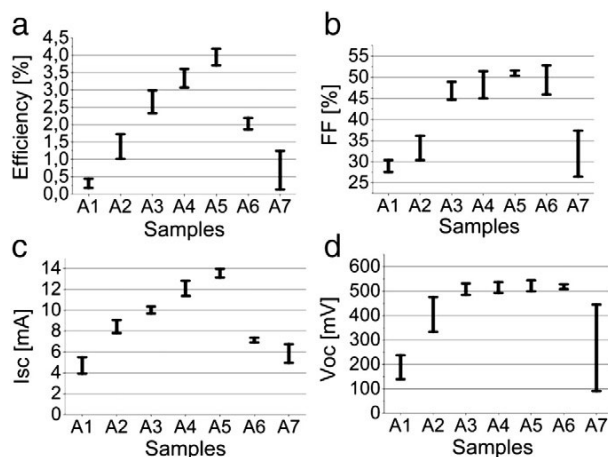


Figure 8.2. Solar cell parameters of devices annealed at temperatures between 420°C and 550°C. The temperature steps are the same as in Figure 8.1

It is observed that annealed absorbers exhibit blisters and annealing temperatures above 510°C lead to the formation of a high density of blisters that degrades the corresponding device performance. The best solar cell in that study exhibits 4.2% efficiency.

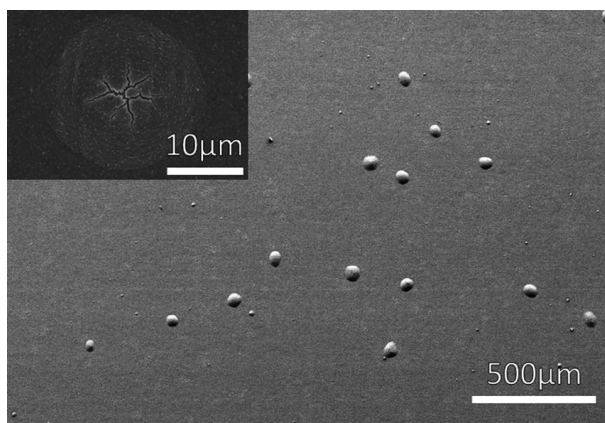


Figure 8.3. SEM top view of a CZTS absorber after annealing at 550°C

Understanding blister formation is of first importance in order to prevent this phenomenon and improve the absorber quality and uniformity. A detailed investigation of the CZTS thin film structure and composition as well as process parameters is conducted in “Investigation of blister formation in sputtered CZTS absorbers for thin film solar cells” (Paper II).

While blister formation does not depend on substrate type, a strong correlation with sputtering parameters is observed. Precursors deposited at low sputtering pressure, typically below 10^{-3} mbar develop blisters during annealing while increasing sputtering pressure to 10^{-2} mbar almost prevents blistering effect. It is initially believed that segregation and evaporation of a high vapor pressure secondary phase at the bottom of the absorber during annealing results in local over-pressure below the film causing blisters. XRD and Raman analysis reveal neither any specific difference in the microstructure nor in condensation of secondary phases when comparing results from samples with and without blisters. The Raman patterns measured on three different strategic locations on a sample after peeling off the absorber layer are shown in Figure 8.4.

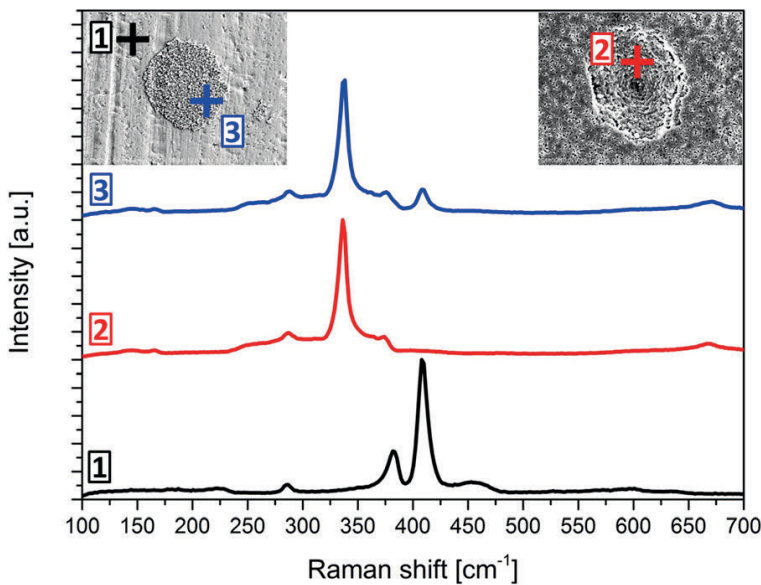


Figure 8.4. Raman patterns measured at a blister location. At the top left corner, an SEM top view of the sample after absorber lift-off is shown. Some material remains on the surface of the back contact layer. At the top right corner, the back of the lifted-off absorber is depicted. Raman measurements are performed on the exposed back contact (1), on the back of the absorber after lift-off (2) and on the material remaining on the back contact at a blister location (3).

Raman patterns only exhibit characteristic kesterite and MoS_2 peaks ruling out secondary phase segregation. Composition measurement leads to the same observation. It is then concluded that blister formation is not due to the film material itself.

A careful analysis of EDX spectra from the CZTS precursors shows that argon, used as sputtering gas, is trapped in the film during deposition. Sputtering

gas entrapment in the growing film has been reported for a variety of materials [139, 162, 163, 164]. Blistering effect as a result of sputtering gas entrapment is already discussed and explained in section 5.3. Briefly speaking, gas atoms or molecules trapped in the film during sputtering can migrate during subsequent high temperature treatment and accumulate at local structural defects to form blisters. Increasing pressure or substrate temperature during sputtering reduces the probability of gas entrapment and hence alleviate blister formation[143]. Using larger working gas atoms (Kr for instance) is another way to reduce gas entrapment as it is more difficult for larger atoms to find an accommodation site [165]. Indeed and as illustrated in Figure 8.5, the blister density greatly reduces when the size of working gas atoms is increased.

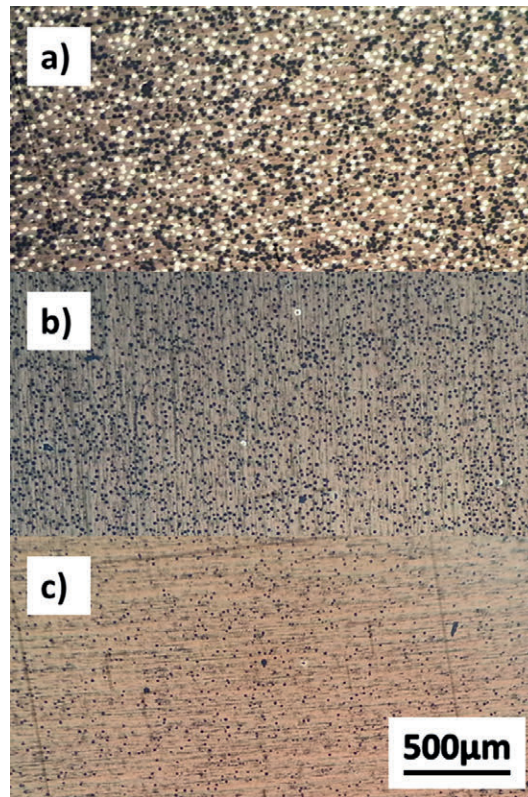


Figure 8.5. Optical microscope images of absorbers after annealing where different sputtering gases, namely Ne (a), Ar (b) and Kr (c), are used. Bright spots in (a) are burst blisters (material peeled-off) while dark dots are not-burst blisters. The blister density is reduced with increasing atomic radius of sputtering atoms.

It has recently been pointed out that stress in the film is an important factor contributing to blister formation in CZTS absorbers [166]. Substrate temperature and sputtering pressure affect the stress in the film which in turn may

influence blister formation. The difference in blister density observed with different sputtering gas in Paper II is however challenging to explain with stress-related considerations. Generally speaking, blister formation is a complex phenomenon and the main root cause certainly varies from one process to another.

8.2 Bandgap grading for industrial CIGS solar cells (Paper III)

As discussed in section 4.3.2, appropriate bandgap grading is of great importance for CIGS device performance. The approach to bandgap grading optimization followed in Paper III, "Ga-grading and Solar Cell Capacitance Simulation of an industrial Cu(In,Ga)Se₂ solar cell produced by an in-line vacuum, all-sputtering process", consists of two phases. First, the impact of different bandgap profiles on device characteristics is tested numerically using SCAPS simulations [157]. Once an optimal configuration is identified, it is experimentally implemented to verify the corresponding gain. The industrial process used to fabricate CIGS solar cells sets additional constraints on material properties, such as limited minority carrier diffusion length, and physical parameters, such as restrictions in terms of absorber thickness.

Setting up a correct model for the device under study is necessary before exploring the impact of bandgap grading. For this purpose, characterization of standard research 6-inch cells produced at Midsummer is first conducted. x-ray diffraction combined with PP-TOFMSTM is used to determine the in-depth compositional profile of the standard absorber, as shown in Figure 8.6. It is found that the profile corresponds well to the different sputtering targets used during the deposition process although Ga-In interdiffusion occurs due to high temperature processing.

The absorber doping level is extracted from CV (capacitance-voltage) measurement while optoelectronic properties of CIGS and top layers are obtained from literature and optical measurements.

To verify the model, solar cells with different absorber thicknesses are simulated and fabricated. Simulations and measurements of JV curves and EQE agree relatively well, especially for an absorber thickness of 950 nm, the standard thickness used in production. A comparison of simulated and measured EQE curves is also shown in Figure 8.6. Significant differences are observed for thinner absorber solar cells. Modeling of thin absorbers is challenging due to potentially different properties resulting from shorter exposure to high temperature during processing, among other causes, as further discussed in the paper.

Selection of an optimal bandgap grading compatible with process requirements and leading to improved device performance is the main objective of

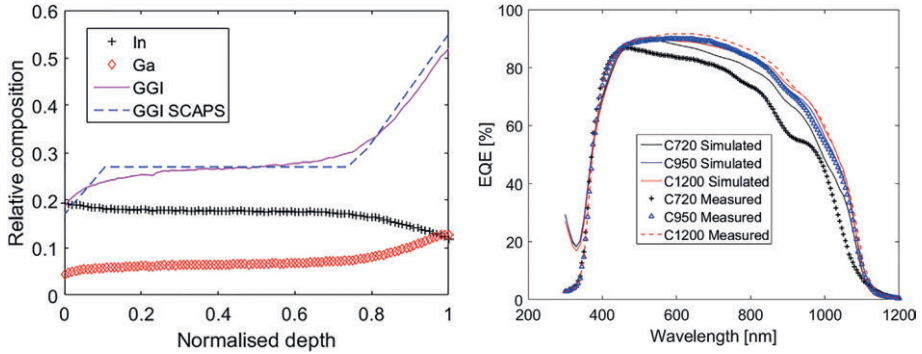


Figure 8.6. Left: PP-TOFMSTM composition depth profile of a standard CIGS cell and corresponding GGI. The GGI used for SCAPS simulation is also shown. Right: Comparison of simulated and measured EQE curves for the standard GGI profile with different absorber thicknesses, namely 720 nm (C720), 950 nm (C950) and 1200 nm (C1200).

this investigation. The standard profile already exhibits a sharp back grading. Such feature is conserved in the new profile and a constant GGI reduction throughout the absorber depth is added as depicted in Figure 8.7 to improve charge carrier collection.

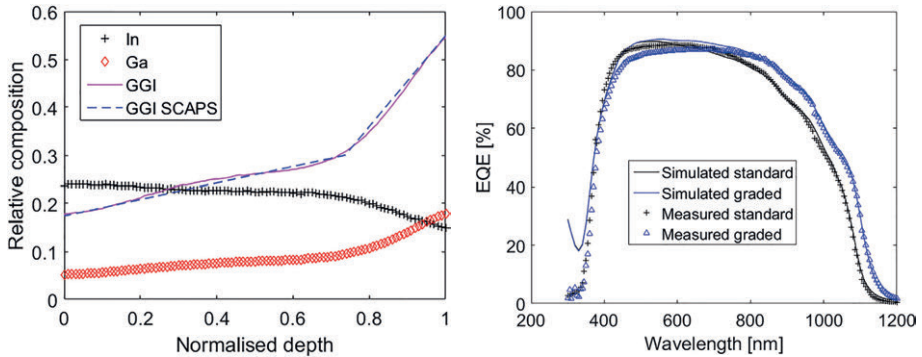


Figure 8.7. Left: GGI profile with additional bulk grading as simulated in SCAPS and measured in PPTOFMS. Right: Comparison of EQE curves from cells with standard and additionally graded absorbers.

Enhanced collection is indeed observed in simulated and measured EQE curves in Figure 8.7 and while corresponding cells show a slightly reduced open-circuit voltage probably due to a smaller bandgap, a large increase in current leads to power conversion efficiency improvement in the order of 1% absolute for full size 6-inch solar cells. Figure 8.8 shows a comparison of the two gradients in terms of corresponding solar cell parameters.

Successful transfer to production process, where thorough process parameters optimization is performed at all steps, is demonstrated and leads to 6-inch devices with average total area efficiency above 15%.

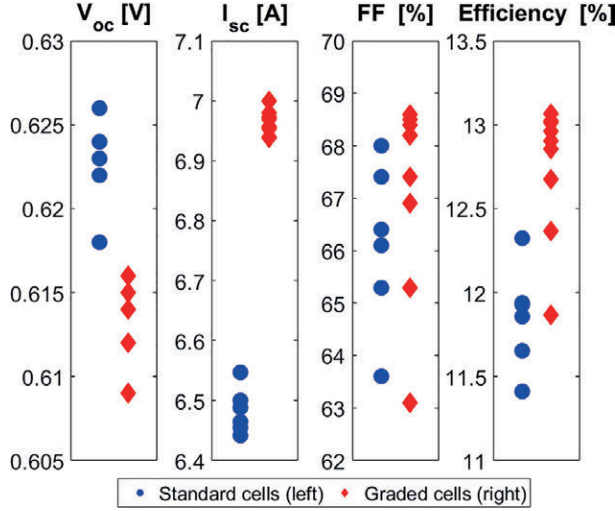


Figure 8.8. Solar cell parameters of 6-inch devices with standard and additionally graded absorber layers.

It is generally accepted that a steep back Ga-grading is beneficial for device performance as it alleviates recombination at the back contact interface leading to an increase in V_{OC} and device performance [167, 62]. This mechanism is particularly beneficial in thin devices [168, 58]. An extension of the back grading with a reduced slope into the absorber layer has also been shown to improve current collection and device performance [57]. The resulting gradient in the conduction band edge throughout the absorber bulk drives the electrons generated deep into the absorber towards the space charge region where they can be collected. This improvement is more prominent in absorbers where the minority carrier diffusion length L_n is relatively short. When L_n is in the order of or larger than the absorber thickness, the charge carriers can diffuse to the junction anyway and the carrier collection improvement due to bulk grading is negligible [61, 169]. For the industrial devices studied in this thesis where L_n is in the order of 600 nm, additional bulk grading is revealed to be beneficial for device performance in agreement with previous considerations.

8.3 Uniformity of 6-inch chalcogenide solar cells (Paper IV and V)

Uniformity of large area devices is the focus of the last part of this work. While relatively minor non-uniformity is observed in CIGS solar cells, large lateral performance discrepancies due to annealing are observed for CZTS devices.

8.3.1 Laterally-resolved characterization and simulation of CIGS absorbers and full solar cells

The record performance of CIGS and thin film solar cells in general is most of the time reported on 0.5 or 1 cm². While these record devices are important to show the potential of the technology, it also appears necessary to demonstrate high performance level on larger prototypes, closer to commercial products.

The uniformity of 6-inch CIGS solar cells is first studied at the material level where mapping of the absorber composition is performed in order to identify potential lateral discrepancies in group III and chalcogen element distribution. The absorber composition is found to be generally uniform within the accuracy of EDX measurements as depicted in Figure 8.9 .

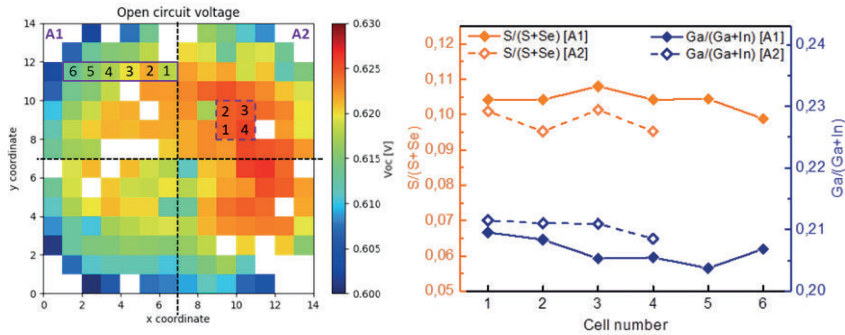


Figure 8.9. Left: Location of the small cells chosen for EDX mapping presented on a V_{OC} map. Right: Chalcogen and GGI ratios measured in EDX on the corresponding locations.

At the complete solar cell level, the 6-inch device is divided into 184, 1 cm² cells that are individually characterized with dark and illuminated JV and EQE measurements. The bandgap values extracted from EQE show minor variations over the 6-inch device, in agreement with a uniform absorber composition. Lateral variations in solar cell parameters are observed. Short circuit current values calculated from EQE show a decrease in photocurrent in the central part of the device. A decay of the EQE signal in the long wavelength range is observed in this area, consistent with increased recombination in the

bulk of the device or at the back-contact interface. Variations in the measured open-circuit voltage of the devices are also observed however, no direct link with material properties can be established. Potential origin for the observed discrepancies are discussed in Paper V and could be related to temperature variation induced by the extended measurement time and light-soaking effects combined with irradiance non-uniformity inherent to large area, ABB class solar simulators such as the one used in this study.

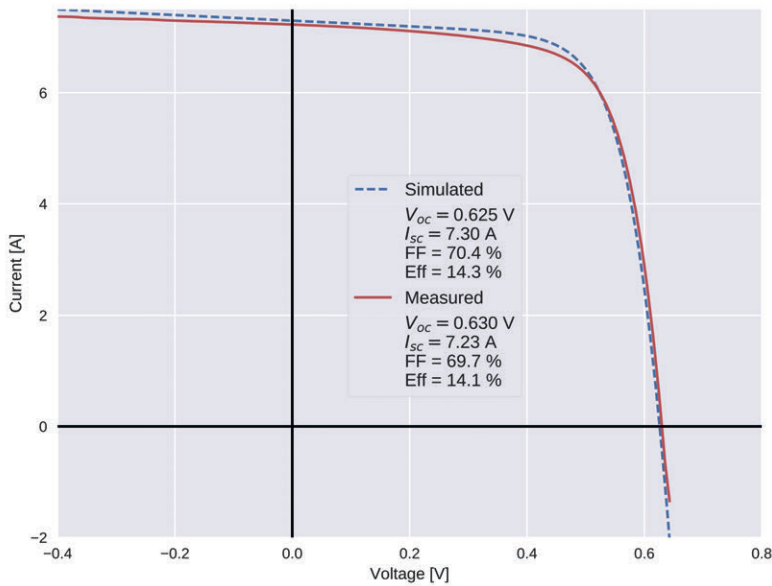


Figure 8.10. Comparison between IV curve simulated using the network model and the average of IV curves measured on 16 full size cells.

A SPICE network model is built in order to relate the performance of individual small cells to the performance of the 6-inch device. The simulated IV curves are compared with experimental IV measurements and relatively good agreement is observed as shown in Figure 8.10. This network model can be used as a basis for different types of studies including investigation of the impact of lateral variation in local solar cell parameters on full size device performance or front contact optimization.

8.3.2 Sputtering and annealing process uniformity for 6-inch CZTS device fabrication

Contrary to CIGS, the fabrication process of CZTS solar cells relies on a two-step approach based on room temperature sputtering followed by high temperature annealing. Microstructure and composition mapping of CZTS absorber over the 6-inch substrate is performed in “Uniformity assessment of a 6-inch copper-zinc-tin-sulfide solar cell sputtered from a quaternary target” (Paper IV).

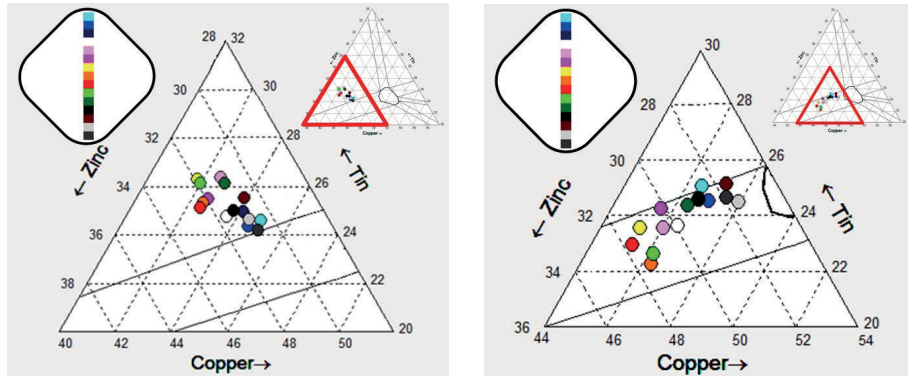


Figure 8.11. EDX composition measurement of CZTS precursors (left) and annealed absorber (right). The dot color in the ternary phase diagram corresponds to the location where the measurement was performed (see substrate schematic in the top left corner).

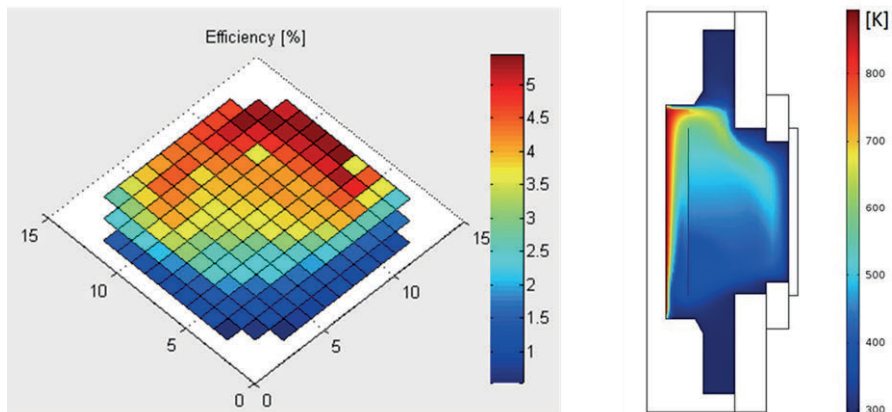


Figure 8.12. Left: Distribution of solar cell efficiency over the 6-inch substrate. Right: COMSOL simulation of the temperature distribution in the annealing chamber viewed in cross-section.

Figure 8.11 shows the composition of CZTS precursors along the diagonal of the substrate measured with EDX. It can be observed that the film composition is close to the composition of the target after sputtering. Moreover, the spread is limited. During annealing, however, the composition drifts substantially and a large scatter of relative Cu-Zn-Sn content along the substrate diagonal is revealed. The largest differences are seen for the Zn content. A potential explanation for such phenomenon is local ZnS segregation due to the Zn-rich composition of the precursors.

After complete cell processing, the special grid pattern including 184 small cells is screen printed and 1 cm^2 devices are manually scribed. JV curves are measured for each small cell and a performance map as shown in Figure 8.12 is drawn. Large differences in the distribution of solar cell parameters across the 6-inch device are identified. The root cause for non-uniformity is found to be inhomogeneous heat distribution in the annealing chamber, for which simulation results are shown in Figure 8.12, potentially coupled to lateral discrepancies in local sulfur partial pressure. The main consequences are uneven recrystallization of the absorber and lateral compositional variation which leads to areas exhibiting poor optoelectronic properties. Strong variations of solar cell parameters over the 6-inch device are hence observed which could be tempered by an improved design of the annealing chamber.

The best 1 cm^2 CZTS solar cell in this study shows an efficiency value of 5.1%.

9. Concluding remarks

CIGS and CZTS thin film solar cells are fabricated using an in-line vacuum, sputtering-based process. In both cases, the core investigation is focused on improving the absorber layer optoelectronic properties.

Kesterite layers are formed in a two-step process where CZTS precursors are first sputtered from a quaternary compound target and subsequently annealed in sulfur-containing atmosphere. It is found that increasing the annealing temperature from 420 °C to 550 °C has a positive effect on the material grain size. A beneficial impact on the corresponding device performance is also noticed with increasing annealing temperature up to 510 °C, consistent with the formation of larger kesterite grains. However, a dramatic drop in solar cell performance for annealing performed at 525 °C and 550 °C is also observed despite further crystallinity improvement.

An optical microscope inspection of the absorbers sulfurized at high temperature reveals a large number of blisters forming in the material during annealing. For samples crystallized at 520 °C and 550 °C, the highest temperature in this study, the majority of blisters rupture, locally exposing the Mo layer during further processing steps. Blister formation is found to originate from sputtering gas entrapment during precursor deposition. Limiting the amount of trapped gas during sputtering results in blister formation alleviation and corresponding solar cell performance improvement, up to power conversion efficiency of 5.1%.

Industrial CIGS solar cell absorbers are also studied through an analysis of the effect of bandgap grading on the resulting device performance. Simulations of devices exhibiting a thin absorber together with a relatively modest minority carrier diffusion length as a result of fast industrial processing show that a combination of steep back grading and gradual bandgap reduction extending throughout the bulk of the material is beneficial for solar cell performance. These results are consistent with experimental results where total area device efficiency values above 15 % for 6-inch solar cells are reported.

The uniformity of 6-inch CIGS and CZTS solar cells is also assessed. For CZTS devices, the uniformity is limited by the annealing process where an uneven temperature and gas distribution leads to variation in crystallization and composition over the device area. Technological solutions to uniformity issues are presented.

The CIGS solar cells are characterized by a much more homogeneous absorber layer. Some lateral variation mainly in short circuit current are observed and EQE measurements reveal slightly enhanced bulk or back interface recombination in the central part of the device. A SPICE network model is built to relate local solar cell performance to the properties of the full size 6-inch device. This model can be used as a basis for further uniformity-related studies.

10. Future work

Based on the results obtained in this thesis, several aspects of CIGS and CZTS solar cell processing are identified as topics of interest that require further investigations.

Deeper analysis of bandgap grading in absorbers sputtered from a set of compound targets with different GGI ratios is the natural continuation of the CIGS-related work in this thesis. S-grading combined with Ga-grading also seems to be an interesting route to follow.

CIGS layer thickness plays an important part in a cost-related perspective. Thinning down the absorber layer while maintaining high performance is one of the major stakes in the CIGS field. Achieving this goal is challenging as it involves specific strategies for improved light absorption as well as optimized bandgap grading and device architecture.

As pointed out in Paper III, the SCAPS model developed in this thesis does not completely grasp the behavior of thin absorbers. A deeper analysis of the differences in physical properties between thin and standard absorbers constitutes a basis towards understanding the discrepancies at the device level.

Paper V emphasizes the requirements on solar simulator irradiance lateral uniformity when relatively large and uniform devices are characterized locally. In this case, great care is required in order to guarantee long lasting, standard test conditions over extended areas in order to discriminate between trends resulting from material and device properties and those potentially coming from drifts in the setup.

CIGS sputtering from compound targets followed by annealing has been explored to some extent in literature mainly in terms of resulting absorber properties. One step sputtering at high temperature has not been studied much on the other hand and the mechanisms governing grain growth in such process are mainly unexplored. A detailed understanding of grain growth process as well as a study of the impact of sputtering parameters on the absorber microstructure and morphology appears to be necessary in order to optimize the CIGS deposition process.

Related to the CZTS process, a clear pathway towards improved uniformity of the device involves a re-design of the annealing chamber. One of the main issues in the current configuration of the annealing chamber is that the substrate is standing vertical leading to convection-related temperature differences over

the substrate. A possible work-around is to implement substrate rotation during annealing. A more long-term solution is to tilt the sample to horizontal position.

Several potential improvement paths for the deposition process are also identified. In quaternary compound sputtering, the composition of the deposited film is somewhat bound to the target composition. Optimization of the CZTS target composition and varying deposition parameters (substrate temperature for instance) could be an interesting lead to follow. An analysis of the stress in the precursors as a function of deposition parameters could also be insightful.

Regarding the annealing sequence, investigations of more advanced temperature profiles to limit secondary phase formation, obtain an ordered kesterite phase and finely tune the absorber optoelectronic properties would also be beneficial.

Sammanfattning på svenska

Den industriella revolutionen och de tekniska framsteg som följt har gett den moderna människan möjlighet till en hög levnadsstandard som vi utnyttjar dagligen. En viktig konsekvens av denna generella höjning av livskvalité är en ökad konsumtion av energi. Dagens samhällen i utvecklade och utvecklingsländer karakteriseras av en energimix till stor del baserad på fossila bränslen som kol, olja och naturgas. Dessa ämnen har väldigt hög energidensitet eftersom de är resultatet av långsamma kemiska reaktioner under extrema temperatur- och tryckförhållanden, flera hundra meter under jordytan. Denna enorma och relativt tillgängliga energikälla har exploaterats kraftigt av människan utan att tidigare på allvar bekymra sig om effekter på klimatet och hälsan hos jordens innevånare. Fossila bränslen används till största del genom förbränning, vilket medför betydande mängder koldioxid, med visad negativ effekt på klimatet, samt små partiklar av olika sammansättning med negativ inverkan på hälsan. Dessutom är de fossila bränslena begränsade i mängd och människan kan inte vara beroende av icke förnybara källor för all framtid.

Sedan några decennier finns flera innovativa lösningar för att på ett hållbart sätt extrahera energi från förnybara källor som finns i vår naturliga miljö. Människan kan idag utnyttja den potentiella energin i vattendammar, den kinetiska energin i vinden genom vindkraftverk och omvandla den elektromagnetiska energin från solen till värme eller elektricitet genom att använda till exempel termiska solfångare eller solcellsmoduler. Dessa tekniker är nu under full utveckling och överenskommelserna om klimatet i Parisavtalet 2015 ger en strimma hopp genom att världen massivt engagerar sig för en total omställning av energisystemet.

Den strålade energi som når jorden från solen under ett enda dygn räcker för att täcka mänsklighetens behov under ett år. Att effektivt kunna omvandla denna solenergi är förstås en viktig del av energiomställningen. Den fotovoltaiska effekten, upptäckt av Edmond Becquerel 1839, är den direkta generationen av elektrisk energi från ljus. Dagens fotovoltaiska tekniker baseras på material som kallas halvledare som har speciella optoelektriska egenskaper som möjliggör generation av elektron-hålpar genom excitation av ljus. Det vanligaste halvledarmaterialet i solcellsindustrin är kisel. Det är en mogen och välutvecklad teknologi som dragit nytta av 50 års forskning och utveckling inom mikroelektroniken.

Verkningsgraden hos en solcell är per definition den andel av den instrålade energin som omvandlas till elektrisk energi. För kisel-solceller ligger rekordet

i verkningsgrad över 25 % och för moduler på marknaden ligger verkningsgraden mellan 15 och 20 %. Celler och moduler baserade på tunnfilmsmaterial är i dagsläget mindre använda eftersom verkningsgraden generellt är lägre. Dock har flera forskargrupper och företag nyligen visat att verkningsgrader över 20 % är möjligt baserat på materialen koppar-indium-selen (CIGS) och kadmiumtellurid (CdTe). Dessa höga värden är visade på cellnivå medan modulverkningsgrader ligger mellan 13-16 %.

Tunnfilmsteknikerna, och särskilt CIGS, tillåter också olika applikationer vilket tillåter en diversifiering av användningsområdena för solceller. Materialet CZTS (koppar, zink, tenn, svavel) har liknande möjligheter med den ytterligare fördelen att det baseras helt på grundämnen som är väldigt vanligt förekommande i jordskorpan. CZTS skulle kunna spela en framträdande roll i framtidens solcellsindustri då de optoelektriska egenskaperna liknar CIGS. Dock är verkningsgraden för solceller baserade på CZTS mycket lägre än för CIGS; 12,6 % vilket ger stor potential för förbättring. Den här avhandlingen har realiserats i ett samarbete mellan Uppsala universitet och Midsummer AB, med syftet att studera och förbättra optoelektroniska egenskaper hos solceller baserade på CIGS och CZTS, deponerade på rostfritt stål.

Till att börja med har materialet CZTS analyserats i detalj i en studie om inverkan från temperatur i värmebehandlingssteget. Kornstorleken hos CZTS ökade med temperaturen, men över 510 °C sjönk istället verkningsgraden. Orsaken till detta visade sig vara formation av mikrokaviteter vid bakkontakten under värmebehandlingen. Bildandet av mikrokaviteter visade sig vara kopplad till ackumulering av argon vid sputtring. Byte av sputtergas till tyngre atomer som Krypton, eller höjd temperatur eller tryck vid sputtring gav reducerad densitet av mikrokaviteter. Den högsta verkningsgrad som uppnåts är runt 5 %.

Konceptet med bandgapsgradering studerades för materialet CIGS. Den industriella process som använts, magnetronsputtring från sammansatt target vid hög temperatur, sätter begränsningar på kvalitén och tjockleken hos det aktiva lagret. Diffusionslängden hos minoritetsladdningsbärarna är relativt kort och tjockleken hos CIGS-skiktet under en mikrometer. En studie baserad på simuleringar av solceller i mjukvaran SCAPS genomfördes med uppmätt sammansättningsprofil som bas. Simuleringarna validerades mot verkliga solceller och en optimal sammansättningsprofil simulerades. Resultatet visade en ökad verkningsgrad för en optimal profil, vilket också kunde visas experimentellt med verkningsgrader nära 15 % för en 6-tumssolcell.

Slutligen har uniformiteten hos 6-tumssolceller analyserats och simulerats. För CZTS är det begränsande steget högttemperaturbehandlingen och en modifiering av kammaren nödvändig för att få homogena solceller. Uniformiteten för CIGS är mycket bättre även om förbättringar kan göras i deponeringen av

det aktiva lagret för att höja öppenkretsspänningen och minska förluster kopplade till filmernas ytterkanter.

Résumé en français

La révolution industrielle et les progrès technologiques qui en ont découlé ont permis à l'homme moderne d'accéder à un haut niveau de confort dont nous profitons au quotidien. Une conséquence importante de cette amélioration générale de la qualité de vie est une consommation accrue d'énergie. Les sociétés contemporaines des pays développés ou en voie de développement sont caractérisées par un mix énergétique largement basé sur l'utilisation de carburants fossiles tels que le charbon, le pétrole ou le gaz naturel. Ces substances ont la particularité d'être extraordinairement denses en énergie car elles résultent de réactions chimiques lentes ayant eu lieu dans des conditions de pression et température extrêmes, à plusieurs centaines de mètres sous terre. Cette énorme et relativement accessible source d'énergie a été profondément exploitée par l'Homme sans vraiment se soucier des répercussions sur le climat global et la santé de tous les habitants de la Terre. En effet, l'énergie des carburants fossiles est le plus souvent extraite par combustion, qui dégage des quantités importantes de dioxyde de carbone, dont l'impact négatif sur le climat est largement prouvé, de particules fines et de multiples composés potentiellement nocifs pour les êtres vivants. De plus, et comme leur nom l'indique, les carburants fossiles sont limités en quantité et l'Homme ne peut dépendre de ressources non-renouvelables s'il veut assurer la pérennité de sa descendance.

Depuis maintenant plusieurs dizaines d'années, de multiples solutions innovantes ont été mises au point pour extraire de manière durable l'énergie issue de sources renouvelables, disponible dans notre milieu naturel. Ainsi l'Homme est de nos jours capable de récupérer l'énergie potentielle de l'eau en altitude grâce aux barrages hydroélectriques, de capter l'énergie cinétique du vent en utilisant des champs d'éoliennes et de transformer l'énergie électromagnétique émise par le soleil en chaleur ou électricité en utilisant des panneaux solaires thermiques ou photovoltaïques, parmi bien d'autres exemples. Ces technologies sont actuellement en plein essor et les accords de Paris sur le climat de 2015 constituent un élément d'espoir majeur de voir le monde s'engager massivement et durablement dans une transition profonde du modèle énergétique.

L'énergie lumineuse reçue par la Terre en provenance du soleil durant une seule journée est suffisante pour couvrir les besoins de l'Humanité pendant une année. Il va donc sans dire que récupérer l'énergie du soleil de manière efficace est un enjeu majeur de la transition énergétique. L'effet photovoltaïque, découvert par Edmond Becquerel en 1839, est la génération directe d'électricité

à partir de lumière. Les technologies photovoltaïques actuelles sont basées sur des matériaux dits semi-conducteurs qui présentent des propriétés opto-électroniques particulières leur permettant la génération de paires électrons-trous lorsqu'ils sont sujets à une excitation externe telle que la lumière. Le matériau semi-conducteur le plus utilisé dans l'industrie photovoltaïque est le silicium. Il s'agit d'une technologie mature et efficace qui bénéficie de multiples améliorations apportées durant plus de cinquante ans de recherche en micro-électronique.

L'efficacité d'une cellule solaire est définie par son rendement ou la proportion de l'énergie solaire incidente qui est convertie en électricité. Les records de rendement pour les cellules silicium utilisant des technologies et procédés avancés sont au-delà de 25%. Le rendement des panneaux en silicium modernes se situe entre 15 et plus de 20% suivant le type de silicium (multi ou monocristallin) et la technologie employée.

Les cellules et panneaux photovoltaïques basés sur des couches minces sont moins répandus à l'heure actuelle car leur rendement solaire est généralement plus faible. Toutefois, plusieurs groupes de recherche et entreprises ont récemment démontré qu'il était possible d'atteindre des valeurs bien supérieures à 20 % en utilisant les technologies sélénium de cuivre-indium-gallium (CIGS) ou encore tellure de cadmium (CdTe). Il est néanmoins nécessaire de préciser que ces valeurs sont obtenues en laboratoires pour des cellules solaires de petite taille (1 cm² ou moins). Pour des panneaux solaires de taille commerciale les rendements sont de l'ordre de 13 à 16%.

Les technologies en couches minces présentent certains avantages qui les rendent particulièrement pertinentes pour plusieurs types d'applications. Tout d'abord, le coefficient d'absorption des semi-conducteurs utilisés est plus élevé que pour le silicium. Une très fine couche de matériau actif, de l'ordre de quelques micromètres d'épaisseur (comparé à plusieurs dizaines voire centaines de micromètres pour les technologies silicium) est donc suffisante pour absorber la quasi-intégralité du rayonnement solaire. La fabrication d'une cellule requiert donc une très faible quantité de matériau. Des techniques de dépôt en couches minces matures telles que l'évaporation ou la pulvérisation magnétron sont le plus souvent utilisées lors de la fabrication.

Le substrat le plus commun est une plaque de verre sodocalcique mais la structure en couches minces permet une grande flexibilité et les cellules peuvent être fabriquées sur polymère ou encore sur feuille d'acier. Les panneaux solaires sont alors beaucoup plus légers que les panneaux conventionnels, et potentiellement flexibles, ce qui permet de les installer sur tous types de toitures, qu'elles soient industrielles ou résidentielles, plates ou incurvées.

Par ailleurs, l'utilisation de substrat léger et flexible facilite la combinaison de plusieurs fonctions différentes au sein d'un même produit. Cette idée est au cœur des concepts de BIPV, "building-integrated photovoltaics", et PIPV, "product-integrated photovoltaics", en anglais. Dans le cas du BIPV, un

matériau de construction, typiquement un élément de couverture, intègre des cellules solaires pour produire de l'électricité en plus de sa fonction première liée à la protection et à l'étanchéité du bâtiment. Le PIPV élargit ce concept aux véhicules, membranes diverses ainsi qu'à différents objets du quotidien. La production d'électricité intervient alors au plus près de son lieu de consommation, en complète adéquation avec la nature éparse du rayonnement solaire.

Les technologies en couches minces et principalement le CIGS offrent donc une palette d'applications variées, permettant de diversifier les domaines d'application du photovoltaïque. Le matériau CZTS (sulfure/sélénure de cuivre-zinc-étain) offre des perspectives similaires avec l'avantage supplémentaire d'être basé exclusivement sur des éléments parmi les plus abondants dans la croûte terrestre. Proche du CIGS en terme de propriétés physiques et opto-électroniques, le CZTS pourrait jouer un rôle de premier ordre dans le photovoltaïque du futur. Les records de rendement solaire pour les cellules basées sur le CZTS sont inférieurs à ceux des cellules en CIGS, de l'ordre de 12%, ce qui témoigne d'un large potentiel d'amélioration.

Cette thèse, réalisée dans le cadre d'un partenariat industriel entre l'université d'Uppsala et Midsummer AB, vise à améliorer les propriétés opto-électroniques de couches actives pour cellules solaires CIGS et CZTS, déposées sur substrats en acier inoxydable. Le procédé de fabrication, réalisé en ligne, sous vide, est exclusivement basé sur la pulvérisation magnétron.

Dans un premier temps, le matériau CZTS est analysé en détail à travers une étude de l'impact de la température lors de l'étape de recuit. Le diamètre des grains de CZTS augmente avec la température de recuit, cependant, au-delà de 510°C, les performances des cellules solaires correspondantes déclinent fortement. L'origine de ce phénomène est la formation de micro-cavités en face arrière de la couche active durant le recuit. La formation de ces micro-cavités est elle-même liée à la capture d'ions argon, utilisés durant la pulvérisation, au sein de la couche en croissance. Une légère élévation de la température du substrat ou de la pression de dépôt permet de réduire drastiquement la quantité de gaz piégé dans le film et d'éviter la formation de micro-cavités. Le rendement solaire maximum obtenu est de l'ordre de 5%.

Le concept de gradient de bande interdite est ensuite exploré pour le matériau CIGS. Le procédé industriel utilisé, basé sur la pulvérisation magnétron de cibles quaternaires à haute température, induit certaines limitations en termes de propriétés physiques et opto-électroniques des couches minces de CIGS comparé aux échantillons normalement étudiés en recherche. En effet, la longueur de diffusion des porteurs de charge minoritaires est limitée et l'épaisseur de la couche active ne dépasse pas un micromètre. Une étude basée sur des simulations SCAPS des cellules solaires est réalisée dans un premier temps pour identifier le profil de bande interdite le plus prometteur. Des échantillons correspondants sont ensuite fabriqués et caractérisés. Les résultats d'analyse

sont alors comparés avec les simulations et un gain de performance est observé dans les deux cas. Le procédé développé est ensuite transféré en production où le rendement solaire de cellules de six pouces avoisine 15 %.

Finalement, l'uniformité de cellules solaires de six pouces de côté est analysée. Pour la technologie CZTS, l'étape à haute température est l'élément limitant et une modification de la chambre de recuit est nécessaire pour l'obtention de cellules homogènes. L'uniformité du procédé CIGS est généralement bien meilleure même si certaines améliorations peuvent être apportées au procédé de dépôt de la couche active pour maximiser le courant de court-circuit et le rendement solaire des cellules.

Acknowledgements

This work was supported by the Swedish Energy Agency, the Swedish Foundation for Strategic Research as well as Midsummer AB. These organizations are presently acknowledged.

Lotten, I would like to first thank you for believing in me and giving me this wonderful opportunity. I will always be grateful to you for all you have taught me and for being such a knowledgeable, conscientious and considerate supervisor.

Jan, you have been a great supervisor at Midsummer for two years. I want to thank you for supporting me everyday during the first two years of my PhD, for your open-mindedness, your kindness and numerous insightful discussions on solar cells, green technologies and a lot of other things. I think I will always remember the Swedish word "raggmunk" that made so many people turn around in the commuter train in Paris.

Eric, I would also like to thank you for supervising me at Midsummer and for being such a competent manager. The stakes at the university and in a company are not always the same but I am thankful to you for giving me the possibility to work on all aspects related to the PhD. I will probably never run as fast as you do but I will try to continue being as driven as you are.

Sven, I cannot thank you enough for your help with accommodation during the first months of my PhD (many thanks to Lisa too), among many other things. Midsummer is great company and I really hope that it will continue to thrive.

Christopher and Ray, I have not been in Uppsala very consistently but you did not hesitate to help me with accommodation and I am very grateful for that. You are two very talented young researchers as well as great individuals and I wish you the best.

Tove and Liv, I would like to thank you for starting the work on CZTS at Midsummer and provide me with a basis to build my work upon.

Leo, you have spent a lot of your time at Midsummer on EDX measurements and I know that it has sometimes been tedious. Thank you for your help and for the nice results on CZTS uniformity.

Ingrid, I am sorry that we could not continue your project a bit further, but I want you to know that the results you obtained are relevant and that they will be used for further improvement of Midsummer's CIGS solar cells. Many thanks for your hard work and your contagious "joie de vivre".

Jonathan, I would like to thank you for your help with Raman measurements and for being such a nice teacher on CZTS solar cells.

Bart, I have not directly worked with you in the framework on this PhD but I am sure it would have been great. Thank you for bringing new interesting concepts to the field of CIGS.

Alexandra, you have helped me a lot with compositional measurements and I am really grateful to you. Thank you for your flexibility, reactivity, and sympathy.

I would like to warmly acknowledge the process and R&D team at Midsummer for help with sample preparation, very professional work and entertaining discussions. Esko, Johan, Klara, Peter, Rodrigo, Adam, Torbjörn, Mattias, Olle, Patrik, Cecilia, MERCI BEAUCOUP!

Cecilia, I would like to thank you for your communicative happiness and for always taking time to help me fix the SMO and keep the "old beast" up and running.

Alf, I am still trying to find a broken device that you cannot fix... but I think I will be looking for a long time. Thanks for your help with a lot of hardware-related issues.

I am grateful to Volodymyr and Adam for interesting discussions on electrical measurements and perovskite solar cells.

I want to acknowledge everybody from the CZTS and CIGS group in Uppsala as well as Pr. Zhang for allowing this project to be conducted.

Olivier, Lucie, thanks a lot for the very nice time we have spent together, great week-end lunch invitations, gardening-related discussions and many other things!

Flore, Vincent, Victor, Goedeke, Kaspar, Fransisco, Per and others, you have been great friends during this PhD and I know it will continue. Thank you for your support and very nice times both in Sweden and in France!

I would like to thank my friends from France for visiting me (Maxime, Nicolas, Sébastien, Stéphanie, Loïc, Florent, Julien, Pauline) or just supporting me telepathically.

Finally, I would like to express my deepest gratitude to my family, Mom, Dad, Christelle, Florent, for unconditionally supporting my choice to go to Sweden, and I know it has not always been easy, and for visiting me as often as possible. The last words go to my sweetheart, Pauline, thank you for joining me in Sweden and for making my life beautiful everyday.

References

- [1] Core writing team, R. K. Pachauri, and L. Meyer, “Climate change 2014: Synthesis report. contribution of working groups I, II and III to the fifth assessment report of the intergovernmental panel on climate change,” tech. rep., IPCC, 2014. http://www.ipcc.ch/pdf/assessment-report/ar5/syr/SYR_AR5_FINAL_full_wcover.pdf.
- [2] E. G. Hertwich, J. A. de Lardereel, A. Arvesen, P. Bayer, J. Bergeson, E. Bouman, T. Gibon, G. Heath, C. Peña, P. Purohit, A. Ramirez, and S. Suh, “Green energy choices: The benefits, risks and trade-offs of low-carbon technologies for electricity production,” tech. rep., UNEP. International resource panel, 2016. Available for download at: <http://www.resourcepanel.org/reports/green-energy-choices-benefits-risks-and-trade-offs-low-carbon-technologies-electricity>.
- [3] UNFCCC, “Paris agreement,” 2015. http://unfccc.int/files/essential_background/convention/application/pdf/english_paris_agreement.pdf.
- [4] D. Gielen, R. Kempener, M. Taylor, F. Boshell, and A. Seleem, “Letting in the light: How solar photovoltaics will revolutionise the electricity system,” tech. rep., IRENA, 2016. http://www.irena.org/DocumentDownloads/Publications/IRENA_Letting_in_the_Light_2016.pdf.
- [5] R. Ferroukhi, J. Sawin, F. Sverisson, H. Wuester, G. Kieffer, D. Nagpal, D. Hawila, A. Khalid, D. Saygin, and S. Vinci, “Rethinking energy 2017: Accelerating the global energy transformation,” tech. rep., IRENA, 2017. http://www.irena.org/DocumentDownloads/Publications/IRENA_REthinking_Energy_2017.pdf.
- [6] M. Wild, D. Folini, C. Schär, N. Loeb, E. G. Dutton, and G. König-Langlo, “The global energy balance from a surface perspective,” *Climate Dynamics*, vol. 40, no. 11, pp. 3107–3134, 2013.
- [7] “©OECD/IEA 2016 Key world energy statistics.” IEA publishing, 2016. Licence: www.iea.org/t&c.
- [8] E. Becquerel, “Mémoire sur les effets électriques produits sous l’influence des rayons solaires,” *Comptes rendus hebdomadaires des séances de l’Académie des Sciences*, vol. 9, pp. 561–567, 1839.
- [9] D. M. Chapin, C. S. Fuller, and G. L. Pearson, “A new silicon p-n junction photocell for converting solar radiation into electrical power,” *Journal of Applied Physics*, vol. 25, no. 5, pp. 676–677, 1954.
- [10] M. Taylor, P. Ralon, and A. Ilasi, “The power to change: Solar and wind cost reduction potential to 2025,” tech. rep., IRENA, 2016. http://www.irena.org/DocumentDownloads/Publications/IRENA_Power_to_Change_2016.pdf.

- [11] K. Yoshikawa, H. Kawasaki, W. Yoshida, T. Irie, K. Konishi, K. Nakano, T. Uto, D. Adachi, M. Kanematsu, H. Uzu, and K. Yamamoto, "Silicon heterojunction solar cell with interdigitated back contacts for a photoconversion efficiency over 26%," *Nature Energy*, vol. 2, p. 17032, mar 2017.
- [12] M. A. Green, Y. Hishikawa, W. Warta, E. D. Dunlop, D. H. Levi, J. Hohl-Ebinger, and A. W. Ho-Baillie, "Solar cell efficiency tables (version 50)," *Progress in Photovoltaics: Research and Applications*, vol. 25, no. 7, pp. 668–676, 2017. PIP-17-089.
- [13] "CIGS White Paper Initiative."
<http://cigs-pv.net/cigs-white-paper-initiative/>.
Accessed: 2017-07-06.
- [14] "First Solar website." <http://www.firstsolar.com/>. Accessed: 2017-07-06.
- [15] W. Wang, M. T. Winkler, O. Gunawan, T. Gokmen, T. K. Todorov, Y. Zhu, and D. B. Mitzi, "Device characteristics of CZTSSe thin-film solar cells with 12.6% efficiency," *Advanced Energy Materials*, vol. 4, no. 7, p. 1301465, 2014.
- [16] D. Abou-Ras, S. Wagner, B. J. Stanbery, H.-W. Schock, R. Scheer, L. Stolt, S. Siebentritt, D. Lincot, C. Eberspacher, K. Kushiya, and A. N. Tiwari, "Innovation highway: Breakthrough milestones and key developments in chalcopyrite photovoltaics from a retrospective viewpoint," *Thin Solid Films*, vol. 633, pp. 2 – 12, 2017. E-MRS 2016 Spring Meeting, Symposium V, Thin-Film Chalcogenide Photovoltaic Materials.
- [17] P. Jackson, R. Wuerz, D. Hariskos, E. Lotter, W. Witte, and M. Powalla, "Effects of heavy alkali elements in Cu(In,Ga)Se₂ solar cells with efficiencies up to 22.6%," *physica status solidi (RRL) – Rapid Research Letters*, vol. 10, no. 8, pp. 583–586, 2016.
- [18] T. J. Huang, X. Yin, G. Qi, and H. Gong, "CZTS-based materials and interfaces and their effects on the performance of thin film solar cells," *physica status solidi (RRL) – Rapid Research Letters*, vol. 08, no. 09, pp. 735–762, 2014.
- [19] W. Peter, W. Uli, et al., *Physics of solar cells: from basic principles to advanced concepts*. John Wiley & Sons, 2016.
- [20] A. H. Smets, K. Jäger, O. Isabella, R. A. van Swaaij, and M. Zeman, *Solar Energy: The physics and engineering of photovoltaic conversion, technologies and systems*. UIT Cambridge Limited, 2016.
- [21] W. Shockley and H. J. Queisser, "Detailed balance limit of efficiency of pn junction solar cells," *Journal of Applied Physics*, vol. 32, no. 3, pp. 510–519, 1961.
- [22] "ASTM G173-03, Reference solar spectral irradiance AM1.5." downloaded from <http://rredc.nrel.gov/solar/spectra/am1.5/>.
Accessed: 2017-08-19.
- [23] U. Rau and M. Schmidt, "Electronic properties of ZnO/CdS/Cu(In,Ga)Se₂ solar cells — aspects of heterojunction formation," *Thin Solid Films*, vol. 387, no. 1, pp. 141 – 146, 2001. Proceedings of Symposium N on Thin Film Photovoltaic materials of the E-MRS Spring Conference.
- [24] N. Naghavi, S. Spiering, M. Powalla, B. Cavana, and D. Lincot,

- “High-efficiency copper indium gallium diselenide (CIGS) solar cells with indium sulfide buffer layers deposited by atomic layer chemical vapor deposition (ALCVD),” *Progress in Photovoltaics: Research and Applications*, vol. 11, no. 7, pp. 437–443, 2003.
- [25] M. Bär, B.-A. Schubert, B. Marsen, R. G. Wilks, S. Pookpanratana, M. Blum, S. Krause, T. Unold, W. Yang, L. Weinhardt, C. Heske, and H.-W. Schock, “Cliff-like conduction band offset and KCN-induced recombination barrier enhancement at the CdS/Cu₂ZnSnS₄ thin-film solar cell heterojunction,” *Applied Physics Letters*, vol. 99, no. 22, p. 222105, 2011.
- [26] M. A. Contreras, M. J. Romero, B. To, F. Hasoon, R. Noufi, S. Ward, and K. Ramanathan, “Optimization of CBD CdS process in high-efficiency Cu(In,Ga)Se₂-based solar cells,” *Thin Solid Films*, vol. 403, pp. 204 – 211, 2002. Proceedings of Symposium P on Thin Film Materials for Photovoltaics.
- [27] T. Minemoto, T. Matsui, H. Takakura, Y. Hamakawa, T. Negami, Y. Hashimoto, T. Uenoyama, and M. Kitagawa, “Theoretical analysis of the effect of conduction band offset of window/CIS layers on performance of CIS solar cells using device simulation,” *Solar Energy Materials and Solar Cells*, vol. 67, no. 1, pp. 83 – 88, 2001. PVSEC 11 - PART III.
- [28] D. A. R. Barkhouse, R. Haight, N. Sakai, H. Hiroi, H. Sugimoto, and D. B. Mitzi, “Cd-free buffer layer materials on Cu₂ZnSn(S_xSe_{1-x})₄: Band alignments with ZnO, ZnS, and In₂S₃,” *Applied Physics Letters*, vol. 100, no. 19, p. 193904, 2012.
- [29] N. Naghavi, D. Abou-Ras, N. Allsop, N. Barreau, S. Bücheler, A. Ennaoui, C.-H. Fischer, C. Guillen, D. Hariskos, J. Herrero, R. Klenk, K. Kushiya, D. Lincot, R. Menner, T. Nakada, C. Platzer-Björkman, S. Spiering, A. Tiwari, and T. Törndahl, “Buffer layers and transparent conducting oxides for chalcopyrite Cu(In,Ga)(S,Se)₂ based thin film photovoltaics: present status and current developments,” *Progress in Photovoltaics: Research and Applications*, vol. 18, no. 6, pp. 411–433, 2010.
- [30] S. ichi Shimakawa, Y. Hashimoto, S. Hayashi, T. Satoh, and T. Negami, “Annealing effects on Zn_{1-x}Mg_xO/CIGS interfaces characterized by ultraviolet light excited time-resolved photoluminescence,” *Solar Energy Materials and Solar Cells*, vol. 92, no. 9, pp. 1086 – 1090, 2008.
- [31] R. Klenk, A. Steigert, T. Rissom, D. Greiner, C. A. Kaufmann, T. Unold, and M. C. Lux-Steiner, “Junction formation by Zn(O,S) sputtering yields CIGSe-based cells with efficiencies exceeding 18%,” *Progress in Photovoltaics: Research and Applications*, vol. 22, no. 2, pp. 161–165, 2014. PIP-13-088.R2.
- [32] D. Hariskos, S. Spiering, and M. Powalla, “Buffer layers in Cu(In,Ga)Se₂ solar cells and modules,” *Thin Solid Films*, vol. 480, pp. 99 – 109, 2005. EMRS 2004.
- [33] R. Scheer, L. Messmann-Vera, R. Klenk, and H.-W. Schock, “On the role of non-doped Zn O in CIGSe solar cells,” *Progress in Photovoltaics: Research and Applications*, vol. 20, no. 6, pp. 619–624, 2012.
- [34] G. Hanna, A. Jasenek, U. Rau, and H. Schock, “Influence of the Ga-content on the bulk defect densities of Cu(In,Ga)Se₂,” *Thin Solid Films*, vol. 387, no. 1, pp. 71 – 73, 2001. Proceedings of Symposium N on Thin Film

- Photovoltaic materials of the E-MRS Spring Conference.
- [35] K. Orgassa, *Coherent Optical Analysis of the ZnO/CdS/Cu(In,Ga)Se₂ Thin Film Solar Cell*. Berichte aus der Halbleitertechnik, Shaker, 2004.
 - [36] R. Herberholz, U. Rau, H. W. Schock, T. Haalboom, T. Gödecke, F. Ernst, C. Beilharz, K. W. Benz, and D. Cahen, "Phase segregation, Cu migration and junction formation in Cu(In, Ga)Se₂," *The European Physical Journal - Applied Physics*, vol. 6, no. 2, p. 131–139, 1999.
 - [37] S. B. Zhang, S.-H. Wei, A. Zunger, and H. Katayama-Yoshida, "Defect physics of the CuInSe₂ chalcopyrite semiconductor," *Phys. Rev. B*, vol. 57, pp. 9642–9656, Apr 1998.
 - [38] J. Pohl and K. Albe, "Intrinsic point defects in CuInSe₂ and CuGaSe₂ as seen via screened-exchange hybrid density functional theory," *Phys. Rev. B*, vol. 87, p. 245203, Jun 2013.
 - [39] C. Persson, Y.-J. Zhao, S. Lany, and A. Zunger, "n-type doping of CuInSe₂ and CuGaSe₂," *Phys. Rev. B*, vol. 72, p. 035211, Jul 2005.
 - [40] M. Igalson, P. Zabierowski, D. Prządo, A. Urbaniak, M. Edoff, and W. N. Shafarman, "Understanding defect-related issues limiting efficiency of CIGS solar cells," *Solar Energy Materials and Solar Cells*, vol. 93, no. 8, pp. 1290 – 1295, 2009.
 - [41] T. Walter, R. Herberholz, C. Müller, and H. W. Schock, "Determination of defect distributions from admittance measurements and application to Cu(In,Ga)Se₂ based heterojunctions," *Journal of Applied Physics*, vol. 80, no. 8, pp. 4411–4420, 1996.
 - [42] S. Siebentritt, "What limits the efficiency of chalcopyrite solar cells?," *Solar Energy Materials and Solar Cells*, vol. 95, no. 6, pp. 1471 – 1476, 2011. Special Issue : Thin film and nanostructured solar cells.
 - [43] M. A. Contreras, J. Tuttle, A. Gabor, A. Tennant, K. Ramanathan, S. Asher, A. Franz, J. Keane, L. Wang, J. Scofield, *et al.*, "High efficiency Cu(In,Ga)Se₂-based solar cells: processing of novel absorber structures," in *Photovoltaic Energy Conversion, 1994., Conference Record of the Twenty Fourth. IEEE Photovoltaic Specialists Conference-1994, 1994 IEEE First World Conference on*, vol. 1, pp. 68–75, IEEE, 1994.
 - [44] R. Kamada, T. Yagioka, S. Adachi, A. Handa, K. F. Tai, T. Kato, and H. Sugimoto, "New world record Cu(In,Ga)(Se, S)₂ thin film solar cell efficiency beyond 22%," in *2016 IEEE 43rd Photovoltaic Specialists Conference (PVSC)*, pp. 1287–1291, June 2016.
 - [45] C. J. Hibberd, E. Chassaing, W. Liu, D. B. Mitzi, D. Lincot, and A. N. Tiwari, "Non-vacuum methods for formation of Cu(In, Ga)(Se, S)₂ thin film photovoltaic absorbers," *Progress in Photovoltaics: Research and Applications*, vol. 18, no. 6, pp. 434–452, 2010.
 - [46] D. Lee and K. Yong, "Non-vacuum deposition of CIGS absorber films for low-cost thin film solar cells," *Korean Journal of Chemical Engineering*, vol. 30, pp. 1347–1358, Jul 2013.
 - [47] S. M. McLeod, C. J. Hages, N. J. Carter, and R. Agrawal, "Synthesis and characterization of 15% efficient CIGS solar cells from nanoparticle inks," *Progress in Photovoltaics: Research and Applications*, vol. 23, no. 11, pp. 1550–1556, 2015. PIP-14-060.R1.

- [48] C. Kind, C. Feldmann, A. Quintilla, and E. Ahlswede, "Citrate-capped $\text{Cu}_{11}\text{In}_9$ nanoparticles and its use for thin-film manufacturing of CIS solar cells," *Chemistry of Materials*, vol. 23, no. 23, pp. 5269–5274, 2011.
- [49] D.-Y. Lee, S. Park, and J. Kim, "Structural analysis of CIGS film prepared by chemical spray deposition," *Current Applied Physics*, vol. 11, no. 1, pp. S88 – S92, 2011. International Conference on Electronic Materials.
- [50] D. Lincot, J. Guillemoles, S. Taunier, D. Guimard, J. Sixx-Kurdi, A. Chaumont, O. Roussel, O. Ramdani, C. Hubert, J. Fauvarque, N. Bodereau, L. Parissi, P. Panheleux, P. Fanouillere, N. Naghavi, P. Grand, M. Benfarah, P. Mogensen, and O. Kerrec, "Chalcopyrite thin film solar cells by electrodeposition," *Solar Energy*, vol. 77, no. 6, pp. 725 – 737, 2004. Thin Film PV.
- [51] T. K. Todorov, O. Gunawan, T. Gokmen, and D. B. Mitzi, "Solution-processed $\text{Cu}(\text{In,Ga})(\text{S,Se})_2$ absorber yielding a 15.2% efficient solar cell," *Progress in Photovoltaics: Research and Applications*, vol. 21, no. 1, pp. 82–87, 2013.
- [52] T. Zhang, Y. Yang, D. Liu, S. C. Tse, W. Cao, Z. Feng, S. Chen, and L. Qian, "High efficiency solution-processed thin-film $\text{Cu}(\text{In,Ga})(\text{Se,S})_2$ solar cells," *Energy Environ. Sci.*, vol. 9, pp. 3674–3681, 2016.
- [53] T. Kato, "Cu(In,Ga)(Se,S)₂ solar cell research in Solar FRONTIER: Progress and current status," *Japanese Journal of Applied Physics*, vol. 56, no. 4S, p. 04CA02, 2017.
- [54] T. Feurer, P. Reinhard, E. Avancini, B. Bissig, J. Löckinger, P. Fuchs, R. Carron, T. P. Weiss, J. Perrenoud, S. Stutterheim, S. Buecheler, and A. N. Tiwari, "Progress in thin film CIGS photovoltaics – Research and development, manufacturing, and applications," *Progress in Photovoltaics: Research and Applications*, vol. 25, no. 7, pp. 645–667, 2017. PIP-16-131.R1.
- [55] R. Scheer and H.-W. Schock, *Chalcogenide photovoltaics: physics, technologies, and thin film devices*. John Wiley & Sons, 2011.
- [56] K. Ramanathan, M. A. Contreras, C. L. Perkins, S. Asher, F. S. Hasoon, J. Keane, D. Young, M. Romero, W. Metzger, R. Noufi, J. Ward, and A. Duda, "Properties of 19.2% efficiency $\text{ZnO/CdS/Cu}(\text{In,Ga})\text{Se}_2$ thin-film solar cells," *Progress in Photovoltaics: Research and Applications*, vol. 11, no. 4, pp. 225–230, 2003.
- [57] T. Dullweber, G. Hanna, W. Shams-Kolahi, A. Schwartzlander, M. Contreras, R. Noufi, and H. Schock, "Study of the effect of gallium grading in $\text{Cu}(\text{In,Ga})\text{Se}_2$," *Thin Solid Films*, vol. 361, pp. 478 – 481, 2000.
- [58] O. Lundberg, M. Bodegård, J. Malmström, and L. Stolt, "Influence of the $\text{Cu}(\text{In,Ga})\text{Se}_2$ thickness and ga grading on solar cell performance," *Progress in Photovoltaics: Research and Applications*, vol. 11, no. 2, pp. 77–88, 2003.
- [59] W. Witte, D. Abou-Ras, K. Albe, G. H. Bauer, F. Bertram, C. Boit, R. Brüggemann, J. Christen, J. Dietrich, A. Eicke, D. Hariskos, M. Maiberg, R. Mainz, M. Meessen, M. Müller, O. Neumann, T. Orgis, S. Paetel, J. Pohl, H. Rodriguez-Alvarez, R. Scheer, H.-W. Schock, T. Unold, A. Weber, and M. Powalla, "Gallium gradients in $\text{Cu}(\text{In,Ga})\text{Se}_2$ thin-film solar cells," *Progress in Photovoltaics: Research and Applications*, vol. 23, no. 6, pp. 717–733, 2015. PIP-13-225.R2.
- [60] M. Turcu, I. M. Kötschau, and U. Rau, "Composition dependence of defect

- energies and band alignments in the $\text{Cu}(\text{In}_{1-x}\text{Ga}_x)(\text{Se}_{1-y}\text{S}_y)_2$ alloy system,” *Journal of Applied Physics*, vol. 91, no. 3, pp. 1391–1399, 2002.
- [61] O. Lundberg, M. Edoff, and L. Stolt, “The effect of Ga-grading in CIGS thin film solar cells,” *Thin Solid Films*, vol. 480, pp. 520 – 525, 2005. EMRS 2004.
- [62] T. Dullweber, O. Lundberg, J. Malmström, M. Bodegård, L. Stolt, U. Rau, H. Schock, and J. Werner, “Back surface band gap gradings in $\text{Cu}(\text{In,Ga})\text{Se}_2$ solar cells,” *Thin Solid Films*, vol. 387, no. 1, pp. 11 – 13, 2001. Proceedings of Symposium N on Thin Film Photovoltaic materials of the E-MRS Spring Conference.
- [63] J. Song, S. S. Li, C. Huang, O. Crisalle, and T. Anderson, “Device modeling and simulation of the performance of $\text{Cu}(\text{In}_{1-x}\text{Ga}_x)\text{Se}_2$ solar cells,” *Solid-State Electronics*, vol. 48, no. 1, pp. 73 – 79, 2004.
- [64] C. Frisk, C. Platzer-Björkman, J. Olsson, P. Szaniawski, J. T. Wätjen, V. Fjällström, P. Salomé, and M. Edoff, “Optimizing Ga-profiles for highly efficient $\text{Cu}(\text{In,Ga})\text{Se}_2$ thin film solar cells in simple and complex defect models,” *Journal of Physics D: Applied Physics*, vol. 47, no. 48, p. 485104, 2014.
- [65] M. Topič, F. Smole, and J. Furlan, “Band gap engineering in $\text{CdS}/\text{Cu}(\text{In,Ga})\text{Se}_2$ solar cells,” *Journal of Applied Physics*, vol. 79, no. 11, pp. 8537–8540, 1996.
- [66] M. Bär, W. Bohne, J. Röhrich, E. Strub, S. Lindner, M. C. Lux-Steiner, C.-H. Fischer, T. P. Niesen, and F. Karg, “Determination of the band gap depth profile of the pentenary $\text{Cu}(\text{In}_{(1-x)}\text{Ga}_x)(\text{S}_y\text{Se}_{(1-y)})_2$ chalcopyrite from its composition gradient,” *Journal of Applied Physics*, vol. 96, no. 7, pp. 3857–3860, 2004.
- [67] R. Scheer and H.-W. Schock, *Chalcogenide photovoltaics: physics, technologies, and thin film devices*. John Wiley & Sons, 2011.
- [68] T. Lavrenko, T. Ott, and T. Walter, “Impact of sulfur and gallium gradients on the performance of thin film $\text{Cu}(\text{In,Ga})(\text{Se,S})_2$ solar cells,” *Thin Solid Films*, vol. 582, pp. 51 – 55, 2015. E-MRS 2014 Spring Meeting, Symposium A, Thin-Film Chalcogenide Photovoltaic Materials.
- [69] Y. Goushi, H. Hakuma, K. Tabuchi, S. Kijima, and K. Kushiya, “Fabrication of pentenary $\text{Cu}(\text{InGa})(\text{SeS})_2$ absorbers by selenization and sulfurization,” *Solar Energy Materials and Solar Cells*, vol. 93, no. 8, pp. 1318 – 1320, 2009.
- [70] O. Lundberg, J. Lu, A. Rockett, M. Edoff, and L. Stolt, “Diffusion of indium and gallium in $\text{Cu}(\text{In,Ga})\text{Se}_2$ thin film solar cells,” *Journal of Physics and Chemistry of Solids*, vol. 64, no. 9, pp. 1499 – 1504, 2003. 13th International Conference on Ternary and Multinary Compounds.
- [71] C. Persson, “Electronic and optical properties of $\text{Cu}_2\text{ZnSnS}_4$ and $\text{Cu}_2\text{ZnSnSe}_4$,” *Journal of Applied Physics*, vol. 107, no. 5, p. 053710, 2010.
- [72] S. Siebentritt and S. Schorr, “Kesterites - a challenging material for solar cells,” *Progress in Photovoltaics: Research and Applications*, vol. 20, no. 5, pp. 512–519, 2012.
- [73] I. Olekseyuk, I. Dudchak, and L. Piskach, “Phase equilibria in the $\text{Cu}_2\text{S}-\text{ZnS}-\text{SnS}_2$ system,” *Journal of Alloys and Compounds*, vol. 368, no. 1, pp. 135 – 143, 2004.
- [74] A. Nagoya, R. Asahi, R. Wahl, and G. Kresse, “Defect formation and phase

- stability of $\text{Cu}_2\text{ZnSnS}_4$ photovoltaic material,” *Phys. Rev. B*, vol. 81, p. 113202, Mar 2010.
- [75] C. Platzer-Björkman, J. Scragg, H. Flammersberger, T. Kubart, and M. Edoff, “Influence of precursor sulfur content on film formation and compositional changes in $\text{Cu}_2\text{ZnSnS}_4$ films and solar cells,” *Solar Energy Materials and Solar Cells*, vol. 98, pp. 110 – 117, 2012.
- [76] Q. Guo, G. M. Ford, W.-C. Yang, B. C. Walker, E. A. Stach, H. W. Hillhouse, and R. Agrawal, “Fabrication of 7.2% efficient CZTSSe solar cells using CZTS nanocrystals,” *Journal of the American Chemical Society*, vol. 132, no. 49, pp. 17384–17386, 2010. PMID: 21090644.
- [77] S. Schorr, “The crystal structure of kesterite type compounds: A neutron and X-ray diffraction study,” *Solar Energy Materials and Solar Cells*, vol. 95, no. 6, pp. 1482 – 1488, 2011. Special Issue : Thin film and nanostructured solar cells.
- [78] J. J. S. Scragg, L. Choubac, A. Lafond, T. Ericson, and C. Platzer-Björkman, “A low-temperature order-disorder transition in $\text{Cu}_2\text{ZnSnS}_4$ thin films,” *Applied Physics Letters*, vol. 104, no. 4, p. 041911, 2014.
- [79] J. J. S. Scragg, J. K. Larsen, M. Kumar, C. Persson, J. Sandler, S. Siebentritt, and C. Platzer Björkman, “Cu–Zn disorder and band gap fluctuations in $\text{Cu}_2\text{ZnSn}(\text{S},\text{Se})_4$: Theoretical and experimental investigations,” *physica status solidi (b)*, vol. 253, no. 2, pp. 247–254, 2016.
- [80] S. Chen, A. Walsh, X.-G. Gong, and S.-H. Wei, “Classification of lattice defects in the kesterite $\text{Cu}_2\text{ZnSnS}_4$ and $\text{Cu}_2\text{ZnSnSe}_4$ earth-abundant solar cell absorbers,” *Advanced Materials*, vol. 25, no. 11, pp. 1522–1539, 2013.
- [81] S. Chen, A. Walsh, J.-H. Yang, X. G. Gong, L. Sun, P.-X. Yang, J.-H. Chu, and S.-H. Wei, “Compositional dependence of structural and electronic properties of $\text{Cu}_2\text{ZnSn}(\text{S},\text{Se})_4$ alloys for thin film solar cells,” *Phys. Rev. B*, vol. 83, p. 125201, Mar 2011.
- [82] S. Siebentritt, “Why are kesterite solar cells not 20% efficient?,” *Thin Solid Films*, vol. 535, pp. 1 – 4, 2013.
- [83] S. Bourdais, C. Choné, B. Delatouche, A. Jacob, G. Larramona, C. Moisan, A. Lafond, F. Donatini, G. Rey, S. Siebentritt, A. Walsh, and G. Dennler, “Is the Cu/Zn disorder the main culprit for the voltage deficit in kesterite solar cells?,” *Advanced Energy Materials*, vol. 6, no. 12, pp. 1502276–n/a, 2016. 1502276.
- [84] A. Weber, R. Mainz, and H. W. Schock, “On the Sn loss from thin films of the material system Cu–Zn–Sn–S in high vacuum,” *Journal of Applied Physics*, vol. 107, no. 1, p. 013516, 2010.
- [85] A. Redinger, D. M. Berg, P. J. Dale, and S. Siebentritt, “The consequences of kesterite equilibria for efficient solar cells,” *Journal of the American Chemical Society*, vol. 133, no. 10, pp. 3320–3323, 2011. PMID: 21329385.
- [86] J. J. Scragg, T. Ericson, T. Kubart, M. Edoff, and C. Platzer-Björkman, “Chemical insights into the instability of $\text{Cu}_2\text{ZnSnS}_4$ films during annealing,” *Chemistry of Materials*, vol. 23, no. 20, pp. 4625–4633, 2011.
- [87] B.-A. Schubert, B. Marsen, S. Cinque, T. Unold, R. Klenk, S. Schorr, and H.-W. Schock, “ $\text{Cu}_2\text{ZnSnS}_4$ thin film solar cells by fast coevaporation,” *Progress in Photovoltaics: Research and Applications*, vol. 19, no. 1,

- pp. 93–96, 2011.
- [88] T. Tanaka, D. Kawasaki, M. Nishio, Q. Guo, and H. Ogawa, “Fabrication of $\text{Cu}_2\text{ZnSnS}_4$ thin films by co-evaporation,” *physica status solidi (c)*, vol. 3, no. 8, pp. 2844–2847, 2006.
 - [89] S. Zhuk, A. Kushwaha, T. K. Wong, S. Masudy-Panah, A. Smirnov, and G. K. Dalapati, “Critical review on sputter-deposited $\text{Cu}_2\text{ZnSnS}_4$ (CZTS) based thin film photovoltaic technology focusing on device architecture and absorber quality on the solar cells performance,” *Solar Energy Materials and Solar Cells*, vol. 171, pp. 239 – 252, 2017.
 - [90] A. Moholkar, S. Shinde, G. Agawane, S. Jo, K. Rajpure, P. Patil, C. Bhosale, and J. Kim, “Studies of compositional dependent CZTS thin film solar cells by pulsed laser deposition technique: An attempt to improve the efficiency,” *Journal of Alloys and Compounds*, vol. 544, pp. 145 – 151, 2012.
 - [91] S. Pawar, A. Moholkar, I. Kim, S. Shin, J. Moon, J. Rhee, and J. Kim, “Effect of laser incident energy on the structural, morphological and optical properties of $\text{Cu}_2\text{ZnSnS}_4$ (CZTS) thin films,” *Current Applied Physics*, vol. 10, no. 2, pp. 565 – 569, 2010.
 - [92] J. J. Scragg, P. J. Dale, and L. M. Peter, “Towards sustainable materials for solar energy conversion: Preparation and photoelectrochemical characterization of $\text{Cu}_2\text{ZnSnS}_4$,” *Electrochemistry Communications*, vol. 10, no. 4, pp. 639 – 642, 2008.
 - [93] R. Schurr, A. Hölzing, S. Jost, R. Hock, T. Voß, J. Schulze, A. Kirbs, A. Ennaoui, M. Lux-Steiner, A. Weber, I. Kötschau, and H.-W. Schock, “The crystallisation of $\text{Cu}_2\text{ZnSnS}_4$ thin film solar cell absorbers from co-electroplated Cu–Zn–Sn precursors,” *Thin Solid Films*, vol. 517, no. 7, pp. 2465 – 2468, 2009. Thin Film Chalcogenide Photovoltaic Materials (EMRS, Symposium L).
 - [94] N. Kamoun, H. Bouzouita, and B. Rezig, “Fabrication and characterization of $\text{Cu}_2\text{ZnSnS}_4$ thin films deposited by spray pyrolysis technique,” *Thin Solid Films*, vol. 515, no. 15, pp. 5949 – 5952, 2007. Proceedings of Symposium O on Thin Film Chalcogenide Photovoltaic Materials, EMRS 2006 Conference.
 - [95] Y. K. Kumar, G. S. Babu, P. U. Bhaskar, and V. S. Raja, “Preparation and characterization of spray-deposited $\text{Cu}_2\text{ZnSnS}_4$ thin films,” *Solar Energy Materials and Solar Cells*, vol. 93, no. 8, pp. 1230 – 1237, 2009.
 - [96] T. K. Todorov, K. B. Reuter, and D. B. Mitzi, “High-efficiency solar cell with earth-abundant liquid-processed absorber,” *Advanced Materials*, vol. 22, no. 20, pp. E156–E159, 2010.
 - [97] J. J. Scragg, J. T. Wätjen, M. Edoff, T. Ericson, T. Kubart, and C. Platzer-Björkman, “A detrimental reaction at the molybdenum back contact in $\text{Cu}_2\text{ZnSn(S,Se)}_4$ thin-film solar cells,” *Journal of the American Chemical Society*, vol. 134, no. 47, pp. 19330–19333, 2012. PMID: 23146047.
 - [98] K. Seshan, *Handbook of thin film deposition*. William Andrew, 2012.
 - [99] W. Sproul, “High-rate reactive DC magnetron sputtering of oxide and nitride superlattice coatings,” *Vacuum*, vol. 51, no. 4, pp. 641 – 646, 1998.
 - [100] J. Musil, P. Baroch, J. Vlček, K. Nam, and J. Han, “Reactive magnetron sputtering of thin films: present status and trends,” *Thin Solid Films*, vol. 475, no. 1, pp. 208 – 218, 2005. Asian-European International Conference on

- Plasma Surface Engineering 2003 Proceedings of the 4th Asian-European International Conference on Plasma Surface Engineering.
- [101] B. Chapman, *Glow Discharge Processes: Sputtering and Plasma Etching*. Wiley, 1980.
 - [102] A. Anders, "Physics of arcing, and implications to sputter deposition," *Thin Solid Films*, vol. 502, no. 1, pp. 22 – 28, 2006. Selected Papers from the 5th International Conference on Coatings on Glass (ICCG5)- Advanced Coatings on Glass and Plastics for Large-Area or High-Volume Products.
 - [103] P. Kelly and R. Arnell, "Magnetron sputtering: a review of recent developments and applications," *Vacuum*, vol. 56, no. 3, pp. 159 – 172, 2000.
 - [104] G. Bräuer, B. Szyszka, M. Vergöhl, and R. Bandorf, "Magnetron sputtering – milestones of 30 years," *Vacuum*, vol. 84, no. 12, pp. 1354 – 1359, 2010. Selected Papers from the Proceedings of The Tenth International Symposium on Sputtering and Plasma Processes (ISSP 2009), 8th–10th July 2009, Kanazawa, Japan.
 - [105] O. Knotek, M. Böhmer, and T. Leyendecker, "On structure and properties of sputtered Ti and Al based hard compound films," *Journal of Vacuum Science & Technology A: Vacuum, Surfaces, and Films*, vol. 4, no. 6, pp. 2695–2700, 1986.
 - [106] J. B. Malherbe, "Sputtering of compound semiconductor surfaces. ii. compositional changes and radiation-induced topography and damage," *Critical Reviews in Solid State and Materials Sciences*, vol. 19, no. 3, pp. 129–195, 1994.
 - [107] D. M. Mattox, "Chapter 7 - physical sputtering and sputter deposition (sputtering)," in *Handbook of Physical Vapor Deposition (PVD) Processing (Second Edition)* (D. M. Mattox, ed.), pp. 237 – 286, Boston: William Andrew Publishing, second edition ed., 2010.
 - [108] F. Boydens, W. Leroy, R. Persoons, and D. Depla, "The influence of target surface morphology on the deposition flux during direct-current magnetron sputtering," *Thin Solid Films*, vol. 531, pp. 32 – 41, 2013.
 - [109] F. Boydens, W. Leroy, R. Persoons, and D. Depla, "The influence of target surface morphology on the deposition flux during direct-current magnetron sputtering," *Thin Solid Films*, vol. 531, pp. 32 – 41, 2013.
 - [110] K. Wasa, M. Kitabatake, and H. Adachi, "3 - sputtering phenomena," in *Thin Film Materials Technology* (K. Wasa, M. Kitabatake, and H. Adachi, eds.), pp. 71 – 114, Norwich, NY: William Andrew Publishing, 2004.
 - [111] H. A. Jehn, S. Hofmann, V. Rückborn, and W. Münz, "Morphology and properties of sputtered (Ti,Al)N layers on high speed steel substrates as a function of deposition temperature and sputtering atmosphere," *Journal of Vacuum Science & Technology A: Vacuum, Surfaces, and Films*, vol. 4, no. 6, pp. 2701–2705, 1986.
 - [112] T. Motohiro and Y. Taga, "Monte Carlo simulation of the particle transport process in sputter deposition," *Thin Solid Films*, vol. 112, no. 2, pp. 161 – 173, 1984.
 - [113] E. Särhammar, E. Strandberg, N. Martin, and T. Nyberg, "Sputter rate distribution and compositional variations in films sputtered from elemental and multi-element targets at different pressures," *International Journal of*

- Materials Science and Applications*, vol. 3, no. 2, pp. 29–36, 2014.
- [114] K. Macák, P. Macák, and U. Helmersson, “Monte Carlo simulations of the transport of sputtered particles,” *Computer Physics Communications*, vol. 120, no. 2, pp. 238 – 254, 1999.
 - [115] W. L. Patterson and G. A. Shirn, “The sputtering of nickel–chromium alloys,” *Journal of Vacuum Science and Technology*, vol. 4, no. 6, pp. 343–346, 1967.
 - [116] G. Betz and G. K. Wehner, *Sputtering of multicomponent materials*, pp. 11–90. Berlin, Heidelberg: Springer Berlin Heidelberg, 1983.
 - [117] P. Sigmund, A. Oliva, and G. Falcone, “Sputtering of multicomponent materials: Elements of a theory,” *Nuclear Instruments and Methods in Physics Research*, vol. 194, no. 1, pp. 541 – 548, 1982.
 - [118] J. A. Frantz, J. D. Myers, R. Y. Bekele, V. Q. Nguyen, B. M. Sadowski, S. I. Maximenko, M. P. Lumb, R. J. Walters, and J. S. Sanghera, “Quaternary sputtered Cu(In,Ga)Se₂ absorbers for photovoltaics: A review,” *IEEE Journal of Photovoltaics*, vol. 6, pp. 1036–1050, July 2016.
 - [119] S. M. Kong, R. Fan, S. H. Jung, and C. W. Chung, “Characterization of Cu(In,Ga)Se₂ thin films prepared by rf magnetron sputtering using a single target without selenization,” *Journal of Industrial and Engineering Chemistry*, vol. 19, no. 4, pp. 1320 – 1324, 2013.
 - [120] T.-Y. Lin, C.-H. Chen, W.-C. Huang, W.-H. Ho, Y.-H. Wu, and C.-H. Lai, “Direct probing Se spatial distribution in Cu(In_xGa_{1-x})Se₂ solar cells: A key factor to achieve high efficiency performance,” *Nano Energy*, vol. 19, pp. 269 – 278, 2016.
 - [121] Q. Cao, O. Gunawan, M. Copel, K. B. Reuter, S. J. Chey, V. R. Deline, and D. B. Mitzi, “Defects in Cu(In,Ga)Se₂ chalcopyrite semiconductors: A comparative study of material properties, defect states, and photovoltaic performance,” *Advanced Energy Materials*, vol. 1, no. 5, pp. 845–853, 2011.
 - [122] C.-H. Chen, W.-C. Shih, C.-Y. Chien, C.-H. Hsu, Y.-H. Wu, and C.-H. Lai, “A promising sputtering route for one-step fabrication of chalcopyrite phase Cu(In,Ga)Se₂ absorbers without extra se supply,” *Solar Energy Materials and Solar Cells*, vol. 103, pp. 25 – 29, 2012.
 - [123] C.-H. Chen, T.-Y. Lin, C.-H. Hsu, S.-Y. Wei, and C.-H. Lai, “Comprehensive characterization of Cu-rich Cu(In,Ga)Se₂ absorbers prepared by one-step sputtering process,” *Thin Solid Films*, vol. 535, pp. 122 – 126, 2013.
 - [124] J. A. Frantz, R. Y. Bekele, J. D. Myers, V. Q. Nguyen, J. S. Sanghera, S. I. Maximenko, M. Gonzalez, J. G. Tischler, R. J. Walters, M. S. Leite, A. Bruce, S. V. Frolov, and M. Cyrus, “Structural and electronic characteristics of Cu(In,Ga)Se₂ thin films sputtered from quaternary targets,” in *2012 38th IEEE Photovoltaic Specialists Conference*, pp. 003098–003101, June 2012.
 - [125] C.-H. Hsu, Y.-S. Su, S.-Y. Wei, C.-H. Chen, W.-H. Ho, C. Chang, Y.-H. Wu, C.-J. Lin, and C.-H. Lai, “Na-induced efficiency boost for Se-deficient Cu(In,Ga)Se₂ solar cells,” *Progress in Photovoltaics: Research and Applications*, vol. 23, no. 11, pp. 1621–1629, 2015. PIP-14-286.R1.
 - [126] C.-H. Hsu, W.-H. Ho, S.-Y. Wei, and C.-H. Lai, “Over 14% efficiency of directly sputtered Cu(In,Ga)Se₂ absorbers without postselenization by post-treatment of alkali metals,” *Advanced Energy Materials*, vol. 7, no. 13, pp. 1602571–n/a, 2017. 1602571.

- [127] L. Ouyang, D. Zhuang, M. Zhao, N. Zhang, X. Li, L. Guo, R. Sun, and M. Cao, "Cu(In,Ga)Se₂ solar cell with 16.7% active-area efficiency achieved by sputtering from a quaternary target," *physica status solidi (a)*, vol. 212, no. 8, pp. 1774–1778, 2015.
- [128] C. Yan, J. Chen, F. Liu, N. Song, H. Cui, B. K. Ng, J. A. Stride, and X. Hao, "Kesterite Cu₂ZnSnS₄ solar cell from sputtered Zn/(Cu & Sn) metal stack precursors," *Journal of Alloys and Compounds*, vol. 610, pp. 486 – 491, 2014.
- [129] B.-T. Jheng, P.-T. Liu, and M.-C. Wu, "A promising sputtering route for dense Cu₂ZnSnS₄ absorber films and their photovoltaic performance," *Solar Energy Materials and Solar Cells*, vol. 128, pp. 275 – 282, 2014.
- [130] J.-S. Seol, S.-Y. Lee, J.-C. Lee, H.-D. Nam, and K.-H. Kim, "Electrical and optical properties of Cu₂ZnSnS₄ thin films prepared by rf magnetron sputtering process," *Solar Energy Materials and Solar Cells*, vol. 75, no. 1, pp. 155 – 162, 2003. PVSEC 12 Part II.
- [131] M. Xie, D. Zhuang, M. Zhao, B. Li, M. Cao, and J. Song, "Fabrication of Cu₂ZnSnS₄ thin films using a ceramic quaternary target," *Vacuum*, vol. 101, pp. 146 – 150, 2014. Including rapid communications, original articles and a special section: Measurement Characteristics and Use of Quadrupole Mass Spectrometers for Vacuum Applications.
- [132] J. He, L. Sun, K. Zhang, W. Wang, J. Jiang, Y. Chen, P. Yang, and J. Chu, "Effect of post-sulfurization on the composition, structure and optical properties of Cu₂ZnSnS₄ thin films deposited by sputtering from a single quaternary target," *Applied Surface Science*, vol. 264, pp. 133 – 138, 2013.
- [133] A. Inamdar, S. Lee, K.-Y. Jeon, C. H. Lee, S. Pawar, R. Kalubarme, C. J. Park, H. Im, W. Jung, and H. Kim, "Optimized fabrication of sputter deposited Cu₂ZnSnS₄ (CZTS) thin films," *Solar Energy*, vol. 91, pp. 196 – 203, 2013.
- [134] J. He, L. Sun, Y. Chen, J. Jiang, P. Yang, and J. Chu, "Cu₂ZnSnS₄ thin film solar cell utilizing rapid thermal process of precursors sputtered from a quaternary target: a promising application in industrial processes," *RSC Adv.*, vol. 4, pp. 43080–43086, 2014.
- [135] R. Nakamura, K. Tanaka, H. Uchiki, K. Jimbo, T. Washio, and H. Katagiri, "Cu₂ZnSnS₄ thin film deposited by sputtering with Cu₂ZnSnS₄ compound target," *Japanese Journal of Applied Physics*, vol. 53, no. 2S, p. 02BC10, 2014.
- [136] J. Feng, X. Huang, W. Chen, J. Wu, H. Lin, Q. Cheng, D. Yun, and F. Zhang, "Fabrication and characterization of Cu₂ZnSnS₄ thin films for photovoltaic application by low-cost single target sputtering process," *Vacuum*, vol. 126, pp. 84 – 90, 2016.
- [137] Y.-P. Lin, Y.-F. Chi, T.-E. Hsieh, Y.-C. Chen, and K.-P. Huang, "Preparation of Cu₂ZnSnS₄ (CZTS) sputtering target and its application to the fabrication of CZTS thin-film solar cells," *Journal of Alloys and Compounds*, vol. 654, pp. 498 – 508, 2016.
- [138] H. D. Hagstrum, "Low energy de-excitation and neutralization processes near surfaces," in *Inelastic Ion–Surface Collisions* (N.H.TOLK, J. TULLY, W. HEILAND, and C. W. WHITE, eds.), pp. 1 – 25, Academic Press, 1977.
- [139] J. A. Thornton and D. W. Hoffman, "The influence of discharge current on the intrinsic stress in Mo films deposited using cylindrical and planar magnetron sputtering sources," *Journal of Vacuum Science & Technology A: Vacuum*,

- Surfaces, and Films*, vol. 3, no. 3, pp. 576–579, 1985.
- [140] W. Wang, J. Roth, S. Lindig, and C. Wu, “Blister formation of tungsten due to ion bombardment,” *Journal of Nuclear Materials*, vol. 299, no. 2, pp. 124 – 131, 2001.
 - [141] M. Fukumoto, Y. Ohtsuka, Y. Ueda, M. Taniguchi, M. Kashiwagi, T. Inoue, and K. Sakamoto, “Blister formation on tungsten damaged by high energy particle irradiation,” *Journal of Nuclear Materials*, vol. 375, no. 2, pp. 224 – 228, 2008.
 - [142] B. Singh and H. Trinkaus, “An analysis of the bubble formation behaviour under different experimental conditions,” *Journal of Nuclear Materials*, vol. 186, no. 2, pp. 153 – 165, 1992.
 - [143] R. A. Levy and P. K. Gallagher, “Argon entrapment and evolution in sputtered TaSi₂ films,” *Journal of The Electrochemical Society*, vol. 132, no. 8, pp. 1986–1995, 1985.
 - [144] L. Maissel and R. Glang, *Handbook of thin film technology*. McGraw-Hill handbooks, McGraw-Hill, 1970.
 - [145] F. Pianezzi, A. Chirilă, P. Blösch, S. Seyrling, S. Buecheler, L. Kranz, C. Fella, and A. N. Tiwari, “Electronic properties of Cu(In,Ga)Se₂ solar cells on stainless steel foils without diffusion barrier,” *Progress in Photovoltaics: Research and Applications*, vol. 20, no. 3, pp. 253–259, 2012.
 - [146] F. Pianezzi, S. Nishiwaki, L. Kranz, C. M. Sutter-Fella, P. Reinhard, B. Bissig, H. Hagendorfer, S. Buecheler, and A. N. Tiwari, “Influence of ni and cr impurities on the electronic properties of Cu(In,Ga)Se₂ thin film solar cells,” *Progress in Photovoltaics: Research and Applications*, vol. 23, no. 7, pp. 892–900, 2015. PIP-13-179.R2.
 - [147] T. Nakada, D. Iga, H. Ohbo, and A. Kunioka, “Effects of sodium on Cu(In,Ga)Se₂ -based thin films and solar cells,” *Japanese Journal of Applied Physics*, vol. 36, no. 2R, p. 732, 1997.
 - [148] A. Chirila, P. Reinhard, F. Pianezzi, P. Bloesch, A. R. Uhl, C. Fella, L. Kranz, D. Keller, C. Gretener, H. Hagendorfer, *et al.*, “Potassium-induced surface modification of Cu(In,Ga)Se₂ thin films for high-efficiency solar cells,” *Nature materials*, vol. 12, no. 12, p. 1107, 2013.
 - [149] P. Salomé, H. Rodriguez-Alvarez, and S. Sadewasser, “Incorporation of alkali metals in chalcogenide solar cells,” *Solar Energy Materials and Solar Cells*, vol. 143, pp. 9 – 20, 2015.
 - [150] Z.-K. Yuan, S. Chen, Y. Xie, J.-S. Park, H. Xiang, X.-G. Gong, and S.-H. Wei, “Na-diffusion enhanced p-type conductivity in Cu(In,Ga)Se₂: A new mechanism for efficient doping in semiconductors,” *Advanced Energy Materials*, vol. 6, no. 24, pp. 1601191–n/a, 2016. 1601191.
 - [151] T. Ericson, T. Kubart, J. J. Scragg, and C. Platzer-Björkman, “Reactive sputtering of precursors for Cu₂ZnSnS₄ thin film solar cells,” *Thin Solid Films*, vol. 520, no. 24, pp. 7093 – 7099, 2012.
 - [152] A. Tempez, S. Legendre, J.-P. Barnes, and E. Nolot, “Combining plasma profiling tofms with tof-sims depth profiling for microelectronic applications,” *Journal of Vacuum Science & Technology B, Nanotechnology and Microelectronics: Materials, Processing, Measurement, and Phenomena*, vol. 34, no. 3, p. 03H120, 2016.

- [153] S. Mondal and C. S. Solanki, "Deep diffusion of phosphorus in silicon using microsecond-pulsed laser doping," *Materials Science in Semiconductor Processing*, vol. 59, pp. 10 – 17, 2017.
- [154] J. Chandrappan, M. Murray, P. Petrik, E. Agocs, Z. Zolnai, A. Tempez, S. Legendre, D. Steenson, A. Jha, and G. Jose, "Doping silica beyond limits with laser plasma for active photonic materials," *Optical Materials Express*, vol. 5, November 2015. (c) 2015, Optical Society of America. This is an author produced version of a paper published in Optical Materials Express. Uploaded in accordance with the publisher's self-archiving policy.
- [155] L. V. Puyvelde, J. Lauwaert, A. Tempez, W. Devulder, S. Nishiwaki, F. Pianezzi, C. Detavernier, A. N. Tiwari, and H. Vrielinck, "Electronic defect study on low temperature processed cu(in,ga)se 2 thin-film solar cells and the influence of an sb layer," *Journal of Physics D: Applied Physics*, vol. 48, no. 17, p. 175104, 2015.
- [156] S. S. Hegedus and W. N. Shafarman, "Thin-film solar cells: device measurements and analysis," *Progress in Photovoltaics: Research and Applications*, vol. 12, no. 2-3, pp. 155–176, 2004.
- [157] M. Burgelman, K. Decock, S. Khelifi, and A. Abass, "Advanced electrical simulation of thin film solar cells," *Thin Solid Films*, vol. 535, pp. 296 – 301, 2013.
- [158] M. Burgelman, P. Nollet, and S. Degrave, "Modelling polycrystalline semiconductor solar cells," *Thin Solid Films*, vol. 361, pp. 527 – 532, 2000.
- [159] M. Burgelman and J. Marlein, "Analysis of graded band gap solar cells with scaps," in *Proceedings of the 23rd European Photovoltaic Solar Energy Conference*, pp. 2151–2155, WIP, 2008.
- [160] "SPICE home page." <https://bwrccs.eecs.berkeley.edu/Courses/IcBook/SPICE/>. Accessed: 2017-08-21.
- [161] T. Prabhakar and N. Jampana, "Effect of sodium diffusion on the structural and electrical properties of Cu₂ZnSnS₄ thin films," *Solar Energy Materials and Solar Cells*, vol. 95, no. 3, pp. 1001 – 1004, 2011.
- [162] J. A. Thornton, "The microstructure of sputter-deposited coatings," *Journal of Vacuum Science & Technology A: Vacuum, Surfaces, and Films*, vol. 4, no. 6, pp. 3059–3065, 1986.
- [163] D. Hoffman, "Stress and property control in sputtered metal films without substrate bias," *Thin Solid Films*, vol. 107, no. 4, pp. 353 – 358, 1983.
- [164] W. W. Lee and D. Oblas, "Argon concentration in tungsten films deposited by DC sputtering," *Journal of Vacuum Science and Technology*, vol. 7, no. 1, pp. 129–133, 1970.
- [165] J. J. Cuomo and R. J. Gambino, "Incorporation of rare gases in sputtered amorphous metal films," *Journal of Vacuum Science and Technology*, vol. 14, no. 1, pp. 152–157, 1977.
- [166] C. Malerba, M. Valentini, C. A. Ricardo, A. Rinaldi, E. Cappelletto, P. Scardi, and A. Mittiga, "Blistering in Cu₂ZnSnS₄ thin films: correlation with residual stresses," *Materials & Design*, vol. 108, pp. 725 – 735, 2016.
- [167] S. Schleussner, U. Zimmermann, T. Wätjen, K. Leifer, and M. Edoff, "Effect of gallium grading in Cu(In,Ga)Se₂ solar-cell absorbers produced by

- multi-stage coevaporation,” *Solar Energy Materials and Solar Cells*, vol. 95, no. 2, pp. 721 – 726, 2011.
- [168] M. Gloeckler and J. Sites, “Band-gap grading in Cu(In,Ga)Se₂ solar cells,” *Journal of Physics and Chemistry of Solids*, vol. 66, no. 11, pp. 1891 – 1894, 2005. The 14th International Conference on Ternary and Multinary Compounds.
- [169] I. Repins, L. Mansfield, A. Kanevce, S. A. Jensen, D. Kuciauskas, S. Glynn, T. Barnes, W. Metzger, J. Burst, C. S. Jiang, P. Dippo, S. Harvey, G. Teeter, C. Perkins, B. Egaas, A. Zakutayev, J. H. Alsmeier, T. Lußky, L. Korte, R. G. Wilks, M. Bär, Y. Yan, S. Lany, P. Zawadzki, J. S. Park, and S. Wei, “Wild band edges: The role of bandgap grading and band-edge fluctuations in high-efficiency chalcogenide devices,” in *2016 IEEE 43rd Photovoltaic Specialists Conference (PVSC)*, pp. 0309–0314, June 2016.

Acta Universitatis Upsaliensis

*Digital Comprehensive Summaries of Uppsala Dissertations
from the Faculty of Science and Technology 1564*

Editor: The Dean of the Faculty of Science and Technology

A doctoral dissertation from the Faculty of Science and Technology, Uppsala University, is usually a summary of a number of papers. A few copies of the complete dissertation are kept at major Swedish research libraries, while the summary alone is distributed internationally through the series Digital Comprehensive Summaries of Uppsala Dissertations from the Faculty of Science and Technology. (Prior to January, 2005, the series was published under the title "Comprehensive Summaries of Uppsala Dissertations from the Faculty of Science and Technology".)



ACTA
UNIVERSITATIS
UPSALIENSIS
UPPSALA
2017

Distribution: publications.uu.se
urn:nbn:se:uu:diva-329778